



Summer Research Scholars 2023



Message to our students: August 11, 2023

This year we are proud to have been able to resume the Garcia Scholar Program throughout the entire summer. Our goal was to explore different research venues and share our knowledge. Through collaboration and inclusion the sum becomes greater than the parts. At Stony Brook University we are fortunate to have Prof. Brooke Ellison to guide us in thoughtful consideration of the ethical implications of our research programs. Together with the Garcia students, she has led them in the initiation of the peer reviewed Journal of Ethics in Scientific and Technological Innovation, edited by the students (<https://you.stonybrook.edu/jesti>). In recognition of her tireless efforts to instill humanism and responsibility in our research efforts, we have chosen to honor Prof. Ellison as our key note speaker for the symposium this summer.

The Garcia Center for Polymers at Engineered Interfaces was founded in 1996 and is named after the late Queens College professor, Narciso Garcia, who was a pioneer in the integration of education and research. The Center focuses on the broad application of materials research to engineering, medicine, and energy, and recently, AI, machine learning, and computational modeling. The Center also supports innovation through entrepreneurship and has multiple collaborations with industry and national laboratories. In the research program, high school students work together with undergraduates, PhD, post PhD and faculty who collaborate in addressing challenges at the cutting edge of modern science. The students are encouraged to publish in refereed scientific journals, present their results at national conferences, and develop patents to protect their intellectual property. Our goal is to convey to the students the excitement we enjoy daily in research and provide for them a supportive network within the scientific community. Research is a lifelong experience and we hope to remain as a resource to our students long after "graduation".

This sentiment is best expressed by the logo designed by Hannah Oh '23 who wrote;

"This year, the Garcia logo has been designed to capture the essence of connection that lies at the heart of Garcia. Just as many monomers join to form a polymer, at Garcia, individuals of diverse backgrounds, experiences, and disciplines join efforts to work towards the exciting goal that is scientific innovation. The meaningful skills, knowledge, and relationships we gained over the summer will forever be cherished. Thank you Garcia 2023 for such an unforgettable experience!"

Sincerely,

Miriam Rafailovich and

Jonathan Sokolov

High School Students



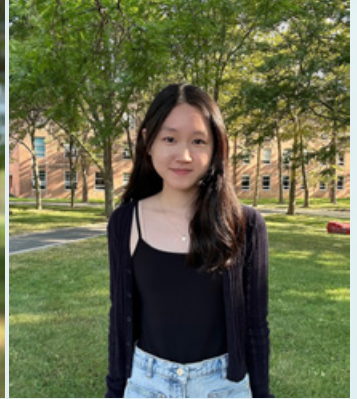
Hyeonji (Tiffany) Ahn



Haaris Alam



Isana Alicea



Kriste An



Saranya Anantapantula



Lamia Ayaz



Dvita Bhattacharya



Sophia Bracco



Harjaisal Brar



Brandon Cai



Boheng Cao



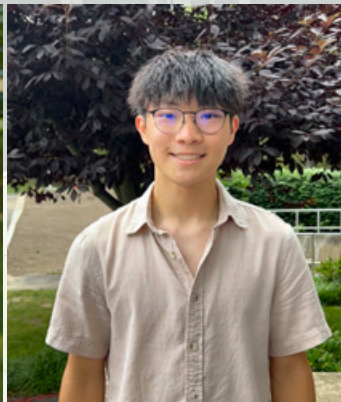
Kenneth Chang



Matthew Chang



Richard Chen

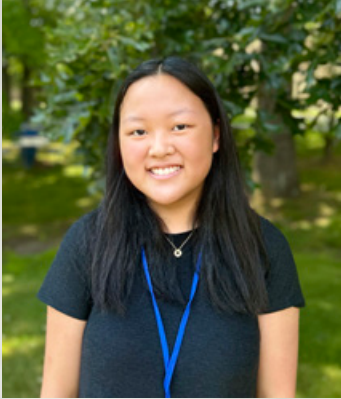


Samuel Chen



Ella Chu

High School Students



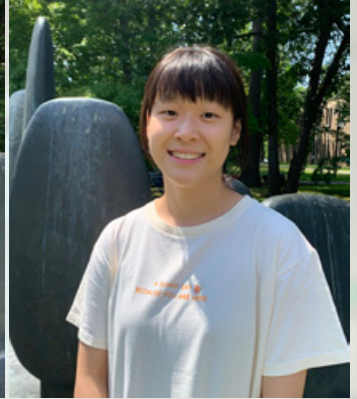
Catherine Chun



Sammy Coopersmith



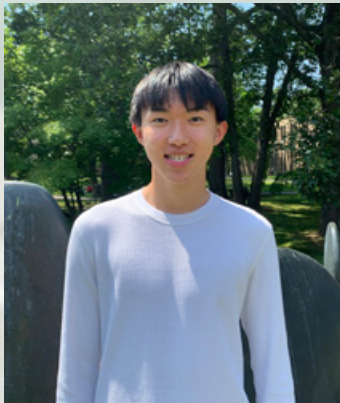
Sahana Dhama



Brinley Dai



Peter Elmer



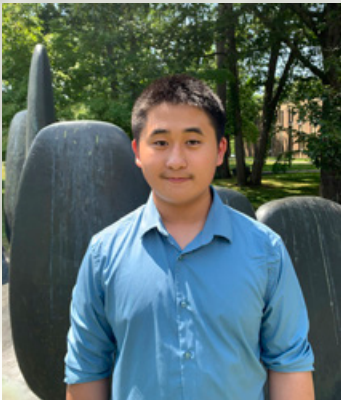
Dylan Fei



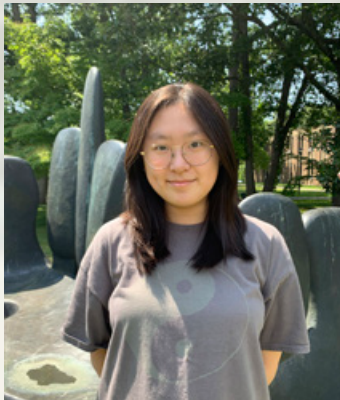
Hannah Feng



Anita Gaenko



Jerry Gao



Jacqueline Han



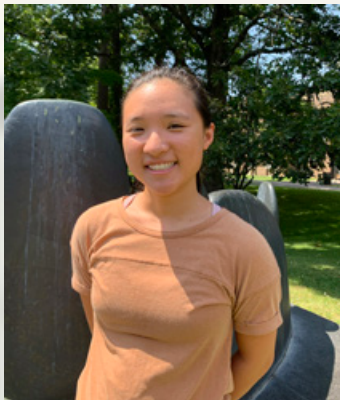
Elaina Heghes



Anna Heimowitz



Sharis Hsu



Ellen Hu



Ashley Huang



Henry Huang

High School Students



Parth Jain



Prisha Jain



Cecilia Jin



Annika Joshi



Ashritha Kalakuntla



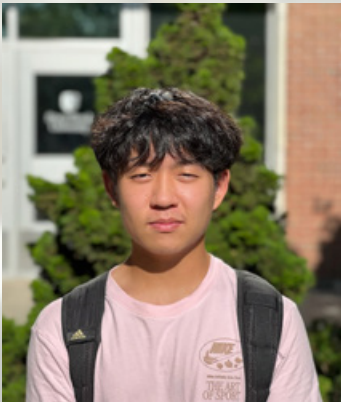
Claire Kang



Gyulim (Jessica) Kang



Juni Kim



Ryan Kim



Tei Kim



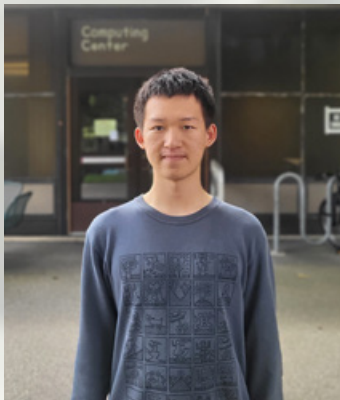
Aditi Kiran



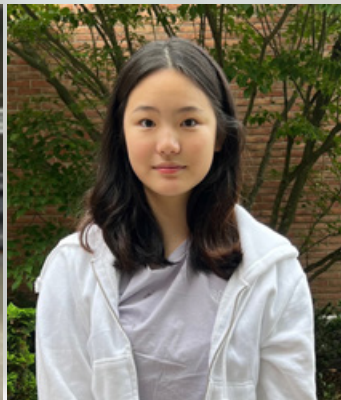
Pranav Kota



Ethan Lai



Daniel Lai



Ann Lee



Caitlyn Limbert

High School Students



Sheldon Liu



Michael Lotwin



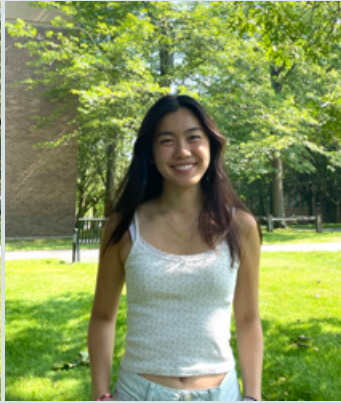
Daniel Lu



Sripradha Manikantan



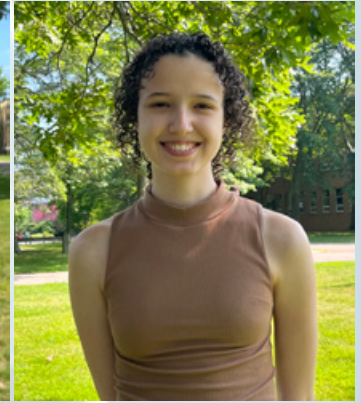
Anusha Misra



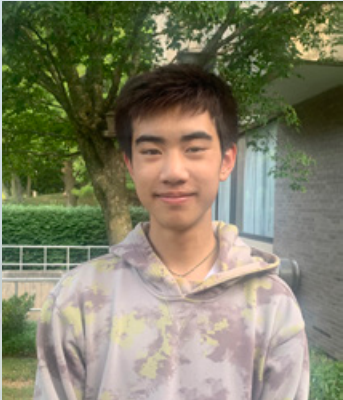
Elise Ngo



Hannah Oh



Jude Ouerfelli



Evan Pang



Jiarui Peng



Grace Qiao



Arianna Roland



Sergio Rosa



Dominic Rossiello



Jonathan Sacolick



Akhil Samavedam

High School Students



Andrew Shin



Pia Sodhi



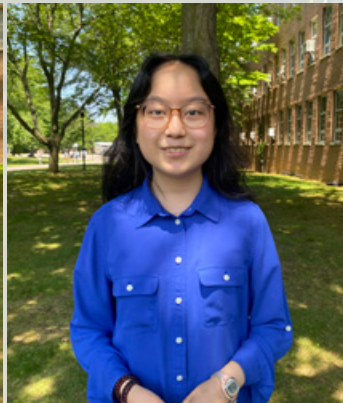
Sam Specht



Anirudh Srinivasan



Leora Stochel



Emily Sun



Matthew Sun



Rohan Suri



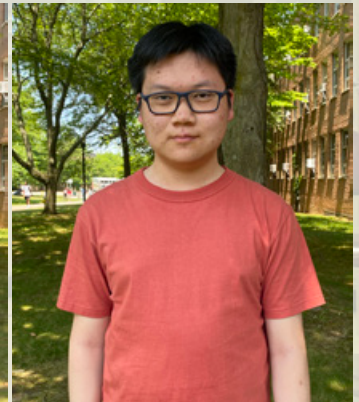
Avi Talsania



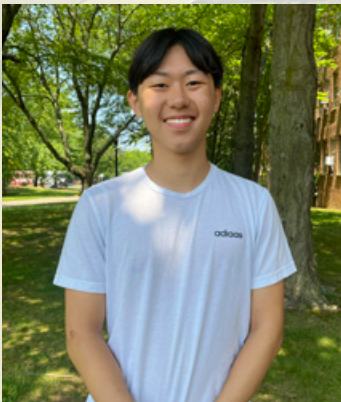
Aman Thawani



Melvin Thu



Tony Tung



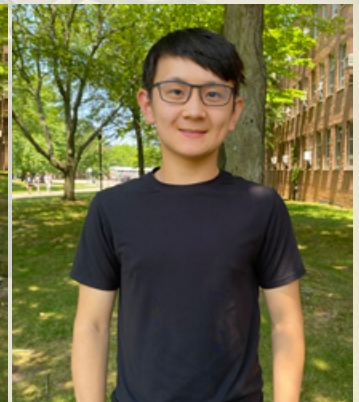
Alex Wang



Grace Wang



Oliver Wang



Michael Wang

High School Students



Raymond Wang



Erin Wong



Richard Wong



Shirley Xiong



Wilson Xu



Eleanor Yang



Aman Yarlagadda



Daniel Yoon



Adam Zaidi



Derek Zhang



Elaine Zhang



Michael Zhang



Richard Zhang



Selina Zhang

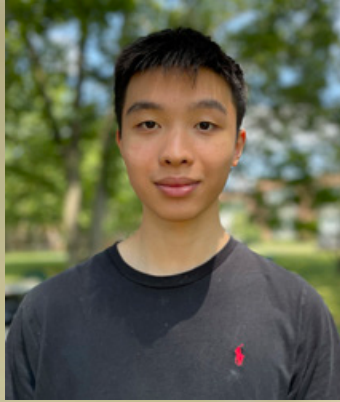


Alex Zheng



Mike Zhou

High School Students



Anthony Zhu



Research Experience for Undergraduates (REU)



Christian Apostol



Bernard Essuman



Maddie Freilich



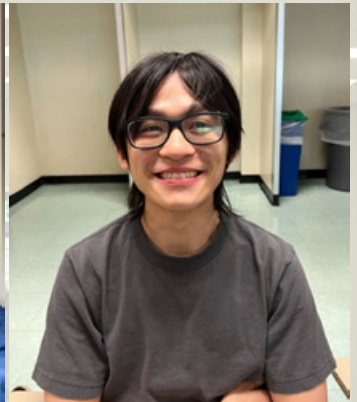
Jason Goldstein



Junior Gonzalez



Megha Gopal



Eugene Jiang



Sahaana Kesavan



Rachel Na



Ruth Pereira



Brooklyn Ratel



Alex Samadi



Briman Yang



Jacob Zerykier

Graduate Students



Haoyan Fang



Yiwei Fang



Shi Fu



Rosario Grasso



Adam Hansen



Karin Hasegawa



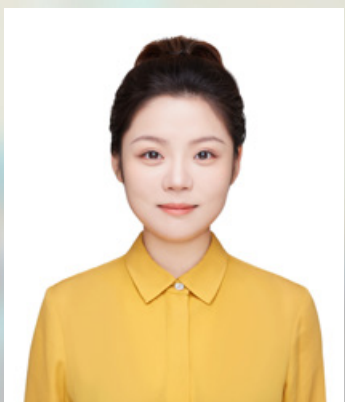
Jessica Hofflich



Yu-Chung Lin



Huiting Luo



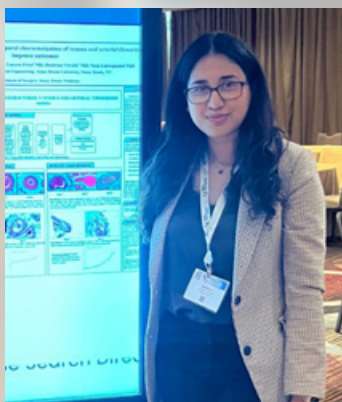
Ziyuan Niu



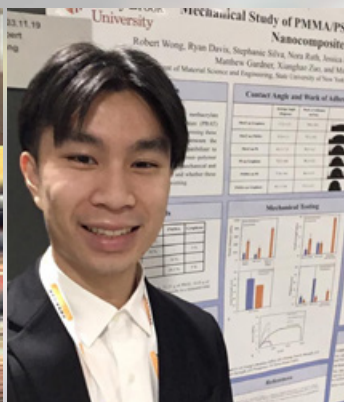
Md Farabi Rahman



Milana Stein



Shiffoni Sukhlal



Robert Wong



Yifan Yin

Faculty & Staff



Jonathan Sokolov



Miriam Rafailovich



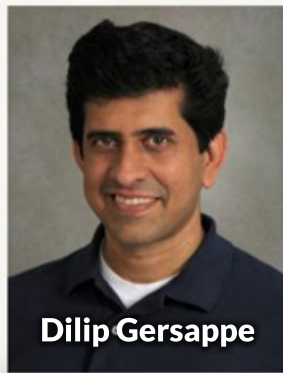
Michael Cui



Marcia Simon



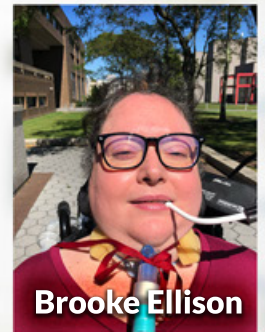
David Sprouster



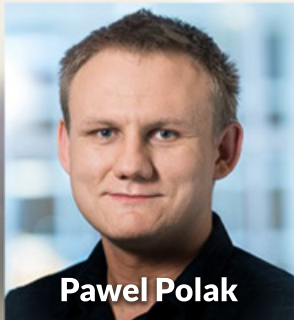
Dilip Gersappe



Rebecca Isseroff



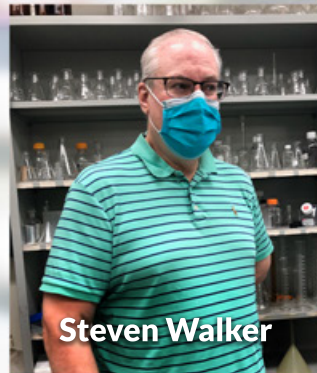
Brooke Ellison



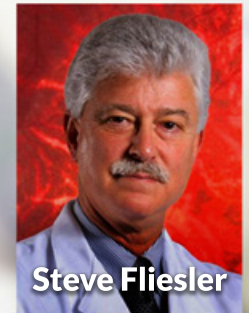
Pawel Polak



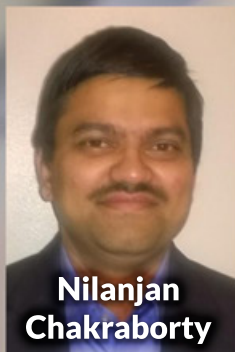
Chander Sadasivan



Steven Walker



Steve Fliesler



Nilanjan Chakraborty



Herb Weiss



John Jerome



Gurtej Singh



Kuan-Che Feng



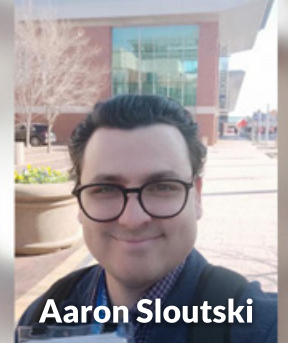
Rachel Brownlee



Yuefan Deng



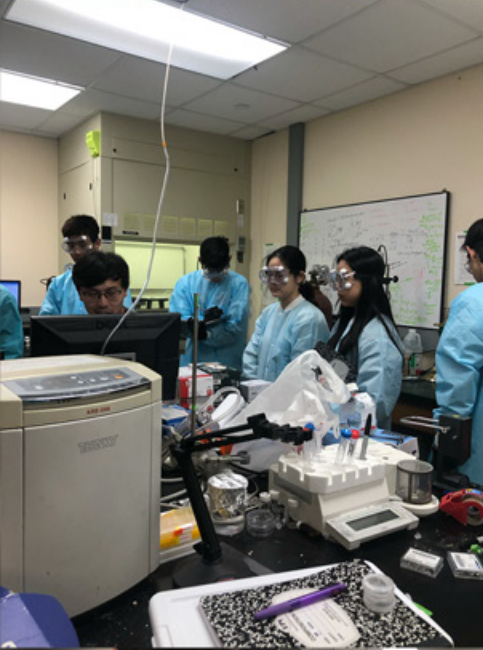
Sriganesh Ramachandra Rao



Aaron Sloutski

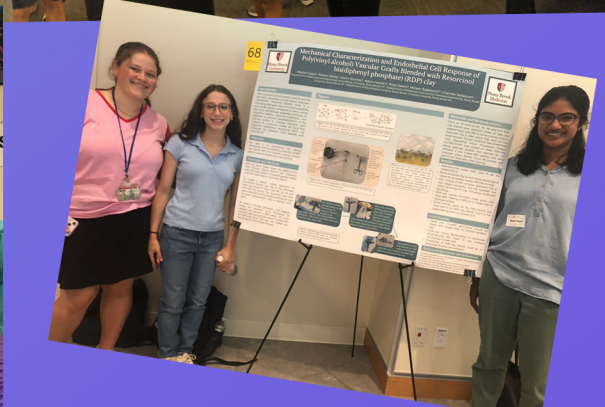
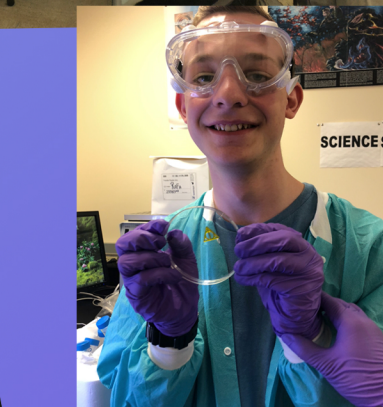
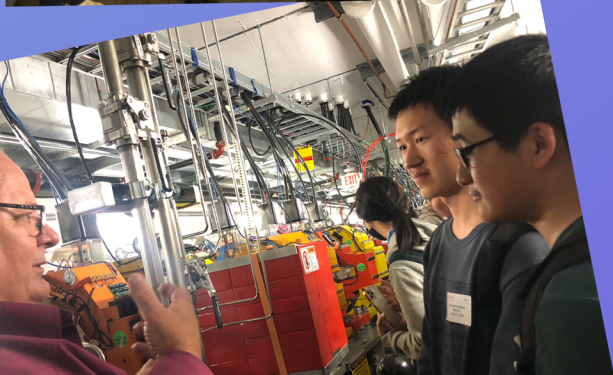
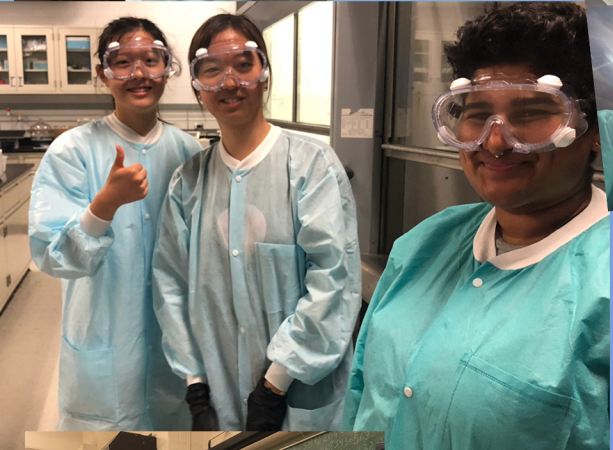
Research Bootcamp!



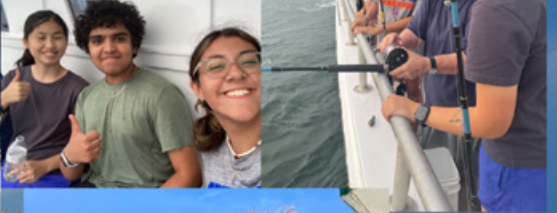


In the lab





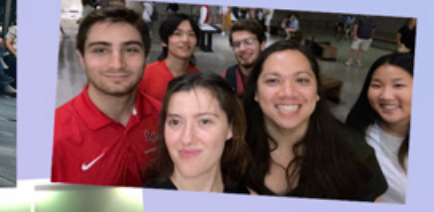
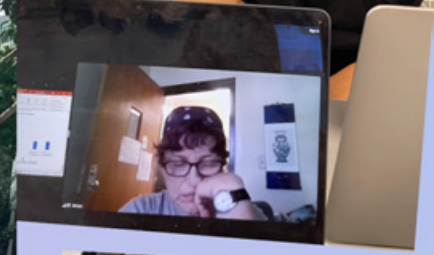
Fishing!

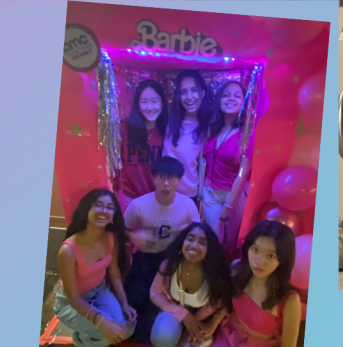
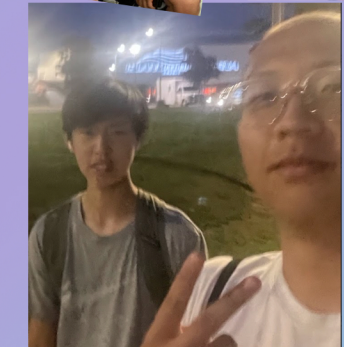
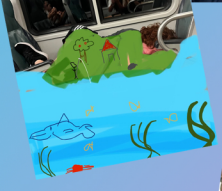
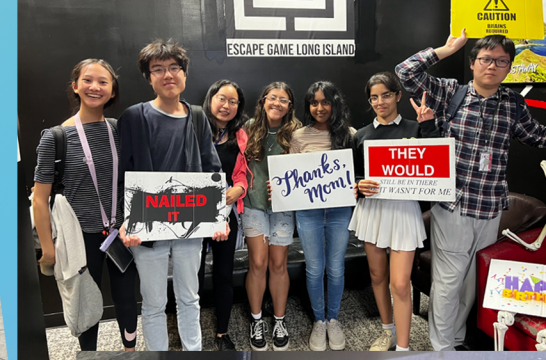


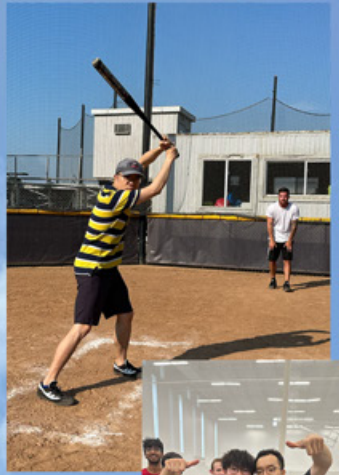
Canoeing!



Fun!







VS!





Summer Scholar Schedule of Weekly Activities

Each day starts with a mandatory group meeting at 10:15 AM!

Daily Schedule: Week of 6/26

Monday – 6/26	Tuesday – 6/27	Wednesday – 6/28	Thursday – 6/29	Friday – 6/30
<p>10:15 – 10:30: Introduction</p> <p>10:30 – 11:00: Dr. Carl Lejuez, Provost: Greeting</p> <p>11:00 – 11:45: Dr. Anne-Marie Scheidt: Welcome</p> <p>11:45 – 12:30: Prof. Steven J. Fliesler: Structure of the Retina</p> <p>12:30 – 1:20: Lunch</p> <p>1:20 – 2:20: Madeline Augustine: Working at Boeing</p> <p>2:20 – 3:15: Prof. Dilip Gersappe: Modeling the Materials World</p> <p>3:15 – 4:15: Prof. Yi-Xian Qin: Neuronal Differentiation</p>	<p>10:15 – 10:30: Organizational Meeting</p> <p>10:30 – 11:45: Mandatory EH&S Chemical Training</p> <p>11:45 – 12:00: Robert Wong: Therapeutic Polymers</p> <p>12:00 – 12:45: Lunch</p> <p>12:45 – 1:40: Fire Safety Training</p> <p>1:40 – 2:30: Dr. Mike Cuiffo: FTIR & XRF</p> <p>2:30 – 3:40: Dr. Pawel Polak: AI and Microemotions</p> <p>3:40 – 4:15: Dr. Chang-Yong Nam: Atomic Layer Deposition</p>	<p>10:15 – 10:30: Organizational Meeting</p> <p>10:15 – 12:30: Mandatory EH&S Biosafety & Hazardous Waste Training</p> <p>11:40 – 11:45: Annual Group Picture</p> <p>11:30 – 12:30: Lunch</p> <p>2:20 – 3:10: Dr. Gurtej Singh: Bioprinted Human Skin Models with Embedded Vascular Networks</p> <p>2:15 – 3:15: Dr. Chrystian Junqueira- Alves: Biomechanics</p> <p>3:15 – 4:15: Rebecca Isseroff: Graphene & HS Student Research</p>	<p>10:15 – 10:30: Organizational Meeting</p> <p>10:30 – 11:15: Dr. Tai-De Li: XPS, TOF-SIMS, & AFM</p> <p>11:15 – 12:00: Dr. Yuefan Deng: In Silico Biology</p> <p>12:00 – 12:45: Lunch</p> <p>12:45 – 4:15: Facilities Tour</p>	<p>10:15 – 10:45: Organizational Meeting & Facilities/Safety Quiz</p> <p>10:45 – 11:45: Prof. Nilanjan Chakraborty: Robotics</p> <p>11:45 – 1:00: Dr. Jonathan Sokolov: Working with DNA</p> <p>12:30: Pizza Working Lunch</p> <p>1:00 – 1:30: Herb Weiss: ISEF and Science Competitions</p> <p>1:30 – 2:00: Dr. Mina Mahidan: AI in Dentistry</p>

Summer Scholar Schedule of Weekly Activities

Each day starts with a mandatory group meeting at 10:15 AM!

Daily Schedule: Week of 7/3


Sunday – 7/2:	Monday – 7/3	Tuesday – 7/4	Wednesday – 7/5	Thursday – 7/6	Friday – 7/7
<p>Trip to Nassau Symphony Pops Orchestra in Concert at Hecksher State Park Featuring Prof. John Jerome</p> <p>Plus Garcia Dinner (5:30 – 9:30 PM)</p>	<p>10:15 – 10:30: Organizational Meeting</p> <p>10:30 – 11:30: Clara Tran: Library Search Training</p> <p>11:30 – 12:20: Aaron Sloutski: Biomedical Polymers</p> <p>12:20 – 1:00: Lunch</p> <p>1:00 – 1:50: Prof. Eyal Zussman: Endoscopic Brush Cytology</p> <p>2:40 – 3:10: Shiffoni Sukhlal: Thombogenics</p> <p>3:10 – 4:15: Prof. Marcia Simon: Engineering Skin</p>	 <p>Happy Fourth of July!</p>	<p>10:15 – 10:30: Organizational Meeting</p> <p>10:30 – 11:00: Dalia Leibowitz: Medtronic Surgical Team</p> <p>11:00 – 11:30: Yifan Yin: Introduction to Spincasting and the Spincasting Experiment</p> <p>11:30 – 12:00: Alex Wang: Spincasting Journal Paper</p> <p>12:00 – 12:30: Lunch</p> <p>12:30 – 1:00: Dr. Kuan-Che Feng: Excel Tutorial</p> <p>1:00 – 1:15: Distribution of Boxes</p> <p>1:15 – 4:15: Spincasting Experiment Part I</p>	<p>10:15 – 10:30: Organizational Meeting</p> <p>10:30 – 11:15: Robert J. Harrison: Computational Chemistry</p> <p>11:15 – 4:15: Spincasting Experiment Part II</p>	<p>10:15 – 10:20: Organizational Meeting</p> <p>10:20– 11:15: Dr. Michael Hadjiargyrou: Tissue Engineering: A Solution to Organ Regeneration?</p> <p>11:15 – 12:00: Dr. Yuchen Zhou: Solar Cells</p> <p>12:00 – 1:00: Pizza Working Lunch & Statistics Lesson</p> <p>1:00 – 2:00: Prof. Steve Greenbaum: NMR and Battery Research</p>



Summer Scholar Schedule of Weekly Activities

Each day starts with a mandatory group meeting at 10:15 AM!

Daily Schedule: Week of 7/10

Monday – 7/10	Tuesday – 7/11	Wednesday – 7/12	Thursday – 7/13	Friday – 7/14
<p>10:15 – 10:20: Organizational Meeting</p> <p>10:20 – 11:00: Dr. David Sprouster: Non-Destructive Microstructural Analysis of Materials</p> <p>11:00 – 1:00: Battle of the Groups: Spincasting Presentations</p> <p>1:00 – 1:30: Lunch</p> <p>1:30 – 2:30: Dr. Steve Larson, ERDC</p> <p>2:30 – 3:15: Dr. Chander Sadasivan: Minimally Invasive Methods for Treatment of Brain Aneurysms</p> <p>3:15 – 4:00: Dr. Mauro Zammarano, NIST: Flame Retardants</p> <p>4:00 – 4:30: Dr. Jonathan Sokolov: Vacuum and Ellipsometry</p>	<p>10:15 – 10:20: Organizational Meeting</p> <p>10:20 – 11:10: Dr. Richard Clark: RBC Aggregation Vasculopathy: A Pathobiology Model of Burn Injury Progression</p> <p>11:10 – 11:45: Safety Quiz Take II</p> <p>Presentation of Projects</p> <p>11:45 – 12:30: Robert Wong and Gersappe Group</p> <p>12:30 – 1:00: Lunch</p> <p>1:00 – 1:45: Dr. Brooke Ellison: Ethics and Sustainability in the Sciences</p> <p>1:45 – 4:15: Aaron Sloutski; Jonathan Sokolov; Kuan-Che Feng; Yu-Chung Lin; Pawel Polak; Yifan Yin</p>	<p>10:15 – 10:20: Organizational Meeting</p> <p>10:20 – 10:30: Elizabeth Zhang: ReGroup Student Magazine</p> <p>10:30 – 11:30: Dr. Steve Walker: Bacteria</p> <p>Presentation of Projects</p> <p>11:30 – 12:30: Haoyan Fang & MD Farabi Rahman; Yiwei Fang; Shi Fu; Adam Hansen</p> <p>12:30 – 1:15: Lunch</p> <p>1:15 – 1:45: Chakraborty Lab; David Sprouster</p> <p>1:45 – 4:15: Selection of Projects</p> <p>5:30 – 9:00: Celtic Quest Fishing and Dinner</p> 	<p>10:15 – 10:30: Organizational Meeting</p> <p>10:30 – 11:15: Dr. Ying Liu: SOP Writing</p> <p>11:15 – 4:15: Lab Work! (According to your group's schedule)</p> <p>4:30 – 6:30: Softball Game! Feat. Dunkin' Donuts and Baskin Robbins</p>	<p>10:15 – 10:20: Organizational Meeting</p> <p>10:20 – 12:00: Journal Club</p> <p>12:00 – 1:00: Pizza Working Lunch</p> <p>1:00 – 2:00: Optional Meeting: ReCell Tissue Constructs for Burns</p> <p>12:00 – 2:00: Lab Work! (According to your group's schedule)</p>



Summer Scholar Schedule of Weekly Activities

Each day starts with a mandatory group meeting at 10:15 AM!



Daily Schedule: Week of 7/17

Sunday – 7/16:	Monday – 7/17	Tuesday – 7/18	Wednesday – 7/19	Thursday – 7/20	Friday – 7/21
<p>Trip to BNL Summer Sundays Center for Functional Nano-materials</p> <p>Feat. Bagel Lunch (9AM – 3PM)</p>	<p>10:15 – 10:30: Organizational Meeting</p> <p>10:30 – 11:15: Optional Meeting: Dr. Eric Lee, MD: Ketamine and Psychiatry</p> <p>10:30 – 4:15: Lab Work! (According to your group's schedule)</p>	<p>10:15 – 10:30: Organizational Meeting</p> <p>10:30 – 11:00: Jonathan Sokolov: Using ImageJ</p> <p>10:30 – 11:00: Dr. Jack Fuhrer, MD: Medical School Admissions</p> <p>11:00 – 4:15: Lab Work! (According to your group's schedule)</p>	<p>10:15 – 10:30: Organizational Meeting</p> <p>10:30 – 4:15: Lab Work! (According to your group's schedule)</p>	<p>10:15 – 10:30: Organizational Meeting</p> <p>10:30 – 11:00: Dr. Patrick M. Lloyd, DDS, MS: Dental School Admissions</p> <p>11:00 – 12:00: Dr. Michelle Hutchins: VIPER Program, UPenn</p> <p>12:00 – 4:15: Lab Work! (According to your group's schedule)</p>	<p>10:15 – 10:30: Organizational Meeting</p> <p>10:30 – 12:00: Research Updates: DISC, Cuiffo Group, Cell Sort, Greenhouse, Shi Fu Group</p> <p>12:00 – 1:00: Pizza Working Lunch</p> <p>1:00 – 2:00: Donna Tuminello: All About Patents</p> <p>12:00 – 2:00: Lab Work! (According to your group's schedule)</p>

Summer Scholar Schedule of Weekly Activities

Each day starts with a mandatory group meeting at 10:15 AM!


Daily Schedule: Week of 7/24

Sunday – 7/23:	Monday – 7/24	Tuesday – 7/25	Wednesday – 7/26	Thursday – 7/27	Friday – 7/28
<p>Trip to BNL Summer Sundays NSLS-II Tour</p> <p>Feat. Bagel Lunch & LI Llama Farm and Yarn (9AM – 3PM)</p>	<p>10:15 – 10:30: Organizational Meeting</p> <p>10:30 – 11:00: Philip Ball: Remaking Ourselves – Technologies of Flesh and the Futures of Selfhood</p> <p>11:00 – 4:15: Lab Work! (According to your group's schedule)</p>	<p>10:15 – 10:30: Organizational Meeting</p> <p>10:30 – 4:15: Lab Work! (According to your group's schedule)</p>	<p>Educational Outing: 9/11 Memorial and Museum</p>  <p>Feat. Bravo Pizza</p>	<p>10:15 – 10:30: Organizational Meeting</p> <p>10:30 – 11:00: Dr. Sharon Nachman MD: Pathology of Tick Bites</p> <p>11:00 – 4:15: Lab Work! (According to your group's schedule)</p>	<p>10:15 – 10:30: Organizational Meeting</p> <p>10:30– 12:00: Research Updates: Deng Groups, Thrombosis Group, Harrison Group, Kim DISC Group, Wong Group</p> <p>12:00 – 1:00: Annual Outdoor Garcia BBQ</p>  <p>12:00 – 2:00: Lab Work! (According to your group's schedule)</p>

Summer Scholar Schedule of Weekly Activities

Each day starts with a mandatory group meeting at 10:15 AM!

Daily Schedule: Week of 7/31



	Monday – 7/31	Tuesday – 8/1	Wednesday – 8/2	Thursday – 8/3	Friday – 8/4
	<p>10:15 – 10:20: Organizational Meeting</p> <p>10:20 – 10:45: Deng Group Presentations</p> <p>10:45 – 4:15: Lab Work! (According to your group's schedule)</p>	<p>Annual Canoe Expedition!</p>  <p>3:00 – 4:15: Lab Work! (According to your group's schedule)</p>	<p>10:15 – 10:30: Organizational Meeting</p> <p>10:30– 11:15: Professor Kaiming Ye, Biomedical Engineering, Binghamton University</p> <p>11:15 – 4:15: Lab Work! (According to your group's schedule)</p>	<p>10:15 – 10:30: Organizational Meeting</p> <p>10:30 – 4:15: Lab Work! (According to your group's schedule)</p>	<p>10:15 – 10:30: Organizational Meeting</p> <p>10:30 – 2:00: Lab Work! (According to your group's schedule)</p> <p>12:00 – 1:00: Working Pizza Lunch</p>



Summer Scholar Schedule of Weekly Activities

Each day starts with a mandatory group meeting at 10:15 AM!

Daily Schedule: Week of 8/7

Sunday – 8/6	Monday – 8/7	Tuesday – 8/8	Wednesday – 8/9	Thursday – 8/10	Friday – 8/11
<p>Garcia Outing: Escape Room!</p> <p>Escape Room LI, Ronkonkoma</p> <p>Feat. Garcia Pizza Dinner (6-9pm)</p>	<p>10:15 – 10:20: Organizational Meeting</p> <p>10:20 – 11:00: Dr. Samantha Luker – Biopolymers and Soil</p> <p>11:00 – 4:15: Lab Work! (According to your group's schedule)</p> <p>4:30 – 6:00: Ice Cream Social and Student Research Updates</p>	<p>10:15 – 10:30: Organizational Meeting</p> <p>10:30 – 4:15: Lab Work! (According to your group's schedule)</p> <p>3:30 – 4:30: Ice Cream Social and Student Research Updates</p>	<p>10:15 – 10:30: Organizational Meeting</p> <p>10:30– 11:15: Marla Boots: Materials Research Society (MRS) Fall Meeting</p> <p>11:15 – 4:15: Lab Work! (According to your group's schedule)</p>	<p>10:15 – 10:30: Organizational Meeting & Vote for Best REU + Grad Student</p> <p>10:30 – 4:15: Lab Work! (According to your group's schedule)</p> <p>3:30 – 4:30: Ice Cream Social and Student Research Updates Feat. Mr Softee!</p> 	 <p>Garcia End-of-Summer Research Symposium!</p>



Please join us in person or via [Zoom](#) for the

Garcia 2023 Research Symposium
Friday, August 11th, 10:15 am – 1:00 pm
SAC Auditorium, Stony Brook University
Coffee and Luncheon : SAC Ballroom A

Greeting by:

Steven Vaccarelli, Trust Officer
Brown Brothers Harriman Trust
Company, N.A. Representing the
Louis Morin Charitable Trust

Musical Arrangement by
Garcia 2023 Students

directed by **Prof. John Jerome**

Guest Speaker:

Dr. Brooke Ellison, PhD, MPP
Noted author, ethicist, and professor
Renaissance School of Medicine
Stony Brook, NY

Research Projects Presented
by Garcia 2023 Students

Please RSVP by 8/8/2023 at: <https://bit.ly/garcia2023symposium> **Contact us: 516 458**

9011

2023 Garcia Program End-of-Summer Research Symposium



"This year, the Garcia logo has been designed to capture the essence of connection that lies at the heart of Garcia. Just as many monomers join to form a polymer, at Garcia, individuals of diverse backgrounds, experiences, and disciplines join efforts to work towards the exciting goal that is scientific innovation. The meaningful skills, knowledge, and relationships we gained over the summer will forever be cherished. Thank you Garcia 2023 for such an unforgettable experience!" **Hannah Oh '23**

10:15 AM Coffee and muffins in Ballroom A	Musical Arrangement: Conducted by Prof. John Jerome <i>Garcia POPS arrangement</i>
10:25 AM	Welcome Mr. Steven Vaccarelli, Vice President, Senior Trust Officer Brown Bros Harriman and the Morin Charitable Trust
	Keynote Address Professor Brooke Ellison, Stony Brook University
10:35 AM	Session 1: Machine Learning, Theory, and AI Chair: Bernard Essuman & Eugene Jiang, SBU
	Machine Learning Approach to Time-Series Analysis of SARS-CoV-2 Spike Glycoproteins Under Varying pH and Temperature Conditions Parth Jain , Bergen County Academies, Hackensack, NJ Melvin Thu , John L. Miller Great Neck North High School, Great Neck, NY
	Application of a Novel Generative AI network for Cancer Drug Discovery Using the eIF4E protein Melvin Thu , John L. Miller Great Neck North High School, Great Neck, NY Parth Jain , Bergen County Academies, Hackensack, NJ Anirudh Srinivasan , duPont Manual High School, Louisville, KY
	Quantifying the Lennard-Jones Potential between Two Hard Ellipsoids Using Coarse-Grained Deep Learning Techniques Erin Wong , Great Neck South High School, Great Neck, NY Dylan Fei , Jericho Senior High School, Jericho, NY
	Convolutional Autoencoder and Extended Dynamic Mode Decomposition for Koopman Operator-based Markov chaining for Time Series Forecasting of a Large-Scale Dissipative Particle Dynamic System Thrombosis Akhil Samavedam , Westlake High School, Austin, TX
	Creating a 3D Manifold to Determine Molecular Weight and Thickness of Spin-coated Polystyrene Samples Alexander Wang , Sewickley Academy, Sewickley, PA Samuel Chen , Ed W. Clark High School, Las Vegas, NV Matthew Chang , Woodbridge High School, Irvine, CA Anthony Zhu , Barrington High School, Barrington, IL

	<p>Using Digital Image Speckle Correlation to Identify Micro Emotions</p> <p>Hyeonji (Tiffany) Ahn, St. Mark's School, Southborough, MA Elaina Heghes, South Side High School, Rockville Centre, NY Gyulim (Jessica) Kang, Singapore American School, Singapore Anusha Misra, Dana Hills High School, Dana Point, CA Shirley Xiong, Ward Melville High School, East Setauket, NY Elaine Zhang, Jericho High School, Jericho, NY</p>
	<p>Enhanced Emotion Recognition via Deep Learning Integration with Digital Image Speckle Correlation</p> <p>Juni Kim, Stanford Online High School, Redwood City, CA</p>
10:50 AM	<p>Session 2: Clean Energy Generation Chair: Christian Apostol, SBU; Junior Gonzalez, SCCC</p>
	<p>Testing the Potential of Partially Reduced Graphene Oxide (PRGO) as a Catalyst Enhancer</p> <p>Sophia Bracco, South Side High School, Rockville Centre, NY Dominic Rosiello, South Side High School, Rockville Centre, NY Sergio Rosa, South Side High School, Rockville Centre, NY Sam Specht, The Stony Brook School, Stony Brook, NY</p>
	<p>Exploring Self-Assembled Hole Transport Materials in p-i-n Perovskite Solar Cells</p> <p>Hongyi Huang, Shenzhen Middle School, Shenzhen, China Minsik Shin, Seoul International School, Seongnam, South Korea Dongmin Yoon, North London Collegiate School Jeju, Seogwipo-si, South Korea</p>
	<p>Enhancement of Anion Exchange Membrane Fuel Cells by Functionalizing Micro cellulose with Partially Reduced Graphene Oxide</p> <p>Kenneth Chang, Great Neck South High School, Great Neck, NY Richard Chen, Andover High School, Andover, MA Raymond Wang, Casa Grande High School, Petaluma, CA</p>
	<p>Study of Silver Nanoparticles Deposition on Proton Exchange Membrane Fuel Cells</p> <p>Prisha Jain, Irvington High School, Fremont, CA Anna Heimowitz, SKA High School for Girls, Hewlett, NY Jonathan Sacolick, HAFTR High School, Cedurhurst, NY Haichuan Wang, Shanghai Jianping High School, Shanghai, China</p>
	<p>Investigating the Effect of ZnO Deposition on Alkaline Anion Exchange Membrane Fuel Cells</p> <p>Kriste An, Harvard-Westlake School, Studio City, CA Samuel Chen, Ed W. Clark High School, Las Vegas, NV Rohan Suri, Ladue Horton Watkins High School, St. Louis, MO</p>
11:00 AM	<p>Session 3: Ethical Considerations in Science and Engineering Chair: Sheldon Liu and Pranav Kota</p>

	<p>An authentic life: on the ethics of providing gender-affirming care for youth through the framework of ethical care</p> <p>Boheng Cao, North Hollywood High School, North Hollywood, CA Jude Ouerfelli, Fort Lee High School, Fort Lee, NJ Adam Zaidi, San Francisco University High School, San Francisco, CA</p>
	<p>Examining the effects of implicit bias in healthcare and potential solutions</p> <p>Ethan Lai, Phillips Academy, Andover, MA Michael Wang, Mounds View High School, Arden Hills, MN Elaine Zhang, Jericho High School, Jericho, NY</p>
	<p>Ethics of Germline Genome Editing (GGE) for Therapeutics</p> <p>Sai Pranav Kota, Cedar Falls High School, Cedar Falls, IA Rohan Suri, Ladue Horton Watkins High School, St. Louis, MO</p>
	<p>The Use of Prenatal Screening to Select Against Disorders and Disability</p> <p>Dvita Bhattacharya, Kent Place School, Summit, NJ Aditi Kiran, Basis Independent Fremont, Fremont, CA</p>
	 <p>Science Fun Video: Histones Selina Zhang</p>
11:15 AM	<p>Session 4: Biomechanics & Stem Cell Differentiation Chair: Jason Goldstein, RPI and Rosario Grasso, SBU</p>
	<p>The Decellularization of Tissue Samples Using Supercritical Carbon Dioxide</p> <p>Jason Goldstein, Rensselaer Polytechnic Institute, Troy, NY</p>
	<p>Osteogenic Differentiation of Dental Pulp Stem Cells via Titanium Deposition in Static Magnetic Field</p> <p>Ethan Lai, Phillips Academy, Andover, MA Michael Wang, Mounds View High School, Arden Hills, MN Aman Yarlagadda, Newman Smith High School, Carrollton, TX</p>
	<p>Neurogenic Differentiation of Micro-spheric Dental Pulp Stem Cells via Poly-lactic Acid and Poly(4-vinylpyridine) with Resorcinol Diphosphate Coated Clay</p> <p>Dvita Bhattacharya, Kent Place School, Summit, NJ Catherine Chun, Ardsley High School, Ardsley, NY Anita Gaenko, Huron High School, Ann Arbor, MI Alexander Wang, Sewickley Academy, Sewickley, PA Adam Zaidi, San Francisco University High School, San Francisco, CA</p>
	<p>Analyzing the Impact of Aging, Cholesterol Inhibition, and Substrate Characteristics on Human Dermal Fibroblasts</p> <p>Samuel Coopersmith, Casa Grande High School, Petaluma, CA Sharis Hsu, Valley Christian High School, San Jose, CA Sai Pranav Kota, Cedar Falls High School, Cedar Falls, IA Pia Sodhi, The Brearley School, New York City, NY Avi Talsania, Sachem High School North, Ronkonkoma, NY Richard Wong, Plainview-Old Bethpage John F. Kennedy High School, Plainview, NY</p>

11:25 AM	<p>Session 5: TiO₂ Nanotoxicology Chair: Maddie Freilich</p>
	<p>(a) Impact of TiO₂ Nanoparticles and RECELL™ on Tissue-Engineered Human Skin Constructs Engrafted in Mice Models (b) Analyzing the Effects of Titanium Dioxide Nanoparticles on Angiogenesis (c) Analyzing the Impacts of Titanium Dioxide Nanoparticles on the Upregulation of EGFP. Caitlyn Limbert, British School Jakarta, Jakarta, Indonesia Sahana Dhama, The Wheatley School, Old Westbury, NY Menachem Lotwin, Rambam Mesivta, Lawrence, NY Jacqueline Han, Great Neck South High School, Great Neck, NY Grace Wang, Detroit Country Day School, Beverly Hills, MI Chunuo Chu, Shenzhen Middle School, Shenzhen, Guangdong Annika Joshi, Johns Creek High School, Johns Creek, GA</p>
	<p>Keratinocyte Uptake of Titanium Dioxide Nanoparticles Effect on Cell Differentiation and Proliferation Ashley Huang, Syosset High School, Syosset, NY Derek Zhang, The Wheatley School, Old Westbury, NY</p>
11:35 AM	<p>Session 6: X-Ray Analysis of Materials Chair: Brooklyn Ratel, Sahaana Kesavan, SBU</p>
	<p>Utilizing Machine Learning to Predict Sinusitis Through the Segmentation of Maxillary Sinus Images Anirudh Srinivasan, duPont Manual High School, Louisville, KY</p>
	<p>Advanced X-Ray Characterization of Fusion Materials Anthony Zhu, Barrington High School, Barrington, IL Michael Zhang, Livermore High School, Livermore, CA Ryan Kim, Thomas Jefferson High School for Science and Technology, Alexandria, VA</p>
11:40 AM	<p>Session 7: Fibrinogen & Thrombosis Chair: Megha Gopal, SBU and Rachel Na, Washington University</p>
	<p>In-Silico Studies on Fibrinogen Domain Adsorption on Polylactic Acid Matthew Sun, North Carolina School of Science and Mathematics, Durham, NC Erin Wong, Great Neck South High School, Great Neck, NY Richard Zhang, Conestoga High School, Berwyn, PA</p>
	<p>Thrombosis: An Analysis of Pseudo-thrombi to Understand Collagen-fibrin Interaction Sripradha Manikantan, James Logan High School, Union City, CA</p>
	<p>Viability of a Novel Peptide P12 as an Antithrombotic Agent Samuel Coopersmith, Casa Grande High School, Petaluma, CA Sharis Hsu, Valley Christian High School, San Jose, CA Sai Pranav Kota, Cedar Falls High School, Cedar Falls, IA Pia Sodhi, The Brearley School, New York City, NY Avi Talsania, Sachem High School North, Ronkonkoma, NY Richard Wong, Plainview-Old Bethpage John F. Kennedy High School, Plainview, NY</p>

	<p>Solving the Time-Independent Schrödinger Equation for Simple Systems, by Projection into a Finite Legendre Polynomial Basis Daniel Lai, High School Affiliated to Renmin University of China, Beijing, China Aman Thawani, Great Neck South High School, Great Neck, NY</p>
	 Science Fun Video: Ziplock and water experiment – Lamia Ayaz
	<p>Session 8: Chitosan Matrices Chair: Jacob Zerykier, MIT</p>
11:55 AM	<p>Synthesizing Gold Nanoparticles on Chitosan-Coated Stainless Steel Characterizing Adhesive Complex Formed with Deweaved Cotton Fibers and Chitosan Solution Daniel Lu, Westview High School, San Diego, CA Harjaisal Brar, Stockdale High School, Bakersfield, CA Claire Kang, Canyon Crest Academy, San Diego, CA</p>
	<p>Session 9: 3-D Printing and Materials Design Chair: Briman Yang, SBU and Alex Samadi, Virginia Tech</p>
12:00 PM	<p>Designing a Mobile Base for a Mobile Manipulator Peter Elmer, High School for Math, Science and Engineering at City College, New York, NY Eleanor Yang, Evergreen Valley High School, San Jose, CA</p>
	<p>A Cross Platform Transfer Alex Samadi, Virginia Polytechnic Institute and State University, Blacksburg, Virginia Junior Gonzalez, Suffolk County Community College, Selden, New York Arianna Roland, Patchogue Medford High School, Patchogue, NY</p>
	<p>Robotic Vision: 3D Object Orientation Detection Algorithms Brandon Cai, Parkland High School, Allentown, PA</p>
	<p>Bioprinting Hydrogels for Dentin Pulp Regeneration and Disinfection Saranya Anantapantula, Spring-Ford Area High School, Royersford, PA</p>
	<p>Mechanical Property and Cell-Adhesion Characterization of Poly(vinyl alcohol) and Resorcinol Diphenyl Phosphate Clay Blend Hydrogels Hannah Oh, Chadwick International, Incheon, South Korea Leora Stochel, Hebrew Academy of Nassau County, Uniondale, NY Haoyu Xu, Hangzhou Foreign Language School CAL Center, Hangzhou, China</p>
	<p>Engineering a Thermally and Electrically Conducted, Mechanically Sustainable Nanocomposite via 3D Printing Xuyi Zhou, Shanghai Pinghe School, Shanghai, China</p>
12:15 PM	<p>Session 10: Biopolymers & Surfaces Chair: Ruth Pereira, SBU</p>

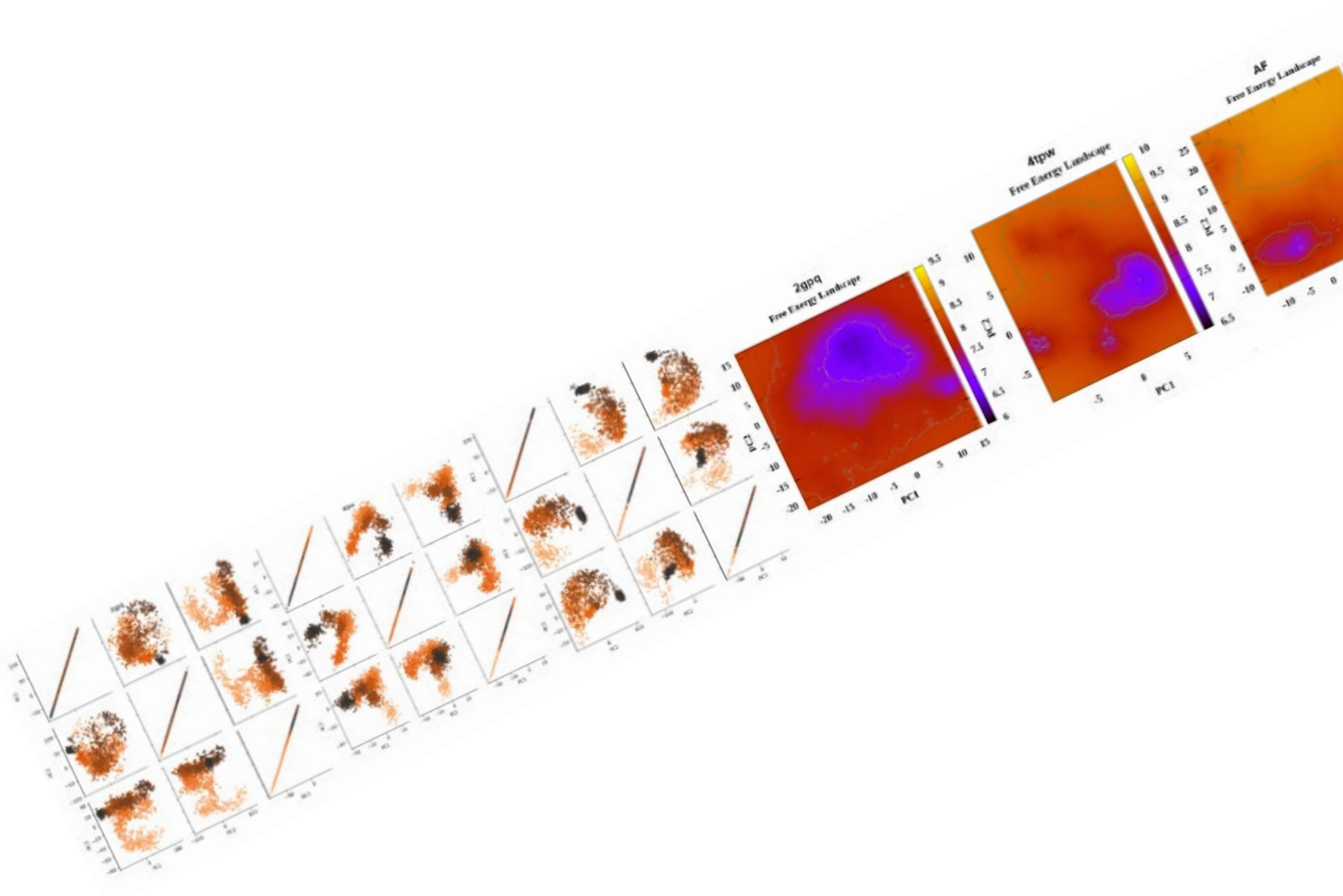
	<p>Engineering a Reverse Thermo-Responsive, Cross-Linkable, Biodegradable Liquid Embolic Agent for Brain Aneurysm Treatment</p> <p>Lamia Ayaz, Howard High School, Ellicott City, MD Hannah Feng, Torrey Pines High School, San Diego, CA Ruoxi Jin, Beijing National Day School, Beijing, China Ann Lee, Seoul International School, Seoul, South Korea Sheldon Liu, Stuyvesant High School, New York, NY Evan Pang, Mission San Jose High School, Fremont, CA Jiarui Peng, East Lyme High School, East Lyme, CT Grace Qiao, The Experimental High School Attached to Beijing Normal University, Beijing, China</p>
	<p>Rhizobium Tropici-Produced EPS Biopolymer: Chemical Analysis and Impact on Bermuda Grass Root Growth</p> <p>Haaris Alam, Portola High School, Irvine, CA Isana Alicea, Patchogue Medford High School, Medford, NY Brinley Dai, The Experimental High School Attached to Beijing Normal University, Beijing, China Jerry Gao, Beijing No. 80 High School, Beijing, China Ashritha Kalakuntla, Ed W. Clark High School, Las Vegas, NV Tei Kim, Stanford Online High School, Redwood City, CA Elise Ngo, Portola High School, Irvine, CA Tony Guo Feng Tung, Shanghai High School International Division, Shanghai, Shanghai, China</p>
	<p>Molecular Dynamics Simulations of Soil-Strengthening Hydrogels</p> <p>Emily Sun, Westford Academy, Westford, MA</p>
	<p>A Novel DNA Ligase-based Soft Lithographic Approach to Ordered DNA Fragmentation</p> <p>Selina Zhang, North Hunterdon High School, Annandale, NJ Jude Ouerfelli, Fort Lee High School, Fort Lee, NJ Aditi Kiran, Basis Independent Fremont, Fremont, CA Alex Zheng, Stuyvesant High School, New York City, NY Boheng Cao, North Hollywood High School, North Hollywood, CA Ellen Hu, C. Leon King High School, Tampa, FL</p>
	<p>In silico study of the temperature effect on binding dynamics between SARS-CoV-2 spike glycoprotein and polylactic acid surface</p> <p>Matthew Chang, Woodbridge High School, Irvine, CA</p>
	 <p>Science Fun Video: The ruler experiment Adam Zaidi</p>
12:30 PM	<p>Formal Buffet Luncheon</p>
	 <p>Please proceed to Ballroom A for musical arrangement and luncheon catered by Wing Wan of West Hempstead</p>

*We gratefully acknowledge support
from
the Louis Morin Charitable Trust
and ICL Group*

Session 1:

Machine Learning and Artificial Intelligence

Chairs: Ziyuan Niu and Karin Hasegawa



Machine Learning Approach to Time-Series Analysis of SARS-CoV-2 Spike Glycoproteins Under Varying pH and Temperature Conditions

Parth Jain¹, Melvin Thu², Ziyuan Niu³, Yuefan Deng³

¹ Bergen County Academies, Hackensack, NJ 07601, ² Great Neck North High School, Great Neck, NY 11023, ³ Stony Brook University, Stony Brook, NY 11790

The SARS-CoV-2 global pandemic continues to pervade many aspects of life and it remains crucial to assess the effects of environmental factors, namely temperature and pH, on the virus's molecular composition and structure. Molecular dynamics (MD) simulations are commonly utilized in modeling these nanoscale interactions, but their high computational complexity indicates their inefficiency and inadequacy for larger scale modeling applications over longer time intervals. The primary goal of this research is to develop a machine learning (ML) approach with supervised training on nanosecond SASA (solvent accessible surface area) MD simulation data for predicting properties of SARS-CoV-2 spike glycoproteins. A protein's SASA values quantify the surface characterized around a protein. Changes in these values over time have implications for the protein's stability and folding capabilities and allow for a greater understanding of the virus's pathogenicity under specific conditions. ^[1]

Our data will be primarily denoised and processed with fast Fourier transforms (FFT). These allow us to convert the SASA time-series data from a time-domain representation to a frequency-domain representation and identify cyclic behavior. Machine learning models including the k-nearest neighbors (k-NN) algorithm, a long short-term memory neural network (LSTM), and a convolutional neural network (CNN) will subsequently be trained on 1000 ns of MD simulation data to predict changes in the spike glycoprotein's SASA values as a function of time. Future *in vitro* experiment results will be able to validate the accuracy of the ML models for long-term predictions.

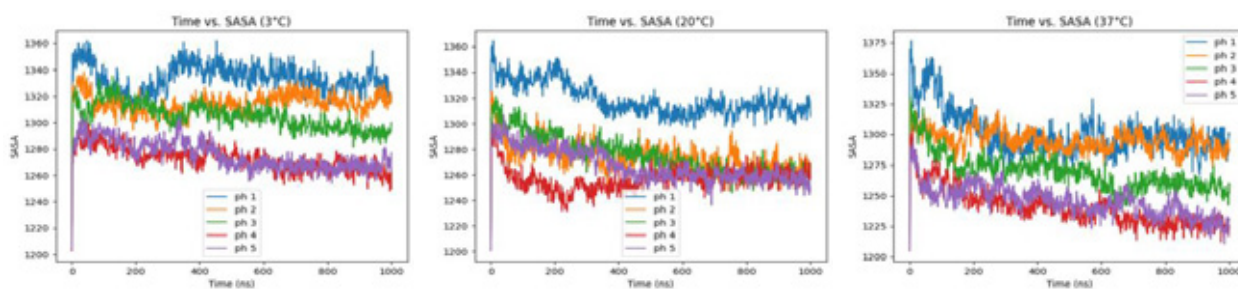


Figure 1: Time-series plots of SASA values from MD simulations prior to fast Fourier transform denoising

^[1] Ali, Syed Ausaf et al. "A review of methods available to estimate solvent-accessible surface areas of soluble proteins in the folded and unfolded states." *Current protein & peptide science* vol. 15,5 (2014): 456-76. doi:10.2174/1389203715666140327114232

Application of eIF4E Protein-Ligand Modeling for Cancer Drug Discovery

Melvin Thu¹, Parth Jain², Anirudh Srinivasan³, Evan Xie⁴, Giorgos Kementzidis⁵, Karin Hasegawa⁵, Yuefan Deng⁵

¹Great Neck North High School, Great Neck, NY 11023, ²Bergen County Academies, Hackensack, NJ, 07601, ³duPont Manual High School, Louisville, KY 40208, ⁴The Pingry School, Basking Ridge, NJ 07920, ⁵Stony Brook University, Stony Brook, NY 11790

The eIF4E complex recruits ribosomal subunits (40S) to initiate translation and is composed of the eIF4E, eIF4G, and eIF4A subunits. eIF4E is the cap-binding protein and binds to the m⁷gtp mRNA 5' cap. eIF4G is the scaffolding protein in the complex and binds eIF4E.

The protein 4E-BPs can bind to eIF4E where eIF4G binds to prevent the eIF4F complex from forming. eIF4F plays a substantial role in cancers since eIF4F preferentially activates the translation of certain mRNAs, encoding proliferation and survival-promoting proteins such as cyclin D1, c-Myc, and VEGF. The pathway involving PI3K phosphorylation of 4E-BPs resulting in the unbinding of eIF4E from 4E-BPs and the formation of the eIF4F complex results in breast, lung, ovarian, and prostate cancers, and the pathway involving Ras phosphorylation of eIF4E results in the formation of an active eIF4F complex and results in pancreatic, lung, and colorectal cancers.

Our approach to eIF4E inhibition involves designing a residue to restrain the movement of key eIF4E residues involved in the binding of eIF4E to m⁷GTP, such as W102, W56, and E103, to prevent binding. An issue with m⁷GTP analogues of similar structure and stronger binding affinity, however, is that many are negatively charged and thus can't pass through cell membranes. Molecular docking simulations can predict binding orientation and binding affinity of the ligand to target, producing samples of many ligand conformations in the target binding region to find the optimal conformation. However, high throughput screening through brute force molecular docking is computationally expensive and limited as there are only 10¹⁰ known compounds as opposed to the 10⁶⁰ total compounds.

In order to design an effective ligand, we first have to study the structure of eIF4E, and investigate how key residues involved in eIF4E binding to m⁷GTP undergo conformational change with and without m⁷GTP. We optimize eIF4E models without m⁷GTP using principal component analysis (PCA) and free energy landscape (FEL) calculations. We performed PCA on the trajectory data of 2gppq, 4tpw, and AF protein sources of eIF4E to transform the set of possibly correlated variables (the positions of the protein atoms) into a set of values of linearly uncorrelated variables (the principal components). We also calculated FEL of the 2gppq, 4tpw, and AF protein sources of eIF4E using GROMACS. FEL is a graphical representation of the thermodynamically stable states of a protein and the transitions between them where the local minima represent the most stable protein conformations and the barriers represent the transition states. We are working on molecular docking simulations for eIF4E binding to m⁷GTP.

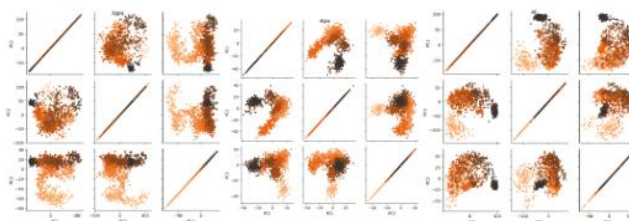


Figure 1. PCA analysis (left) of 2gp, 4tpw, and AF (left to right).
Graphic by author.

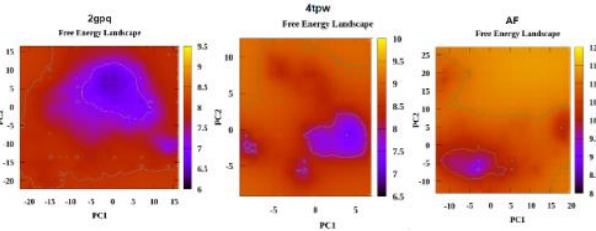


Figure 2. FEL (right) of 2gp, 4tpw, and AF (left to right).
Graphic by author.

Quantifying the Lennard–Jones Potential between Two Hard Ellipsoids Using Coarse-Grained Deep Learning Techniques

Erin Wong¹, Dylan Fei², Georgios Kementzidis³, Ziji Zhang³, Yuefan Deng³

¹ Great Neck South High School, Great Neck, NY 11020, ² Jericho Senior High School, Jericho, NY 11753, ³ Department of Applied Mathematics & Statistics, Stony Brook University, Stony Brook, NY 11794

Classical molecular dynamics (MD) is a highly intensive, $O(n^2)$, computational method for simulating the kinetics, thermodynamics, and structural properties of a many-body system over time. The Lennard–Jones potential (LJP), subsuming a set of energy functions that regulate the dynamics of the particles in an MD simulation, governs the van der Waals (vdW) energetics between neighboring particles. We seek to modify the potential’s conventional form, eq. (1), which fails to accurately model the vdW forces between large and anisotropic particles. Eq. (3), however, overcomes those shortcomings by treating the ellipsoids as a collection of uniformly distributed points and, in turn, applying a double summation over those points to generate the LJP.

$$U_{LJ} = 4\epsilon_{LJ} \left[\left(\frac{\sigma}{r} \right)^{12} - \left(\frac{\sigma}{r} \right)^6 \right]$$

Eq. (1) — 12-6 Lennard-Jones potential — [1]

$$V_{AB} = 4\epsilon_{AB} \left\{ \left(\frac{\sigma^0}{R_{AB} - \sigma_{AB} + \sigma^0} \right)^{12} - \left(\frac{\sigma^0}{R_{AB} - \sigma_{AB} + \sigma^0} \right)^6 \right\}$$

Eq. (2) — Gay-Berne potential — [2]

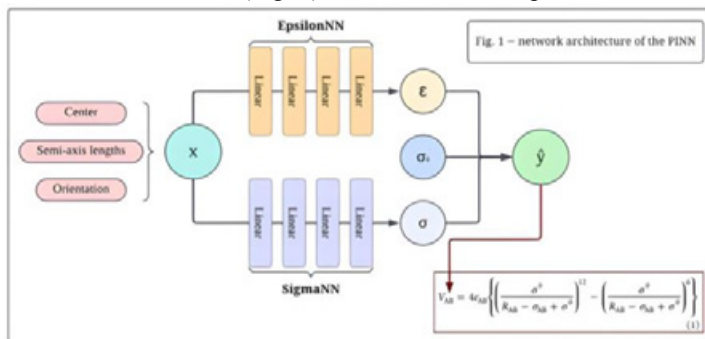
$$U = \sum_{i \in \text{Body 1}} \sum_{j \in \text{Body 2}} U_{LJ}(r_{ij})$$

Eq. (3) — ground-truth potential — [1]

We learn the parameters to eq. (2) using a physics-informed neural network (PINN), which, unlike a typical feedforward neural network, assumes a physics-principled training process that, in our case, entails the parametrization of eq. (2). Our goal, as shown in Fig. 1, is to replicate the accuracy of eq. (3) by training our PINN to recognize the relationship between the parameters of eq. (2) and the parameters—relative orientation, semi-major/-minor axes, and center—of the two ellipsoids. Our PINN then uses those parameters to generate the corresponding ϵ_{AB} and σ_{AB} values, thereby streamlining the complexity involved in the computation of eq. (3).

Our ground truth, derived from the Monte Carlo approximation of eq. (3), consisted of 2,080,000 potentials, each of which bore a unique permutation of the parameters to eq. (3), where $U_{LJ}(r_{ij})$ denotes the 12–6 LJP. One of the primary concerns about the data’s accuracy was the extent to which an ellipsoid could be classified as a rigid body. Therefore, we ran three mini-experiments to verify the equations and code used to generate the ground truth. We referenced the three cases shown by Paramonov & Yaliraki and demonstrated (a) that the number of points per ellipsoid, upon exceeding 15,000, minimally impacted the generated potential, U , and (b) that ground truth generation code proved scientifically sound, emulating the well depth and curvature in all three cases shown by Paramonov and Yaliraki [3]. Moreover, in addressing part (a), we randomly sampled a subset of our ground truth (generated using 30,000 points per ellipsoid) and regenerated those LJP values using 1,000, 15,000, 25,000, and 30,000 points. The mean absolute percentage error (MAPE) started at 1.48% for 1,000 points, but upon exceeding 15,000 points, gradually decreased to 0.96% ($\text{MAPE}_{30,000}$), confirming the accuracy of our ground truth.

We implemented two models using this ground truth. The first was a black box model, which used the parameters of two ellipsoids to predict the LJP. The second was a PINN (Fig. 1) that used the same parameters of the two ellipsoids to find the coefficients of ϵ and σ through two separate neural networks and tune σ_0 for eq. (1). By employing a combination of Adam and L-BFGS optimization, the PINN was able to achieve a minimum training loss of 0.0004 over 250 epochs. We plan to both validate this PINN using a separate testing dataset and further improve upon it by investigating the use of other activation and loss functions.



1. Everaers, R., and M. R. Ejtehadi. "Interaction Potentials for Soft and Hard Ellipsoids." *Physical Review E*, vol. 67, no. 4, 21 Apr. 2003, <https://doi.org/10.1103/physreve.67.041710>.
2. Tillack, Andreas F., et al. "Systematic Generation of Anisotropic Coarse-Grained Lennard-Jones Potentials and Their Application to Ordered Soft Matter." *Journal of Chemical Theory and Computation*, vol. 12, no. 9, 8 Aug. 2016, pp. 4362-74, <https://doi.org/10.1021/acs.jctc.6b00219>.
3. Paramonov, Leonid, and Sophia N. Yaliraki. "The Directional Contact Distance of Two Ellipsoids: Coarse-grained Potentials for Anisotropic Interactions." *The Journal of Chemical Physics*, vol. 123, no. 19, 15 Nov. 2005, <https://doi.org/10.1063/1.2102897>.

Solving the Time-Independent Schrödinger Equation for Simple Systems, by Projection into a Finite Legendre Polynomial Basis

Daniel Lai^{1,†}, Aman Thawani^{2,†}, Robert Harrison^{3,*}

¹ High School Affiliated to Renmin University of China, Beijing 100080, China; ² Great Neck South High School, Great Neck, NY 11020; ³ Institute for Advanced Computational Science, Stony Brook University, Stony Brook, NY 11794; [†] These authors contributed equally to this work; * Corresponding author (robert.harrison@stonybrook.edu).

ABSTRACT

Solving the time-independent Schrödinger equation provides first principles insight into the structural and electronic properties of atoms and molecules, which has pivotal implications in chemistry and materials science¹. Approximation is necessary to solve the equation as it is often too complex to solve analytically. A common technique used to approximate a solution to the time-independent Schrödinger equation is the finite basis method, which approximates the wavefunction as a finite linear combination of less computationally demanding “basis functions” from a chosen basis set, and thus reducing the complex partial differential equation to a linear algebraic problem². Legendre polynomials have demonstrated promising results as a basis set in diverse applications^{3,4,5}, and thus were selected as the basis set in this study. These functions possess many desirable properties, such as orthogonality, being easily differentiable, and compatibility with Gauss-Legendre quadrature, a numerical integration method that takes advantage of the orthogonality of Legendre polynomials⁵.

Using the finite basis method, we can solve for the ground state wavefunction and energy of simple quantum mechanical systems, and in this study we focused on the quantum harmonic oscillator in 1-D. We first projected the wavefunction into the Legendre polynomial basis to obtain integral expressions for the wavefunction overlap, kinetic energy, and potential energy; the expressions were then computed and substituted into an expression for energy, derived from the Schrödinger equation. With the expression for energy represented by a linear combination of the basis functions, we minimized the energy with respect to variation of the coefficients of the linear combination. By doing so, we obtained a set of coefficients for the basis set approximation of the wavefunction that results in minimum energy, which is also the ground state solution for the system’s Schrödinger equation. To minimize the energy function, we implemented various algorithms including the steepest descent method with line search via Newton’s method or the bisection method, and the conjugate gradient method.

We applied this overall method to calculate the ground state energy of the quantum harmonic oscillator in 1-D, with angular frequency $\omega = 2$ and in a simulation box of length $L = 8$. Approximated results for the minimum energy relative to the analytical value of $\omega / 2 = 1$, were within six decimal places with the steepest descent method and within seven decimal places with the conjugate gradient method, using Gauss-Legendre quadrature of order $n = 50$. The approximated wavefunction using the conjugate gradient minimization method is shown along with the exact solution, and the error between them, to the right (**Fig. 1**).

Solving the time-independent Schrödinger equation for the quantum harmonic oscillator system can be used to model photons and the vibrational motion of diatomic molecules. Future directions include solving for more quantum systems such as the “particle in a box”, hydrogenic atoms, and the helium atom.

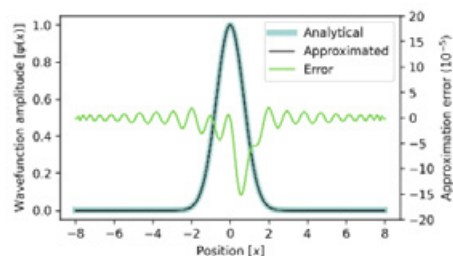


Fig. 1. Plot of analytical and approximated wavefunction amplitude curves for the ground state of the quantum harmonic oscillator in 1-D, with the error shown in green. The ground state was found using the conjugate gradient method. The maximum error was within -1.5×10^{-4} .

¹ E. Cancès, M. Defranceschi, W. Kutzelnigg, C. Le Bris, Y. Maday, in Handbook of Numerical Analysis, Volume 10 (Elsevier, 2003), pp. 3–270.

² R. J. Harrison, G. I. Fann, T. Yanai, Z. Gan, G. Beylkin, Journal of Chemical Physics. 121, 11587–11598 (2004).

³ M. Abdelhakem, H. Moussa, Alexandria Engineering Journal. 66, 301–313 (2023).

⁴ R. J. Harrison et al., SIAM Journal on Scientific Computing. 38, S123–S142 (2016).

⁵ Hwan Pyo Moon, Soo Hyun Kim, S.-H. Kwon, Applied Mathematics and Computation. 451, 127995–127995 (2023).

Utilizing Machine Learning to Predict the Thickness of Spin-Coated Monodisperse Polystyrene Thin Films

Alexander Wang¹, Samuel Chen², Matthew Chang³, Anthony Zhu⁴, Evan Xie⁵, John Jerome⁶, Miriam Rafailovich⁷
¹Sewickley Academy Senior School, Sewickley, PA 15090, ²Ed W. Clark High School, Las Vegas, NV 89102, ³Woodbridge High School, Irvine, CA 92604, ⁴Sewickley, PA 15143, ⁵Barrington High School, Barrington, IL 60010, ⁶The Pingry School, Basking Ridge, NJ 07920, ⁷Department of Mathematics, Suffolk Community College, Selden, NY 11784, ⁷Department of Materials Science and Chemical Engineering, Stony Brook University, Stony Brook, NY 11794

The creation of polystyrene thin films via spin-coating has several industry applications, such as lens and adhesives-making, in which control over the thickness of the films is critical. Molecular weight and the concentration of polystyrene in the spin-coating solution are 2 factors that affect thickness [1,2]. In this study, we created a python program that is able to receive an input monodisperse molecular weight of polystyrene of any concentration and return an accurate estimation of spin-coat thickness. The program utilizes a machine learning model trained on a 3D-manifold that relates molecular weight, concentration, and thickness.

To determine the relationship between polystyrene thin film thickness and solution concentration, monodisperse polystyrene with molecular weights 30K, 50K, 123K, 200K, 311K, 650K, 1080K, and 2000K were each dissolved in toluene solvent at concentrations of 10 mg/mL, 15mg/mL, 20mg/mL, 25 mg/mL, and 30 mg/mL. After manually cleaving 1x1 cm silicon wafers and blow-cleaning them with extra dry compressed nitrogen, we spin-coated the polystyrene of the set molecular weights prepared at the set concentrations onto the silicon wafers. Through ellipsometry, we determined the angstrom thickness of the coated thin films. After taking the average of the six thickness readings we obtained of each molecular weight at each concentration, we plotted the data on a thickness vs concentration graph, determining a second degree polynomial relationship exists between thin film thickness and solution concentration after running a polynomial regression. The thickness data with 2nd-degree polynomial fits [Figure 1] and their corresponding equations [Figure 2], are shown.

This dataset was then used to generate a 3-Dimensional manifold [Figure 3] that relates molecular weight, concentration, and thickness and train a machine learning model that can predict the thickness of a spin-coated polystyrene thin film with any given molecular weight and concentration.

In the future, we will test the model's accuracy with actual results of spins with combinations of molecular weights and concentrations that were not used to generate the manifold. If the python-based program proves to be accurate, one will be able to determine the solution concentration needed to coat silicon wafer with a specific thickness with a certain monodisperse molecular weight of polystyrene. Separately, we also plan on investigating the effects of annealing on the thickness measurements of the thin films.

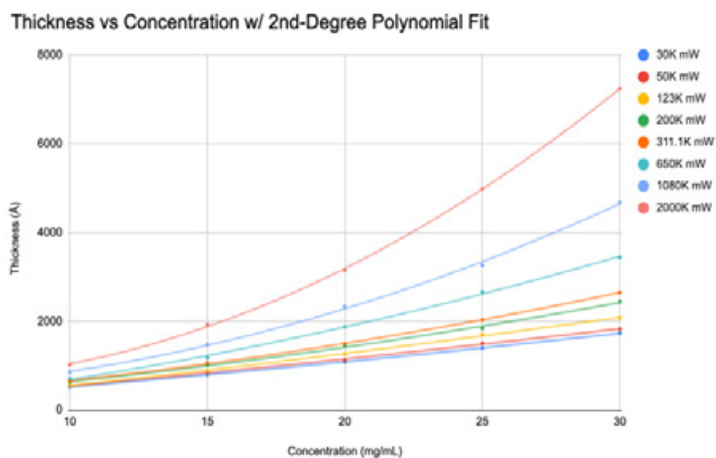


Figure 1: Lines of best fit for concentration vs thickness of monodisperse

$$\begin{aligned} \text{for mW } 30K &: 31.9 + 45.4x + 0.372x^2 \\ \text{for mW } 50K &: 11.7 + 50x + 0.355x^2 \\ \text{for mW } 123K &: -78.5 + 58.6x + 0.453x^2 \\ \text{for mW } 200K &: 99.5 + 42.4x + 1.17x^2 \\ \text{for mW } 311K &: 144 + 36.6x + 1.56x^2 \\ \text{for mW } 650K &: -71.1 + 55.5x + 2.08x^2 \\ \text{for mW } 1080K &: 421 - 2.65x + 4.79^2 \\ \text{for mW } 2000K &: 800 - 70.8x + 9.52^2 \end{aligned}$$

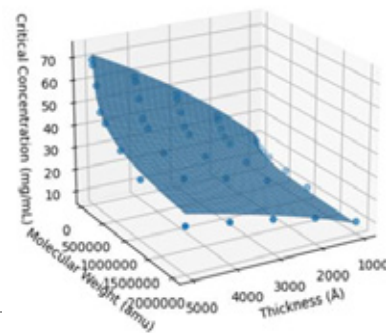


Figure 3: 3D manifold

[1] Sood, Sahil, et al. Polystyrene Laboratory Analysis: A Hands-On Experience for High School Students to Determine the Molecular Weight of Polystyrene Through Spin Casting. Journal of Chemical Education 2023 100 (2), 900-906

[2] Ton-That, C., et al. Thickness of Spin-Cast Polymer Thin Films Determined by Angle-Resolved XPS and AFM Tip-Scratch Methods. Langmuir 2000 16 (5), 2281-2284

Using Digital Image Speckle Correlation (DISC) to Identify Micro Emotions

Hyeonji (Tiffany) Ahn*, Elaina Heghes*, Jessica Kang*, Anusha Misra*, Shirley Xiong*, Elaine Zhang*, Jessica Hofflich, Shi Fu, Pawel Polak, Miriam Rafailovich

St. Mark's School, Southborough MA 01772, South Side High School, Rockville Centre NY 11570, Dana Hills High School, CA 92629, Ward Melville High School, NY 11733, Jericho Senior High School, Jericho, NY 11753, Singapore American School, Singapore 738547, Department of Materials Science and Chemical Engineering, Stony Brook University, Stony Brook NY 11794, Department of Applied Mathematics and Statistics, Stony Brook University, Stony Brook NY 11794

**Authors contributed equally*

Facial expressions are one of the most basic and natural forms of communication between humans.¹ Alongside general facial expressions, micro emotions are spontaneous changes in facial muscles that indicate hidden emotions. Micro emotions become apparent in response to specific emotion-inducing stimuli, such as pictures and videos. These fleeting expressions are low in intensity and are therefore significantly more difficult to identify than visible facial expressions and emotions.²

This study uses DISC to identify micro expressions by analyzing subcutaneous facial muscle displacement. The use of DISC is optimal when identifying micro emotions because it operates by dividing an image into grids that trace displacement. Vector maps and strain fields are then generated by tracking the micromovements of the pixels in each frame. These plots are subsequently used to assess shifts in the subject's emotions through patterns in their facial muscle movements. Then, the intensity of this movement is calculated and graphed by averaging the displacement of vectors in each frame, enabling a comparison with the original positional data to indicate different changes in emotion (Figure 2).

The stimuli in the form of pictures that induce micro emotions are categorized using a valence and arousal scale. Valence denotes the emotional value of an image, while arousal characterizes its level of stimulation. The analysis of the participant's faces and the stimuli shows that high-valence images tend to evoke positive emotions, translating to more pronounced movement in the cheeks and mouth region (Figure 1). When the subject was exposed to an image with positive valence and high arousal, large levels of displacement occurred in those areas. Figure 2 illustrates the magnitude of facial displacement in four quadrants of the face: the upper left, upper right, lower left, and lower right. As observed in Figure 2, visible spikes span approximately one second within these four quadrants. These peaks represent sudden, fleeting muscle

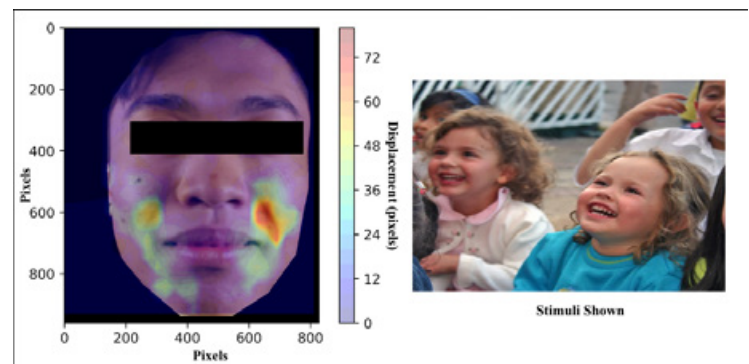


Figure 1. Facial movement of control subject to a high valence and arousal stimulus.

movements that correlate to micro emotions, which can be most effectively detected through the displacement captured by DISC technology. When the images with positive valences were shown (frames 0-50), large amounts of micro emotions were detected in all four quadrants due to the nature of happy emotions that positive valence photos elicit. The negative valence images induced significant amounts of micro emotions in the upper quadrants of the face, indicating movement in the forehead and eyebrow areas, commonly associated with sad emotions.

DISC has the potential to be used to analyze the efficacy of treatments of certain psychological disorders. MDD presents with non-verbal indicators such as the lack of or abundance of specific facial movements and reactions.³ Hence, facial expressions and movements identified by DISC can be used to diagnose and understand depression and to track the progression and regression of depressive symptoms.⁴ For example, esketamine, a more concentrated and potent variation of ketamine, is approved by the FDA to treat Major Depressive Disorder (MDD) that is resistant to other forms of treatment such as antidepressants. Digital Image Speckle Correlation (DISC) can be used to compare the facial responses of Treatment Resistant Depression (TRD) patients pre-esketamine use and post-esketamine use.

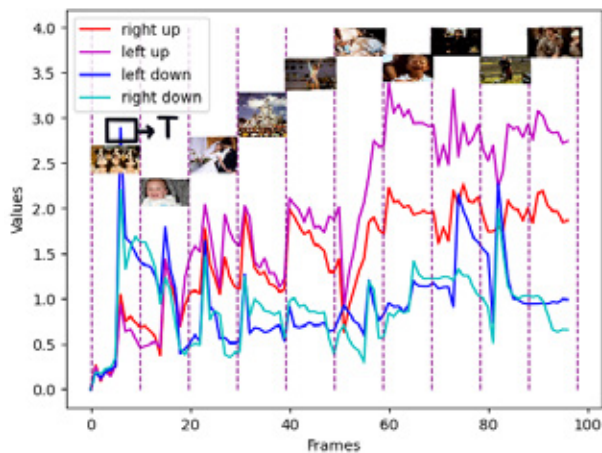


Figure 2. Total facial displacement in the quadrants of the face during test. Picture in between dotted lines were the pictures shown to the subject. Point T symbolizes drastic but quick muscle movement in the left cheek.

¹ Darwin, C. (1872). The expression of the emotions in man and animals (3rd ed.)

² X. Li *et al.*, "Towards Reading Hidden Emotions: A Comparative Study of Spontaneous Micro-Expression Spotting and Recognition Methods," in *IEEE Transactions on Affective Computing*, vol. 9, no. 4, pp. 563-577, 1 Oct.-Dec. 2018, doi: 10.1109/TAFFC.2017.2667642.

³ Stratou, G., Scherer, S., Gratch, J., & Morency, L. P. (2015). Automatic nonverbal behavior indicators of depression and PTSD: the effect of gender. *Journal on Multimodal User Interfaces*, 9(1), 17-29. <https://doi.org/10.1007/s12193-014-0161-4>

⁴ Ekman, P., Matsumoto, D., & Friesen, W. v. (n.d.). *Facial-Expression-In-Affective-Disorders*.

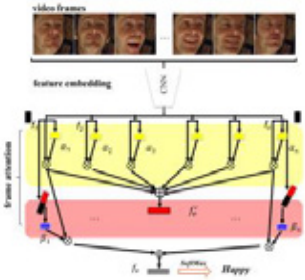
Enhanced Emotion Recognition via Deep Learning Integration with Digital Image Speckle Correlation

Juni Kim¹, Zhikang Dong², Shi Fu³, Miriam Rafailovich³, Pawel Polak^{2,4}

¹Stanford Online High School, Redwood City, CA 94063, ²Department of Applied Mathematics and Statistics, Stony Brook University, Stony Brook, NY 11794, ³Department of Materials Science and Chemical Engineering, Stony Brook University, Stony Brook, NY 11790

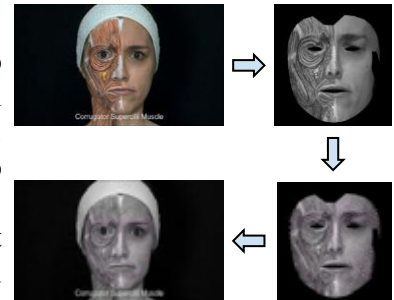
⁴Institute for Advanced Computational Science, , Stony Brook University, Stony Brook, NY 11794

Emotion detection based on micro-motions of facial muscles finds applications in a multitude of areas such as the diagnosis of muscle paralysis, person differentiation, reaction time evaluation, deep fake detection, and emotion measurement. This study leverages Digital Image Speckle Correlation (DISC), originally conceptualized for understanding mechanical stress in materials science, as a tool for detecting minuscule face muscle movements. DISC functions by comparing successive frames and producing a vector map that tracks pixel movements between frames.



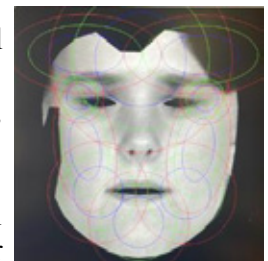
Nonetheless, employing DISC on facial videos for identifying subtle muscle movements often results in considerable measurement errors due to a low signal-to-noise ratio. This research synergizes DISC analysis with deep learning methodologies.

Initially, the Frame Attention Network (FAN)¹ is utilized to determine the likelihood of specific emotions within a video. We then implement the Facial Action Coding System (FACS), crafting a kernel smoothing operator that adjusts DISC measurements in proportion to the estimated FAN emotion probabilities within specific facial regions.



Our Face-GPS technique conducts the DISC measurement net of the head movement in the video. Canonical face images are generated through Google's open-source Mediapipe library and its face tracking and affine transformations. These standardized images facilitate DISC comparisons.

The DISC computations are executed through Optical Flow methods available in the OpenCV library. The subsequent vector field is superimposed on the canonical images and transformed back to the original video frames via inverse affine mapping.



The entire procedure generates a video analogous to the original, augmented with a vector map overlay that tracks the facial micromovements (Fig. 1). This refined vector map, showcasing the nuanced movements of face muscles, is integrated into an XGBoost classifier for the final emotion detection. The model is trained and tested using widely accepted datasets (such as CK++²) and our unique collection of videos that capture subtle and concealed emotional expressions.

¹ Meng, Debin, et al. "Frame Attention Networks for Facial Expression Recognition in Videos." 2019 IEEE International Conference on Image Processing (ICIP), IEEE, 2019, pp. 3866–70. DOI.org (Crossref), <https://doi.org/10.1109/ICIP.2019.8803603>.

² Lucey, P., Cohn, J. F., Kanade, T., Saragih, J., Ambadar, Z., & Matthews, I. (2010, June). The extended cohn-kanade dataset (ck+): A complete dataset for action unit and emotion-specified expression. In *2010 IEEE computer society conference on computer vision and pattern recognition-workshops* (pp. 94-101). IEEE.

Session 2: Clean Energy Generation

Chairs: Haoyan Fang, MD Farabi Rahman,
and Yifan Yin

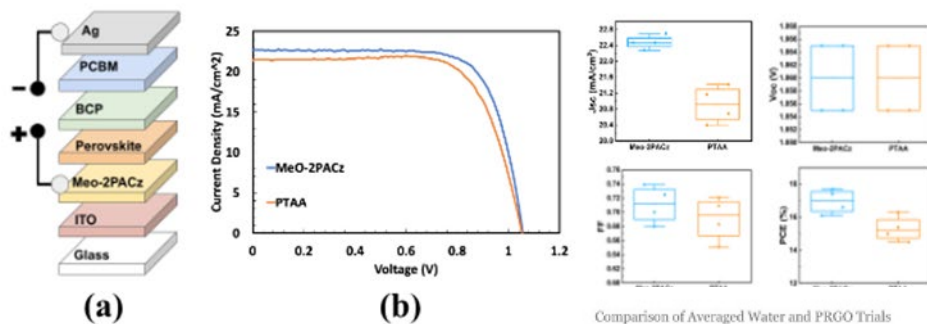
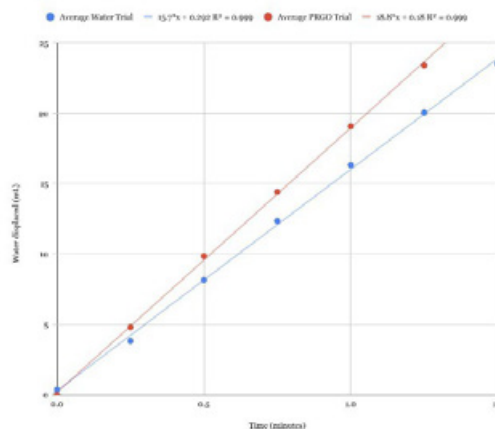


Figure 1: The structure of the perovskite solar cell (a), the Jv curve of the two champion devices (b), and photovoltaic performance parameters of the four samples (c).

Comparison of Averaged Water and PRGO Trials



Testing the Potential of Partially-Reduced Graphene Oxide as a Catalyst Enhancer

Sophia Bracco¹, Dominic Rosiello¹, Sergio Rosa¹, Sam Specht², Rebecca Isseroff³

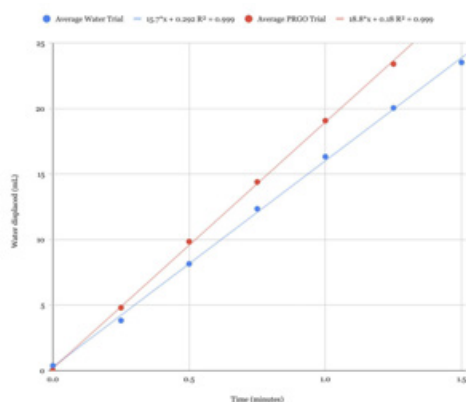
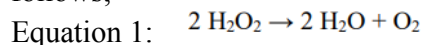
¹South Side High School, Rockville Center, NY ²The Stony Brook School, Stony Brook, NY

³Stony Brook University, Stony Brook, NY 11794

A catalyst increases the rate of a chemical reaction by producing an activated complex with a lower potential energy, thus lowering the activation energy of the reaction and speeding it up. It is often desirable to increase the reaction rate even more than the conventional catalyst's ability.

Partially-reduced graphene oxide (pRGO) is composed of graphene oxide (strongly oxidized graphite) partly reduced with sodium borohydride. It has previously been shown that pRGO added to a gelatin solution reduces the onset of gelation time using the enzyme microbial transglutaminase by nearly 50% while inducing a very large increase in viscosity by three orders of magnitude.¹ Would pRGO have an enhancing effect on another enzymatic reaction as well?

Yeasts are unicellular organisms possessing a variety of useful enzymes.² Among its arsenal is an enzyme that converts hydrogen peroxide to water and oxygen, as follows;



Would pRGO affect yeast activity of H_2O_2 decomposition?

To first qualitatively see if pRGO affects yeast, we incubated 0.012 grams yeast in tubes with 2 ml of water, 12 mM, 18 mM, and 21 mM pRGO and then added 15 ml 3% H_2O_2 containing a drop of Dawn detergent to see which tube produced the fastest rise in foam. Since the yeast in 18 mM pRGO rose the fastest, we chose this degree of reduction for subsequent experiments. We then found that an 18 mM pRGO dilution of 1:2 produced the fastest rate of O_2 bubble production. To quantify the reaction rate, we measured its rate by water displacement in an inverted graduated cylinder

filled with water. We reacted 0.012 g of yeast incubated with 2 mL of PRGO and yeast in 2 mL water and then combined each with 12 mL of hydrogen peroxide. We conducted four trials with yeast in water and four trials with yeast in 18 mM pRGO. The average rate of oxygen gas production in the water-yeast solutions was 15.7 mL/min whereas for the 18 mM PRGO-yeast solutions was 18.8 mL/min. The t-test value is 0.0156, which is less than 0.05, indicating statistical significance. In the future, we will analyze the GO and PRGO solutions using Raman Spectroscopy in order to determine the degrees of reduction. We will then test the effects of PRGO on the cross-linking of fibrinogen by thrombin, which are blood clotting agents.

¹ Isseroff, R., Reyes, J., Reddy, R. *et al.* The Effects of Graphene Oxide and Partially Reduced Graphene Oxide on the Enzymatic Activity of Microbial Transglutaminase in Gelatin. *MRS Advances* 4, 879–887 (2019). <https://doi.org/10.1557/adv.2019.89>

² https://folk.ntnu.no/preisig/HAP_Specials/Felles_lab/Experiments/RE5_yeast_fermentation.pdf

Exploring Self-Assembled Hole Transport Materials in p-i-n Perovskite Solar Cells

Hongyi Huang¹, Minsik Shin², Dongmin Yoon³, Christian Apostol⁴, Yifan Yin⁴, Miriam Rafailovich⁴

¹Shenzhen Middle School, Shenzhen, China 518021, ²Seoul International School, Seongnam, South Korea 13113, ³North London Collegiate School Jeju, Seogwiposi, South Korea, 63644, ⁴Department of Materials Science & Chemical Engineering, Stony Brook University, Stony Brook, NY 11794

Renewable energy plays a crucial role in combating climate change, and one of the primary focuses is improving the efficiency and production of solar cells. Over the past decade, perovskite solar cells (PSCs) have garnered significant attention due to the extraordinary evolution of the power conversion efficiency (PCE): perovskites are a class of materials with unique crystal structures, represented by the chemical formula ABX_3 ¹. Here, A denotes monovalent organic cations like methylamine (MA⁺), formamide (FA⁺), or cesium, while B refers to metal cations such as lead and tin. Finally, X represents halide anions. The inverted structure PSCs, also known as p-i-n PSCs offer several advantages, including lower production costs and enhanced stability compared to the conventional n-i-p PSCs. However, the inverted PSCs face the challenge of lower device efficiencies². In this study, we focus on two distinct materials for the hole transport layer (HTL): PTAA and Meo-2PACz. Our primary goals involve investigating the fabrication process to create an optimal substrate for subsequent perovskite layer deposition and evaluating the efficiency of MeO-2PACz as a hole transport material in inverted p-i-n perovskite solar cells. By exploring these aspects, we aim to contribute to the ongoing efforts to enhance the performance of PSCs.

Fabricating the solar cell, the HTL was first deposited onto the ITO glass through spin-casting. Two solutions were used: 1 mM Meo-2PACz in ethanol and 2 mg/ml PTAA in chlorobenzene. The spin-casting was done at 4000 rpm for 30 s, followed by annealing at 100°C for 10 minutes. Next, a 1.2M MAPbI₃ precursor solution in a mixed solvent of DMF/DMSO (v:v=9:1) was spin-casted on the glass at 4000 rpm for 30 s. 150 μ L of toluene was dripped onto the surface 10 s after the beginning of spinning, the as-casted film was annealed at 100°C for 10 min. The subsequent steps involved spin coating a 20 mg/ml solution of PCBM at 1500 rpm for 30 s, followed by spin coating a 0.5 mg/ml BCP at 4000 rpm for 30 s. Finally, Ag electrodes (100 nm) were deposited using physical vapor deposition (PVD).

In terms of measurements, the surface roughness of Meo-2PACz and PTAA coated substrates was investigated using Atomic Force Microscopy (AFM). Both films exhibited relatively small surface roughness. Fourier Transform Infrared Spectroscopy showed peak shifts of the phosphate functional group due to its reaction with the glass substrate. Contact Angle measurements demonstrated that Meo-2PACz exhibits higher hydrophilicity, which enhances nucleation and crystal growth. X-ray Diffraction (XRD) analysis revealed that both perovskites coated onto Meo-2PACz or PTAA substrate show a similar crystallinity. Scanning Electron Microscopy (SEM) revealed that the perovskite prepared from the Meo-2PACz-coated substrate had a larger average grain size. Furthermore, PV Performance testing confirmed Meo-2PACz's superiority as a hole transport material, achieving a higher PCE of 17.7% compared to PTAA's 16.3% PCE in the fabricated inverted p-i-n device.

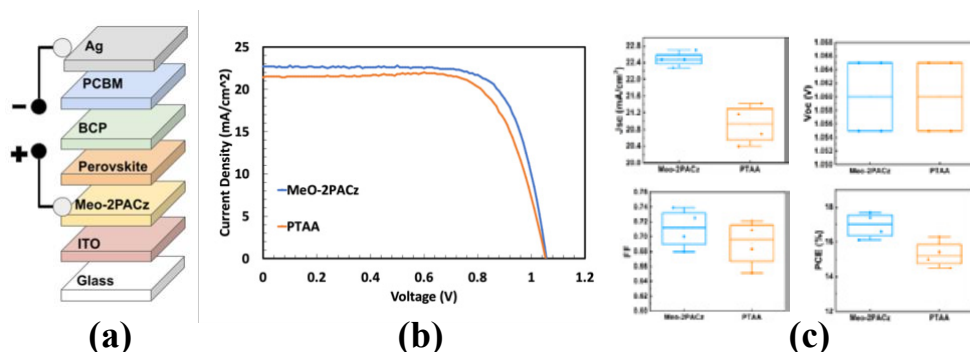


Figure 1: The structure of the perovskite solar cell (a), the Jv curve of the two champion devices (b), and photovoltaic performance parameters of the four samples (c).

¹"Perovskite Solar Cell - Clean Energy Institute". *Clean Energy Institute*, 2023, <https://www.cei.washington.edu/education/science-of-solar/perovskite-solar-cell/> Accessed 1 Aug 2023.

²Zhang, D., Zhang, H., Guo, H., Ye, F., Liu, S., Wu, Y., Stable α -FAPbI₃ in Inverted Perovskite Solar Cells with Efficiency Exceeding 22% via a Self-Passivation Strategy. *Adv. Funct. Mater.* 2022, 32, 2200174. <https://doi.org/10.1002/adfm.202200174>. Accessed 2 Aug 2023.

Enhancement of Anion Exchange Membrane Fuel Cells by Functionalizing Microcellulose with Partially Reduced Graphene Oxide

Kenneth Chang^{1*}, Richard Chen^{2*}, Raymond Wang^{3*}, Haoyan Fang⁴, Rebecca Isseroff⁴, Miriam Rafailovich⁴

¹Great Neck South High School, Great Neck, NY 11020, ²Andover High School, Andover, MA 01810, ³Casa Grande High School, Petaluma, CA 94954 ⁴Department of Materials Science and Chemical Engineering, Stony Brook University, Stony Brook, NY 11794

*These authors contributed equally to this work.

As carbon emissions from fossil fuels increasingly contribute to climate change, hydrogen fuel cells have emerged as a carbon-free, green source of energy, operating without combustion and producing water as waste¹. Anion exchange membrane fuel cells (AEMFCs) are a form of hydrogen fuel cell that transports OH⁻ ions across an anion exchange membrane (AEM). This gives them several advantages over other fuel cells, such as lower cost and less corrosion². The composition and properties of the AEM heavily determine the effectiveness of the fuel cell, with polymer membranes leading the market due to their high performance. However, these polymers come at prohibitively expensive price points, providing a large entry barrier to widespread commercialization. Therefore, we propose the use of microcellulose as a low-cost alternative AEM material. This study aims to investigate the effectiveness of microcellulose filters impregnated with potassium hydroxide (KOH) and Sustainion[®] ionomer and functionalized with partially reduced graphene oxide (prGO) as an AEM.

Microcellulose filters sourced from Ahlstrom-Munksjö were submerged in 200 mL of 1 M potassium hydroxide solution overnight and air dried. Thirteen drops of Sustainion[®] XA-9 ionomer (Dioxide Materials) dissolved in ethanol were pipetted onto the surface of the KOH-impregnated cellulose filters. This solution was allowed to diffuse and air dry, creating KOH and Sustainion[®] (KOH-Sus) impregnated cellulose membranes. Graphene oxide (GO) prepared by Hummer's method was dissolved in distilled water to create three 10 mL solutions of 1 mg/mL GO. The GO solutions were then partially reduced to different degrees using sodium borohydride (NaBH₄), creating prGO solutions of 10 mM, 12 mM, and 15 mM reduction. Three KOH-Sus cellulose membranes were airbrushed with 24 drops of prGO solution, with one membrane for each reduction degree. These 3 membranes, along with a control membrane with no prGO coating, were tested in the fuel cell test station between two gas diffusion electrodes with a loading of 0.76 mg cm⁻² Pt/C catalyst ink.

Figure 1a demonstrates that surface coating of the KOH-Sus membranes with 12 mM prGO significantly increased the maximum power density of the AEMFC, with the maximum power density of 17.7 mW cm⁻² exhibiting a 26.4% increase when compared to the control. Similarly, as shown in Figure 1b, the 12 mM prGO treatment exhibited a 6.5% increase in maximum voltage compared to the control, with the 15 mM prGO treatment exhibiting the largest increase in maximum voltage at 15.3%. However, the 10 mM prGO and 15 mM prGO treatments were unable to support greater current densities, indicating reduction beyond 12 mM may reduce stability. Our future work focuses on using micro computed tomography or gas adsorption testing to characterize these membranes and their porosity, as well as further investigate the effect reduction degree has on performance.

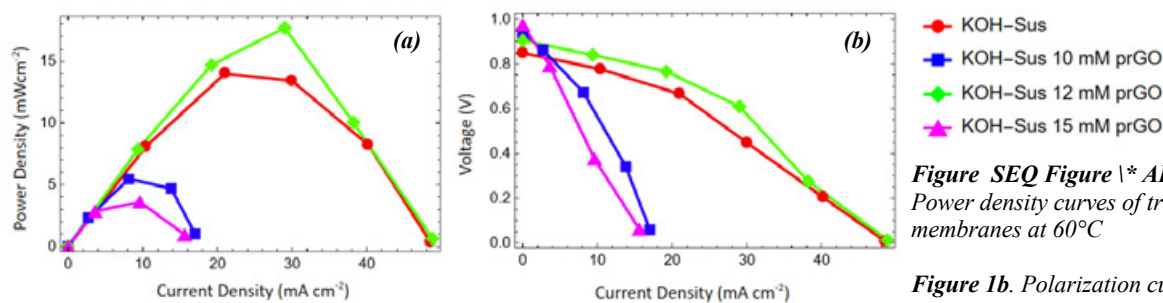


Figure 1a. Power density curves of treated membranes at 60°C

Figure 1b. Polarization curves of treated membranes at 60°C

¹ Das, Gautam, Ji-Hyeok Choi, Phan Khanh Thinh Nguyen, Dong-Joo Kim, and Young Soo Yoon. 2022. "Anion Exchange Membranes for Fuel Cell Application: A Review." *Polymers* 14 (6): 1197. <https://doi.org/10.3390/polym14061197>.

² Firouzjaie, Horie Adabi, and William E. Mustain. 2019. "Catalytic Advantages, Challenges, and Priorities in Alkaline Membrane Fuel Cells." *ACS Catalysis* 10 (1): 225–34. <https://doi.org/10.1021/acscatal.9b03892>.

Study of Silver Nanoparticle Deposition on Proton Exchange Membrane Fuel Cells

Prisha Jain¹, Anna Heimowitz², Jonathan Sacolick³, Haichuan Wang⁴, Md. Farabi Rahman⁵, Haoyan Fang⁵, Miriam Rafailovich⁵

¹Irvington High School, Fremont, CA, 94538, ²Stella K. Abraham High School for Girls, Hewlett, NY, 11557, ³Hebrew Academy of Five Towns and Rockaway High School, Cedarhurst, NY, 11559, ⁴Shanghai Jianping High School, Shanghai, China, 200135, ⁵Department of Materials Science and Chemical Engineering, Stony Brook University, Stony Brook, NY 11794

Hydrogen fuel cells are an innovative technology capable of producing electricity from hydrogen gas and air. The fuel cell's electrolytic reaction emits only water vapor, making hydrogen fuel cells a more sustainable energy technology¹. Proton exchange membrane fuel cells (PEMFCs) are known for their low operating temperature and high power density². Existing PEMFCs utilize a platinum (Pt) catalyst for better efficiency, but the catalyst's high cost has prevented the widespread adoption of PEMFCs. The amount of Pt catalyst necessary can be reduced by adding non-Pt group catalysts to the fuel cell.

This study aims to research the impact of silver nanoparticles on the power density of PEMFC. Silver nanoparticles, synthesized using the Brust-Schiffrin method, were capped with octanethiol or dodecanethiol. The thiol caps prevented nanoparticle interactions, reducing agglomeration, one of the main challenges with silver nanoparticles³. The synthesized particles were examined employing Transmission Electron Microscopy (TEM); they were spherical nanoparticles with a diameter of about 4 nm for both octanethiol-capped and dodecanethiol-capped nanoparticles. Isothermal data was collected using the Langmuir-Blodgett Trough (LBT) to determine the surface pressure required to develop a monolayer on a Nafion-117 membrane for both octanethiol and dodecanethiol. The silver nanoparticles were deposited at surface pressures of 2, 5, and 10 mN/m. Then, the 6 membranes were characterized in the hydrogen fuel cell test station, and the PEMFC performance was recorded for each one.

Data from the PEMFC demonstrated no significant power density enhancement with octanethiol-capped silver nanoparticles at surface pressures of 2 and 5 mN/m; however, at 10 mN/m, a 33% increase in power density was observed (Figure 1). For dodecanethiol-capped silver particles a similar trend was observed. There was no significant power density increase at surface pressures of 2 and 5 mN/m but there was about a 33% increase in power density at a pressure of 10 mN/m (Figure 2).

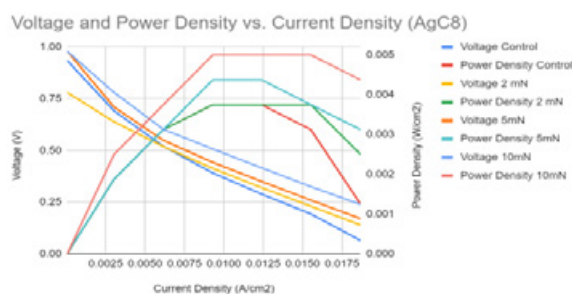


Figure 1: Voltage and Power Density vs. Current Density for different surface pressures of AgC₈ deposition

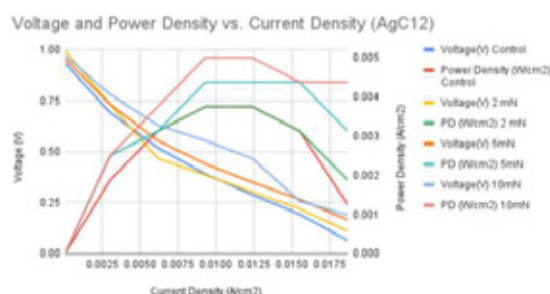


Figure 2: Voltage and Power Density vs. Current Density for different surface pressures of AgC₁₂ deposition

¹ P.P. Edwards, V.L. Kuznetsov, W.I.F. David, N.P. Brandon, Hydrogen and fuel cells: Towards a sustainable energy future, Energy Policy, Volume 36, Issue 12, 2008, Pages 4356-4362, doi.org/10.1016/j.enpol.2008.09.036.

² Ryan O'Fayre et al. Fuel Cell Fundamentals. 3rd ed., Wiley, 2016

³ Connie Manz, Lee Williams, Ray Mohseni, Eugene Zlotnikov, Aleksey Vasiliev, Dispersibility of organically coated silver nanoparticles in organic media, Colloids and Surfaces A: Physicochemical and Engineering Aspects, Volume 385, Issues 1-3, 2011, Pages 201-205, doi.org/10.1016/j.colsurfa.2011.06.009.

Investigating the Effects of ZnO Deposition on Alkaline Anion Exchange Membrane Fuel Cells

Kriste An^{1*}, Samuel Chen^{2*}, Rohan Suri^{3*}, Haoyan Fang⁴, Farabi Rahman⁴, Miriam Rafailovich⁴

¹Harvard-Westlake School, Studio City, CA, ²Ed W. Clark High School, Las Vegas, NV, ³Ladue Horton Watkins High School, St. Louis, MO, ⁴Department of Materials Science and Chemical Engineering, Stony Brook University, Stony Brook, NY

*All authors contributed equally to this work

In response to a global challenge to find a clean and sustainable power source, scientists have turned their attention to alkaline anion exchange membrane fuel cells (AEMFCs). These fuel cells offer a promising alternative to proton exchange membrane fuel cells (PEMFCs) given their abilities to function in alkaline environments and potential for low-cost production. Though significant progress has been made in the development of AEMFCs, several obstacles impede their application. Poor water management in AEMFCs, for example, leads to flooding at the anode and dries up the cathode, deteriorating the cells' performance [1]. Previous research has also shown that platinum migration and precipitation degrade the performance of AEMFCs [2]. In response, scientists have proposed depositing a thin film of zinc oxide (ZnO) between the AEM and the catalyst layer to mitigate platinum migration and improve water management. This project investigated the effects of ZnO deposition on the performance of AEMFCs.

Preparing the membranes for the fuel cell involved a two-step process. First, we used the atomic layer deposition (ALD) method, a high-precision deposition technique for growing thin films, to deposit 5, 10, 15, and 30 layers of ZnO onto the fuel cells' alkaline exchange membranes (Sustainion-grade T). XRD measurements were taken that demonstrate the deposited ZnO's amorphous nature, as shown in Figure 2. Then, an ink containing ionomer, distilled water, isopropanol, and PtRu/C (for the anode) or Pt/C (for the cathode) powder was sprayed onto pieces of carbon paper at a loading amount of 0.5 mg/cm². The voltage and power output of the fuel cells were tested at 60 °C with pure H₂ gas supplied to the anode and pure O₂ supplied to the cathode until the voltage dropped below 0.1 V.

As shown in Figure 1, the control cell recorded a maximum power density of 0.334 W/cm². The fuel cells with 5 and 10 layers recorded maximum power densities of 0.382 W/cm² (a 14.4 percent increase) and 0.430 W/cm² (a 28.7 percent increase), proving more powerful than the control cell. This can be because the ZnO deposition prevents Pt degradation and helps water flow throughout the cell, preventing flooding at the anode. The ALD method that we used to deposit ZnO, moreover, can increase the surface area of the reaction, enhancing the fuel cells' performance. Depositing increasing amounts of ZnO proved less effective, however. The fuel cells with 15 and 30 layers of ZnO recorded maximum power densities of 0.312 W/cm² (a 6.59 percent decrease) and 0.274 W/cm² (a 18.0 percent decrease), proving less efficient than the control cell. This can be because too much ZnO on the fuel cell inhibits water movement, stifling the fuel cell's performance. It can also be because excess ZnO hinders the reaction between the gas and the catalyst, causing the performance of the fuel cells to deteriorate. This shows that among the amounts tested, the fuel cell with 10 layers of ZnO proved the most effective. Future research should include further spectroscopic and microscopic characterization of the membrane and electrodes before and after the performance tests to gain a deeper understanding of our results.

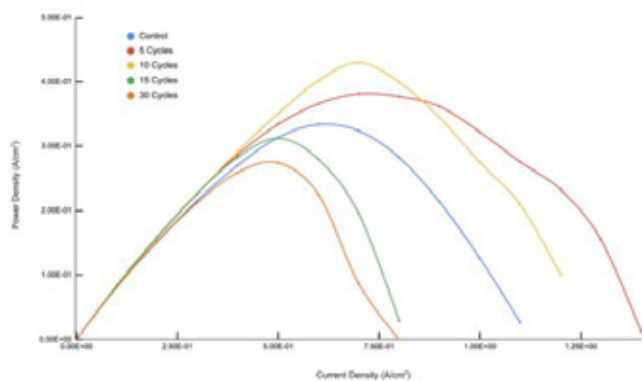


Figure 1: Graph of power density vs. current density for each of the fuel cells tested

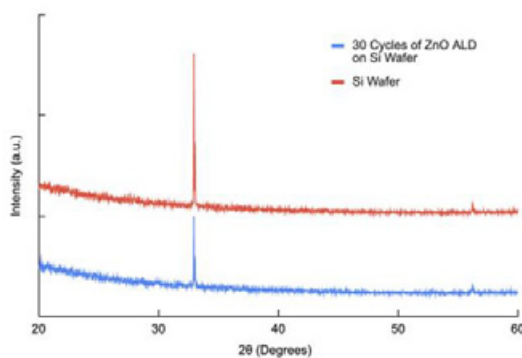


Figure 2: XRD spectra of a Si wafer and a Si wafer with 30 layers of ZnO

[1] Das, Gautam, et. al. "Anion Exchange Membranes for Fuel Cell Application: A Review." *Polymers* (Basel). 2022

[2] Raut, Aniket, et. al. "Migration and Precipitation of Platinum in Anion-Exchange Membrane Fuel Cells." *Angewandte Chemie*, 2023.

Session 3: Ethical Considerations in Science & Engineering

Advisor: Prof. Brooke Ellison



An authentic life: on the ethics of providing gender-affirming care for youth through the framework of ethical care

Boheng Cao¹, Jude Ouerfelli², Adam Zaidi³

¹North Hollywood High School, CA 91601, ²Fort Lee High School, NJ 07024, ³San Francisco University High School, CA 94115

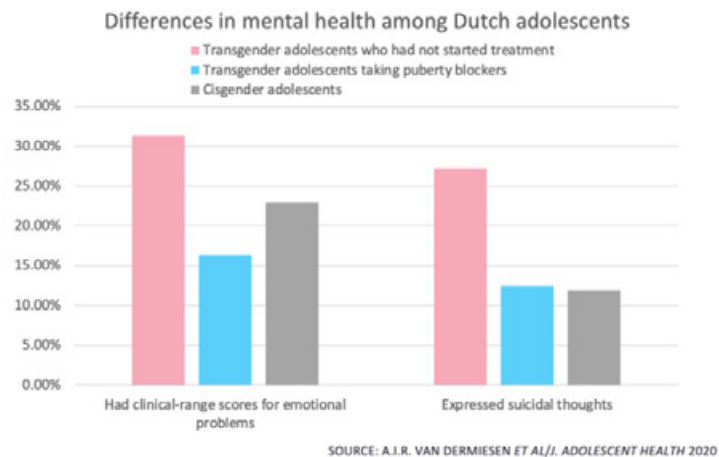
*All authors contributed equally to this work

With the increasing acceptance of gender nonconformity in mainstream Western societies, a growing number, particularly among youth, are embracing an identity different from their assigned gender at birth. Gender-affirming care (GAC) has emerged as a supportive form of healthcare for gender non-conforming people to align their physical characteristics with internal perceptions of gender identity, whether conventionally binary (female or male) or otherwise.

While the public eye has focused on the more overtly medical components of GAC, care for minors often prioritizes mental health and social services instead. Surgery to correct sex characteristics is usually unavailable for adolescents, with most current clinical standards recommending its postponement until early adulthood. More common are puberty blockers to reversibly delay the onset of puberty until a more comprehensive hormonal phenotypic transition with estrogen or testosterone can be pursued. While the physiological effects of this treatment are not well-understood, GAC has been widely recognized as improving long-term mental health prognoses and alleviating gender dysphoria in many gender-nonconforming patients.¹

Controversy has recently arisen, though, over the ability of minors to consent to such treatments, the best treatment practices, disparities in treatment accessibility among different demographics, and looming risks of regret or detransition. Furthermore, treatment may be complicated by comorbidities in gender-nonconforming patients, including a higher prevalence of anxiety, mood disorders, suicidal ideation, and autism spectrum disorder. Yet, the importance of GAC cannot be understated, as these services help individuals feel more whole in a community that faces mental health and substance abuse at a much higher rate than the general population due to lack of family acceptance, rejection in schools, and abuse from peers. In this paper, we explore such questions through the framework of ethical care as it pertains to providing treatment. We ask questions regarding how such care is provided under the guiding principles of autonomy, beneficence, justice, and non-maleficence, all while considering three key case studies.

We conclude that medical practitioners must undertake a multidisciplinary approach in providing care and meeting the unique needs of gender-nonconforming youth.² Patients should be provided with thorough informed consent, along with mental healthcare in addition to their physical treatment. As legal battles rage throughout the West regarding the provision of such care, we urge citizens to take a step back and consider this issue from a nuanced ethical standpoint to provide the best clinical outcomes for youths seeking treatment rather than barring access to this care and contributing further to the already rampant international mental health epidemic.



¹ Lee, J. Y., & Rosenthal, S. M. (2022). Gender-affirming care of transgender and gender-diverse youth: Current concepts. *Annual Review of Medicine*, 74(1), 107–116. <https://doi.org/10.1146/annurev-med-043021-032007>

² Chen, D., Hidalgo, M. A., Leibowitz, S., Leininger, J., Simons, L., Finlayson, C., & Garofalo, R. (2016). Multidisciplinary care for gender-diverse youth: A narrative review and unique model of gender-affirming care. *Transgender Health*, 1(1), 117-123. <https://doi.org/10.1089/trgh.2016.0009>

Examining the effects of implicit bias in healthcare and potential solutions

Ethan Lai¹, Michael Wang², Elaine Zhang³

¹Phillips Academy, Andover, MA 01810 ²Mounds View High School, Arden Hills, MN 55112 ³Jericho Senior High School, Jericho, NY 11753

Upon entering a hospital or doctor's office, patients expect adequate care. Similarly, it is a doctor's responsibility to treat all patients with the same standard of care and thoughtfulness. Unfortunately, implicit bias has been proven to influence the judgment of doctors and medical professionals when diagnosing, treating, and interacting with patients. Implicit biases involve associations outside conscious awareness that lead to a negative evaluation of a person based on irrelevant characteristics such as race or gender.¹

In 2016, Kelly M. Hoffman, a UVA psychology Ph.D. candidate, conducted two studies questioning medical and non-medical professionals about medical scenarios and the validity of biological differences in races. Both studies concluded that white adults endorse beliefs about biological differences between black and white individuals, the majority of which are fictitious. Furthermore, participants high in false biological beliefs rated the pain of black individuals lower. This idea is reinforced as the study concludes that participants who believed more false ideals about biological differences between blacks and whites showed a racial bias in the accuracy of their treatment recommendations.²

Some have argued that individuals are not consciously aware of their biases and cannot control them; this would provide little ground for individuals to be held responsible for their implicit biases.³ However, recent empirical evidence has shown this to be untrue. A 2015 study showed that implicitly biased participants in the study have some awareness of their own biases.⁴ Studies have also shown that implicitly biased participants can "control themselves" in social situations but are cognitively fatigued afterward.⁵ The fact that it is merely difficult, not impossible, to control implicit bias is enough to establish moral responsibility. Individuals are responsible for controlling their implicit biases and preventing the associated harms.

The increased attention given to implicit bias and its effects has led to the development and implementation of many approaches to reduce the impacts of implicit bias.⁶ However, evidence suggests that current strategies to reduce implicit bias produce insignificant results and, in some cases may even cause the opposite of the intended effect.⁷ Extensive research has been done to find an evidence-based solution to the inefficiencies of traditional training methods elsewhere.⁸ One example is Professor Patricia Devine's prejudice habit-breaking intervention, which approaches bias as a "habit" and tries to reduce implicit bias through breaking habitual tendencies associated with race, gender, and other demographics. This study reveals important results, showing that scores on the Implicit Association Test (IAT) before and after the training decreased significantly compared to the control group (Figure 1). This provides promising methods to reduce implicit bias in healthcare. In this paper, we will examine the impact of implicit bias in modern-day healthcare and analyze the efficacy of various studies in reducing the impacts of bias in healthcare.

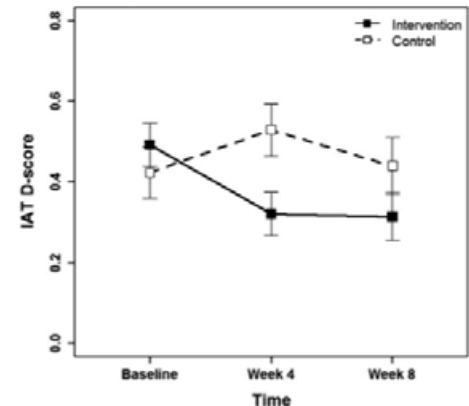


Figure 1. IAT D-scores for intervention and control groups. Higher numbers indicate higher levels of implicit bias. (Devine, Patricia G et al. "Long-term reduction in implicit race bias: A prejudice habit-breaking intervention." *Journal of Experimental Social Psychology* vol. 48,6 (2012): 1267-1278. doi:10.1016/j.jesp.2012.06.003)

¹ FitzGerald C, Hurst S. Implicit bias in healthcare professionals: a systematic review. *BMC Med Ethics*. 2017 Mar 1;18(1):19. doi: 10.1186/s12910-017-0179-8. PMID: 28249596; PMCID: PMC5333436.

² Hoffman, Kelly M et al. "Racial bias in pain assessment and treatment recommendations, and false beliefs about biological differences between blacks and whites." *Proceedings of the National Academy of Sciences of the United States of America* vol. 113,16 (2016): 4296-301. doi:10.1073/pnas.1516047113

³ Lawrence, Charles R. "The Id, the Ego, and Equal Protection: Reckoning with Unconscious Racism." *Stanford Law Review*, vol. 39, no. 2, 1987, pp. 317-88. JSTOR, <https://doi.org/10.2307/1228797>. Accessed 5 Aug. 2023.

⁴ Cooley, E., Payne, B. K., Loersch, C. and Lei, R. (2015). "Who Owns Implicit Attitudes? Testing a Metacognitive Perspective," *Personal and Social Psychology Bulletin* 41(1), pp. 103-115.

⁵ Richeson, J. A. and Shelton, J. N. (2007). "Negotiating Interracial Interactions: Costs, Consequences and Possibilities," *Current Directions in Psychological Science* 16(6), pp. 316-320; Gonsalkorale, K., von Hippel, W., Sherman, J. W. and Klauer, K. C. (2009). "Bias and Regulation of Bias in Intergroup Interactions: Implicit Attitudes toward Muslims and Interaction Quality," *Journal of Experimental Social Psychology* 45(1), pp. 161-166.

⁶ Devine, Patricia G et al. "Long-term reduction in implicit race bias: A prejudice habit-breaking intervention." *Journal of Experimental Social Psychology* vol. 48,6 (2012): 1267-1278. doi:10.1016/j.jesp.2012.06.003

⁷ Coffman, Katherine and Gino, Francesca. "Unconscious Bias Training That Works." *Harvard Business Review*, 30 Aug. 2021, hbr.org/2021/09/unconscious-bias-training-that-works. Accessed 5 Aug. 2023.

⁸ Devine, Patricia G et al. "A Gender Bias Habit-Breaking Intervention Led to Increased Hiring of Female Faculty in STEM Departments." *Journal of Experimental Social Psychology* vol. 73 (2017): 211-215. doi:10.1016/j.jesp.2017.07.002

Ethics of Germline Genome Editing (GGE) for Therapeutics

Sai Pranav Kota^{1*}, Rohan Suri^{2*}

Cedar Falls High School, Cedar Falls, IA¹, Ladue Horton Watkins High School, St. Louis, MO²

*All authors contributed equally to this work

The first intentional, targeted gene edits were accomplished in the 1970s, performed on yeast and mice, more than 100 years after the discovery of DNA. The scientists involved (Kirk R. Thomas, Kim R. Folger, and Mario R. Capecchi) corrected a defective gene within a mammalian cell by injecting copies of the same gene carrying a different mutation into the nucleus¹. The process used by these scientists, although rudimentary, laid the groundwork for an entire field of study in the years to come.

Forty years later, scientists discovered a new, revolutionary way to edit the DNA of eukaryotic cells: CRISPR/Cas 9. As seen in Figure 1, CRISPR utilizes restriction enzymes, which are enzymes normally found in prokaryotic cells, as a tool to cut DNA when needed. The use of this method markedly decreased the cost of gene editing, rendering it a far more viable technique for use as a therapeutic.

Germline genome editing (GGE), has and will continue to be a controversial but revolutionary practice. The concept of altering an embryo's DNA is a radical one, and one that many classify as unethical. One of the main arguments supporting this perspective relates to informed consent and the future child's autonomy; it states that manipulating a child's genome prior to their birth is committing an action that is undoable, essentially robbing the child of the right to decide their own future. However, the autonomy argument actually neglects the fact that parents already make critical decisions regarding their child's future, some of which include education, vaccination, and medical treatment. Another important consideration for GGE use is the risk of off-target mutations: errors in the gene editing process which would increase the risk of an already critical procedure. Although the off-target mutation argument is valid, one cannot conclusively prove unethicity, as all medical procedures require the patient to assume some amount of risk during treatment. If assumption of risk was deemed unethical, progress would become nearly impossible, with new treatments being shot down before research could even be conducted. There are also significant justifications to be considered when determining the ethicality of GGE: the possibility of curing monogenic diseases (e.g. cystic fibrosis and duchenne muscular dystrophy) and the chance for parents dealing with infertility to have children genetically related to them, which current therapeutic options do not provide. Moreover, the possible benefits of GGE extend even further than these two possible practices, and as a result, it would be a fatal error to ignore GGE's potential.

As GGE continues to develop in the future, polygenic modifications will eventually become a reality, giving scientists the ability to adjust an embryo's appearance, IQ, or physical strength. These changes will bring into light the debate between enhancement and therapeutics, and what should be permissible when using GGE. Some say enhancement is inherently unethical, and only therapeutics should be allowed, yet without defining the line between either one, it is impossible to justify any sort of treatment in the first place. Nonetheless, this is not a present concern, as GGE has not yet been developed to the point of polygenic modification. Because of this, it is possible to conclusively contradict the current governmental ruling that places a moratorium on the research and therapeutic use of GGE by justifying a set of cases that are currently achievable where the use of GGE is ethically permissible and necessary.

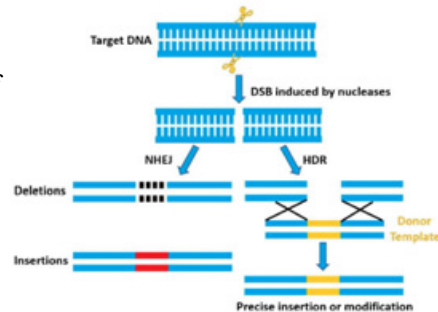


Figure 1. Mechanisms of genome editing.

[1] Carroll D. (2017). Genome Editing: Past, Present, and Future. The Yale journal of biology and medicine, 90(4), 653–659

[2] Xu Y, Li Z. CRISPR-Cas systems: Overview, innovations and applications in human disease research and gene therapy. Comput Struct Biotechnol J. 2020 Sep 8;18:2401-2415. doi: 10.1016/j.csbj.2020.08.031. PMID: 33005303; PMCID: PMC7508700.

The Use of Prenatal Screening to Select Against Disorders and Disability

Dvita Bhattacharya¹, Aditi Kiran²

¹ Kent Place School, NJ, ² BASIS Independent Fremont, CA

*authors contributed equally

Since its birth in the 1950s, prenatal testing has revolutionized the field of obstetrics and gynecology by enabling parents to select against genetic abnormalities and birth defects in their offspring. Over the last 70 years, these technologies have become a standard of obstetric care, with 75% of fertility clinics in the United States offering Prenatal Genetic Diagnosis (PGD) to parents undergoing IVF treatment¹. PGD, a form of prenatal testing, is used during in vitro fertilization to scan candidate embryos for genetic disorders, allowing parents to select against embryos with disorders. Other tests, such as amniocentesis, chorionic villus sampling and ultrasound, are also routinely used to recognize disorders and disabilities during gestation, after which parents may choose to abort affected fetuses. As these technologies progress, they raise important ethical questions about the value of life, disability rights, and human intervention in genetics.

Proponents of selecting against genetic disorders and disabilities argue that eliminating these conditions in early embryos minimizes suffering and provides children with a better quality of life. Others, however, claim that such technologies could lead to discrimination against disorders/disability and a subsequent elimination of these traits such as Down Syndrome, as illustrated in [Figure 1](#). Currently, selection against disorders and disability is widely accepted in the medical community², with some literature even suggesting that it is a parent's moral *obligation* to select against children with disorders or disabilities. This paper evaluates the ethical implications of such claims through the ethical principles of beneficence, paternalism, and utilitarianism.

Upon considering the aforementioned principles and various case studies, we concluded that the ethicality of selection against disorders and disability must take into account various factors. Evaluating severity, prognosis, and available treatment is necessary when deciding whether to select against a disability/disorder. Ultimately, the goal of prenatal testing should be to provide a good quality of life for each child, and we found that several disorders, such as Down Syndrome, *can* allow affected individuals to lead healthy, fulfilling lives. Therefore, we propose that regulation of PGD should be a collaborative case-by-case process involving guidelines from healthcare professionals and familial bioethics consultation services, which are provided in the vast majority of hospitals³. Further ethical considerations include the financial capacity of parents and access to sufficient health care resources, both of which should also be considered on a case-by-case basis.

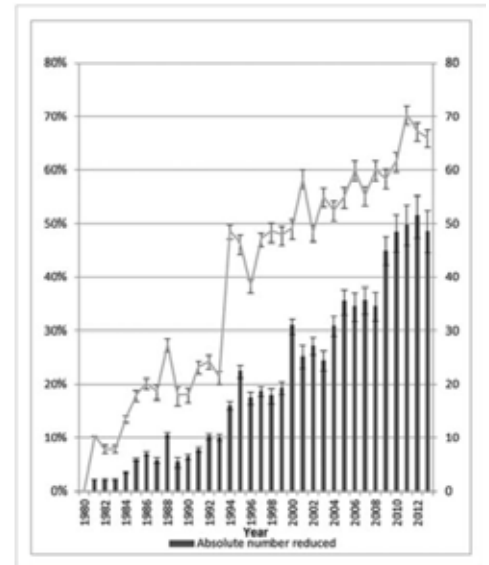


Fig 1: Impact of PGD on termination rates of fetuses with Down Syndrome

¹ Winkelman, W. D., Missmer, S. A., Myers, D., & Ginsburg, E. S. (2015). Public perspectives on the use of preimplantation genetic diagnosis. *Journal of Assisted Reproduction and Genetics*, 32(5), 665-675. <https://doi.org/10.1007/s10815-015-0456-8>

² Gyngell, C., & Douglas, T. (2016). Selecting against disability: The liberal eugenic challenge and the argument from cognitive diversity. *Journal of Applied Philosophy*, 35(2), 319-340. <https://doi.org/10.1111/japp.12199>

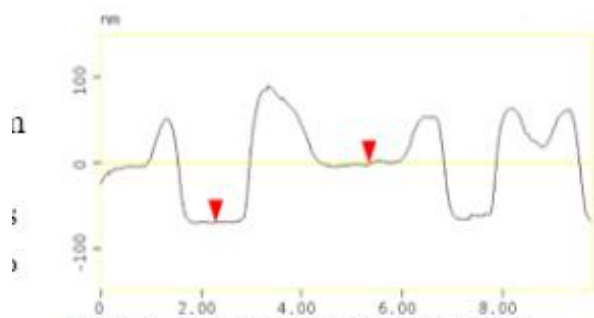
³ Danis, M., Fox, E., Tarzian, A., & Duke, C. C. (2021). Health care ethics programs in U.S. hospitals: Results from a national survey. *BMC Medical Ethics*, 22(1). <https://doi.org/10.1186/s12910-021-00673-9>

(Figure 1) Maxwell, S., Bower, C., & O'Leary, P. (2015). Impact of prenatal screening and diagnostic testing on trends in down syndrome births and terminations in Western Australia 1980 to 2013. *Prenatal Diagnosis*, 35(13), 1324–1330. <https://doi.org/10.1002/pd.4698>

Session 4:

Biomechanics and Stem Cell Differentiation

Chairs: Adam Hansen, Huiting Luo, Shi Fu, Kuan-Che Feng, and Gurtej Singh



Thickness

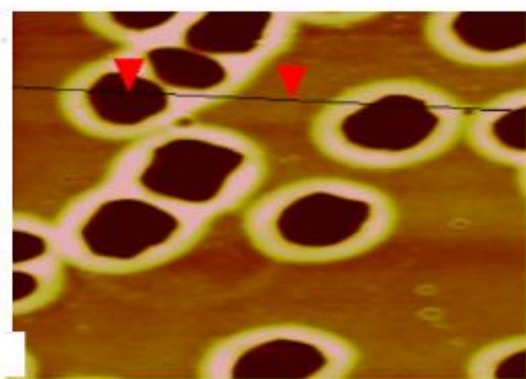


Figure 2. Polystyrene treated w. scCO2

The Decellularization of Tissue Samples Using Supercritical Carbon Dioxide

Jason Goldstein, Rensselaer Polytechnic Institute, Troy, NY 12180-

Shi Fu, Huiting Luo, John Jerome, Miriam Rafailovich, CEAS Stony Brook, NY 11794-2275

We have begun studying a possible method for the decellularization of tissue samples to isolate extracellular matrix (ECM) proteins and fibers to be utilized for various medical applications. The method we are testing entails using supercritical carbon dioxide (scCO₂) as a solvent for cells to dislodge from ECM without reacting with or breaking its overall structure. Carbon dioxide can act as a solvent for such materials while in its supercritical state as its properties change to have a stronger capacity for permeation through various membranous materials [5] (J.W. King 2002), [1](Temelli F. 2000).

Carbon dioxide is the optimal medium for such a reaction as it has a supercritical point at a relatively ambient temperature as well as being reactively inert to most fibers and proteins [1] (Temelli F. 2000).

Figure 1. Shows the phase diagram of CO₂ showing the supercritical point of carbon dioxide is at 31.8°C and 1070 psi [3] (Witkowski 2014 P.119), [4] (Koga, T. 2005). Based on literature the region where the highest density fluctuation and sample swelling that provide the best results would occur at around 32-36°C and 1080-1180 psi [4] (Koga, T. 2005).

As proof of concept, we tested polystyrene film samples under scCO₂ conditions in which we observed swelling of the film from 550 to 670 angstroms or by 27%. This is very close literature values which suggest a minimum of 30% [2] (Jerome L.J. 2005 P.77). The results of scCO₂ exposure can be seen in figure 2 which shows the bubbles popped during Atomic Force Microscopy AFM while figure 3 shows the change in thickness due to the swelling of the polystyrene film.

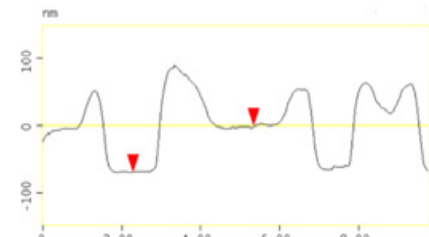


Figure 3. Polystyrene treated w. scCO₂ Thickness

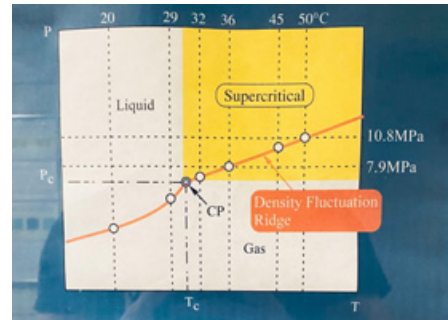


Figure 1. Carbon dioxide Phase Diagram w/ density fluctuation ridge from (Koga, T. 2005).

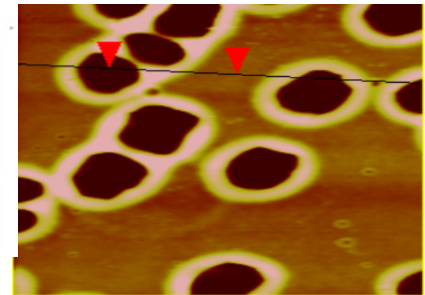


Figure 2. Polystyrene treated w. scCO₂ AFM

Such film swelling suggests that the sample was exposed to high density fluctuations of scCO₂ appropriate for properly separating cells from ECM in tissue samples [1] (Temelli F. 2000), [4] (Koga, T. 2005).

1. Temelli, F. (2000). Lipid extraction from plant and muscle tissues using supercritical CO₂. In *Supercritical fluids: fundamentals and applications* (pp. 489-498). Dordrecht: Springer Netherlands.
2. Jerome, L. J. (2005). *The effects of supercritical carbon dioxide and patterned surfaces on phase separation of thin film polymer blends* (Order No. 3206464). Available from Dissertations & Theses @ SUNY Stony Brook; ProQuest Dissertations & Theses Global. (305366239). Retrieved from Jerome, L. J. (2005). *The effects of supercritical carbon dioxide and patterned surfaces on phase separation of thin film polymer blends* (Order No. 3206464). Available from Dissertations & Theses @ SUNY Stony Brook; ProQuest Dissertations & Theses Global. (305366239).
3. Witkowski, Andrzej & Majkut, Mirosław & Rulik, Sebastian. (2014). Analysis of pipeline transportation systems for carbon dioxide sequestration. *Archives of Thermodynamics*. 35. s. 117-140. 10.2478/aoter-2014-0008.
4. Koga, T., Jerome, J. L., Seo, Y. S., Rafailovich, M. H., Sokolov, J. C., & Satija, S. K. (2005). Effect of density fluctuating supercritical carbon dioxide on polymer interfaces. *Langmuir*, 21(14), 6157-6160.
5. J.W, King. (2002). *Supercritical Fluid Technology for Lipid Extraction, Fractionation, and Reactions*. Lipid Biotechnology. 10.1201/9780203908198.ch34.

Osteogenic Differentiation of Dental Pulp Stem Cells via Titanium Deposition in a Static Magnetic Field

Ethan Lai¹, Michael Wang², Aman Yarlaga³, Kuan-Che Feng⁴, Miriam Rafailovich⁴

¹Phillips Academy, Andover, MA 01810 ²Mounds View High School, Arden Hills, MN 55112 ³Newman Smith High School, Carrollton, TX 75006

⁴Department of Materials Science and Chemical Engineering, Stony Brook University, NY, 11794

Osteogenic differentiation of dental pulp stem cells (DPSCs) offers potential treatments for bone-related diseases such as osteoporosis, which affects more than three million patients in the U.S. and costs the U.S., U.K., and Canada upwards of 5 trillion USD every year.¹ Using static magnetic fields (SMFs) has been shown to induce osteoblast differentiation in rat DPSCs² and cause bone growth through human DPSCs and nano-scaffolds.³ The purpose of this study is to research the effects of a SMF on the osteogenic differentiation of DPSCs attached to a polylactic acid (PLA) coated surface with deposited titanium serving as a scaffold. This method of differentiating DPSCs is crucial to discovering a stem cell-based treatment for endemic bone diseases.

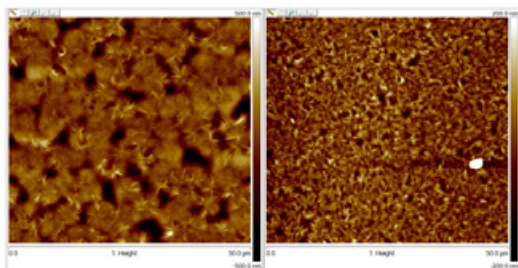


Fig 1. Left: AFM image of 50 μm PLA wafer, RMS = 121 nm. Right: AFM image of 50 μm PLA/ALD wafer, RMS = 48.1 nm.

Osteogenic differentiation of DPSCs was measured for 6 groups. For 4 of the groups, 2 x 2 inch silicon wafers were cleaned, treated with hydrofluoric acid, and coated with PLA via spin casting with a solution of 30 mg/mL of PLA dissolved in chloroform. Two groups were further treated with titanium, which was deposited onto the surface via atomic layer deposition (ALD). DPSCs of strain 13 were isolated from third molar teeth at the Stony Brook Dental School of Medicine. Cells were cultured with 30 mL DPSC media, which was MEM- α , 10% fetal bovine serum (FBS), and 1% glutaMAX. For each passage, the cells were trypsinized after 4 days (70% confluency) to dissolve the ECM, and then replated. After 4 passages, 24 silicon wafers (4 groups) were placed in TCP dishes, and 14 other TCP dishes (2 groups) were used. Agarose was added to each dish to cover the surface along with 2 mL of DPSC media, which was diluted to contain 4×10^4 cells. Three groups (PLA, PLA/ALD, TCP) were then placed in a SMF. After 1 day of incubation, DPSC media was replaced with ascorbic acid and β -glycerophosphate. Reverse Transcription Polymerase Chain Reaction (RT-PCR) will be performed to indicate the expression of osteocalcin (OCN), dentin sialophosphoprotein (DSPP), and alkaline phosphatase (ALP). These expression levels will be used as a baseline to compare expression levels after 28 days.

Images produced by atomic force microscopy (AFM) for the PLA and PLA/ALD groups were analyzed via NanoScope Analysis. Both samples had roughness in the nanometer scale, ensuring roughness will not influence differentiation (Figure 1). Cells were stained with alamarBlue and fluorescence intensity was measured (Figure 2). RNA isolation was done via lysis on day 0. Data obtained on days 20 and 28 will help determine the extent of DPSC differentiation into osteoblasts when compared to that of day 0.

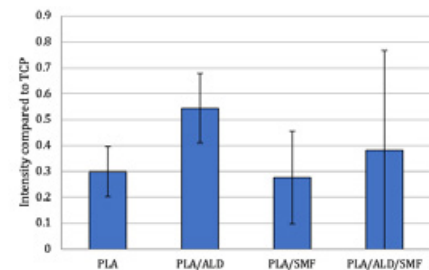


Fig 2. Fluorescence intensity expressed as a fraction of respective TCP group for 4 treatments.

¹ Rashki Kemmak, A., Rezapour, A., Jahangiri, R., Nikjoo, S., Farabi, H., & Soleimanpour, S. (2020). Economic burden of osteoporosis in the world: A systematic review. *Medical journal of the Islamic Republic of Iran*, 34, 154. <https://doi.org/10.34171/mjiri.34.154>.

² Hsu, S. H., & Chang, J. C. (2010). The static magnetic field accelerates the osteogenic differentiation and mineralization of dental pulp cells. *Cytotechnology*, 62(2), 143–155. <https://doi.org/10.1007/s10616-010-9271-3>.

³ Yang Xia, Jianfei Sun, Liang Zhao, Feimin Zhang, Xing-Jie Liang, Yu Guo, Michael D. Weir, Mark A. Reynolds, Ning Gu, Hockin H.K. Xu, Magnetic field and nano-scaffolds with stem cells to enhance bone regeneration, *Biomaterials*, Volume 183, 2018, Pages 151-170, ISSN 0142-9612, <https://doi.org/10.1016/j.biomaterials.2018.08.040>.

Neurogenic Differentiation of Micro-spheric Dental Pulp Stem Cells via Poly-lactic Acid and Poly(4-vinylpyridine) with Resorcinol Diphosphate Clay

Dvita Bhattacharya¹, Catherine Chun², Anita Gaenko³, Alexander Wang⁴, Adam Zaidi⁵, Kuan-Che Feng⁶, Miriam Rafailovich⁶

¹Kent Place School, NJ 07902, ²Ardley High School, NY 10502, ³Huron High School, MI 48105, ⁴Sewickley Academy Senior School, PA 15143, ⁵San Francisco University High School, CA 94115, ⁶Department of Materials Science and Engineering, Stony Brook University, NY 11790 USA

*Authors 1-5 contributed equally to this work

Neurodegenerative diseases pose a major risk to the central nervous system due to the intrinsic non-dividing nature of neurons. Diseases such as Alzheimer's and Parkinson's cause irreversible damage to neuronal networks that cannot be cured through traditional medicine practices^[1]. It is imperative to find methods of generating functionally and morphologically neuronal-like cells from non-neuronal cells under biomimetic conditions. Previously, dental pulp stem cells (DPSCs) have been shown to differentiate into neurons via plating on Poly(lactic Acid) (PLA)^[2], Poly(4-vinylpyridine) (P4VP)^[3], and Poly(lactic Acid) with Resorcinol Diphosphate (RDP) Clay^[4]. In previous studies, a concentration of 20% RDP-Clay was found to provide the highest extent of differentiation into neurons on rough PLA surfaces.^[5] In a recent study, using micro-sphere forming U-bottomed StemFit 3D (SF) plates increased the differentiability of DPSCs^[6]. The aim of this study is to investigate the effects of PLA, P4VP, and RDP-Clay scaffolding on neuronal differentiation of DPSCs plated on 3D micro-sphere

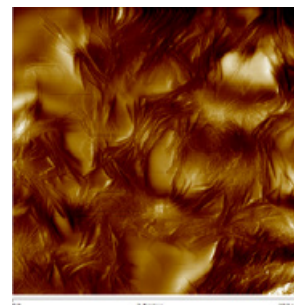
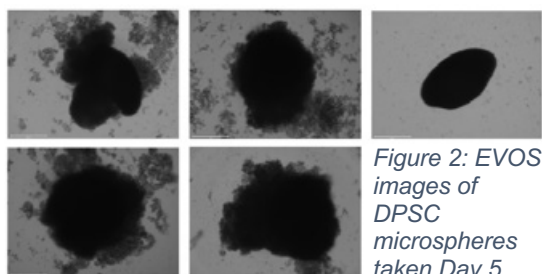


Figure 1: AFM image of PLA-coated wafer with 20% RDP-Clay, 10µm



forming plates.

DPSCs were isolated from strain 13 of the third molar tooth of donors undergoing tooth extraction at Stony Brook School of Dental Medicine. DPSC microbeads (created using SF plates) were plated onto silicon wafers spin-casted with pure PLA, PLA with 20% RDP-Clay, PLA with 30% RDP-Clay, pure P4VP, P4VP with 20% RDP-Clay, and P4VP with 30% RDP-Clay, with 16 wafers per group. The spin-casted surfaces were analyzed with Atomic Force Microscopy (AFM) to ensure

homogeneous roughness across the samples so that the roughness of the surfaces would not be a confounding factor in the growth and differentiation of the DPSCs. The RDP-Clay particles dispersed throughout the PLA with 20% RDP-Clay sample became nuclei for PLA crystals, as shown in Figure 1.

The plated cells will be incubated for 28 days, with growth media replaced every two days until day four after which it is replaced every three days with neuronal media. After the DPSCs reached 60-70% confluency with their container, the old media was aspirated, and 10 mL of trypsin was then used to digest the extracellular matrix and detach the cells from the Tissue Culture Plastic by incubating at 37° C for five minutes^[6]. EVOS images of the DPSC microspheres were taken on Day 5 (figure 2) to provide baseline images of the cells before differentiation. On Day 28, the expression of neuronal markers TUBB3, NES, and NEFM will be measured using Reverse Transcriptase Polymerase Chain Reaction (RT-PCR), and EVOS imaging will be utilized again to observe the differentiation of the cells.

[1] Alzheimer's Disease Fact Sheet. (2023, April 5). National Institute on Aging. <https://www.nia.nih.gov/health/alzheimers-disease-fact-sheet>

[2] Feng, K.-C., Pinkas-Sarafova, A., Ricotta, V., Cuiffo, M., Zhang, L., Guo, Y., Chang, C.-C., Halada, G. P., Simon, M., & Rafailovich, M. (2018). The influence of roughness on stem cell differentiation using 3D printed polylactic acid scaffolds. *Soft Matter*, 14(48), 9838-9846. <https://doi.org/10.1039/c8sm01797b>

[3] Zhang, L., Feng, K.-C., Yu, Y., Chuang, Y.-C., Chang, C.-C., Vadada, S., Patel, R., Singh, V., Simon, M., & Rafailovich, M. (2019). Effect of graphene on differentiation and mineralization of dental pulp stem cells in poly(4-vinylpyridine) matrix in vitro. *ACS Applied Bio Materials*, 2(6), 2435-2443. <https://doi.org/10.1021/acsabm.9b00127>

[4] Justin, A., Zhang, S., & Mak, P. (2023). Observing the Neurogenic Differentiation of Human Dental Pulp Stem Cells (hDPSCs) on Molded Poly-lactic Acid (PLA) Scaffolds with Varying Percentages of Resorcinol Diphenyl Phosphate (RDP) Clay. *Journal of Undergraduate Chemical Engineering Research*, 11.

[5] Farkas, D. H., & Holland, C. A. (2009). Overview of molecular diagnostic techniques and instrumentation. *Cell and Tissue Based Molecular Pathology*, 19-32. <https://doi.org/10.1016/b978-044306901-7.50008-0>

[6] Bu NU, Lee HS, Lee BN, Hwang YC, Kim SY, Chang SW, Choi KK, Kim DS, Jang JH. In Vitro Characterization of Dental Pulp Stem Cells Cultured in Two Microsphere-Forming Culture Plates. *J Clin Med*. 2020 Jan 16;9(1):242. doi: 10.3390/jcm9010242. PMID: 31963371; PMCID: PMC7020027.

Analyzing The Impact of Aging, Cholesterol Inhibition, and Substrate Characteristics on Human Dermal Fibroblasts

Samuel Coopersmith^{1*}, Sharis Hsu^{2*}, Pranav Kota^{3*}, Pia Sodhi^{4*}, Avi Talsania^{5*}, Richard Wong^{6*}, Adam Hansen⁷, Miriam Rafailovich⁷, Steven Fliesler⁸

*Authors 1-6 contributed equally

¹Casa Grande High School, Petaluma, CA, ²Valley Christian High School, San Jose, CA, ³Cedar Falls High School, Cedar Falls, IA, ⁴The Brearley School, New York, NY, ⁵Sachem High School North, Lake Ronkonkoma, NY, ⁶Plainview-Old Bethpage John F. Kennedy High School, Plainview, NY, ⁷Department of Materials Science and Chemical Engineering, Stony Brook University, Stony Brook, NY, ⁸Department of Ophthalmology and Biochemistry, University at Buffalo, Buffalo, NY

Fibroblasts are human dermal cells that assist in the production of the protein collagen, vital for the maintenance of the extracellular matrix (ECM). Dermal fibroblasts exhibit increased stiffness during aging due to a decrease in the rate of collagen production; as the cells stiffen, their viscoelastic properties alter as well¹. The actin cytoskeleton is an essential component of the interaction between fibroblasts and ECM, building contraction forces in the 3D collagen lattice². It is composed of actin filaments that maintain cell shape and motility³. Additionally, cholesterol has significant impacts on the stiffness of cells, as it maintains the fluidity of the membrane.

To examine the effect of substrate characteristics and age on the stiffness of dermal fibroblasts, donor fibroblasts aged 28, 29, 69, and 71 were grown on collagen gels and tissue culture plastic (TCP). Atomic force microscopy (AFM) was used to measure Young's Modulus, an indicator of the stiffness and elasticity of cells. Comparing modulus of all ages of cells, those grown on TCP were 29.50% stiffer than those grown on collagen. Additionally, with respect to age, fibroblast cell and actin cytoskeleton modulus consistently indicated an increase in stiffness with age (Figure 1).

Due to cholesterol's vital role in the cell membrane, effects of its inhibition were studied. Fibroblasts from donors aged 28 and 69 were cultured in a medium with lipid-free serum (LFM) with AY9944, a cholesterol biosynthesis inhibitor. After five days of growth, EVOS imaging was performed to measure the major and minor axes of the fibroblasts (Figure 3). The aspect ratio was calculated to measure the level of adhesion of the cells, an indicator of the health of the culture. One-way ANOVA testing produced statistically significant evidence that there is a difference in aspect ratio between cells grown in medium with fetal bovine serum (control), LFM, and LFM with AY9944. Cells grown in LFM with AY9944 had a much higher aspect ratio, indicating a decreased level of adhesion and therefore a less healthy cell. Cell modulus of the fibroblasts also indicated that cells raised in LFM and LFM with AY9944 were stiffer than those raised in control.

Resorcinol diphenyl phosphate (RDP) Clay is a flame-retardant clay previously used in nanocomposite materials. It is noted for its potential to increase cell adhesion by inducing more favorable surface properties such as reducing the surface contact angle. Cultures of human dermal fibroblasts of ages 29 and 71 were plated on wafers spin-coated with various concentrations of RDP Clay: 5%, 10%, and 20%. Polystyrene wafers were used as a control, while TCP was utilized as a negative control. Plating efficiency, measured in the number of cells present one day after plating, was increased by all concentrations of RDP Clay. For younger cells, a concentration of 10% RDP Clay was most effective, whereas, for older cells, a concentration of 20% RDP clay was most effective.

Analyzing these various properties' effect on fibroblasts has highlighted a significant difference in membrane behavior between old and young cells and the conditions necessary to culture these cells. Future studies include a sterol analysis and an infectivity test with *staphylococcus aureus*.

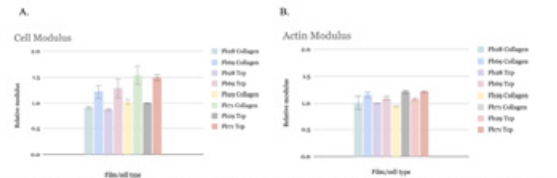


Figure 1. Cell modulus (A) and actin modulus (B) of different aged fibroblasts grown on TCP and collagen

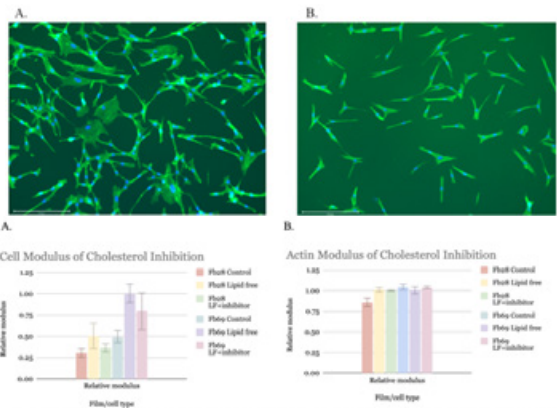


Figure 3. Cell modulus (A) and actin modulus (B) of FB28/FB69 in DMEM, LFM, and LFM+Inhibitor

FB29	Plating Efficiency	FB71	Plating Efficiency
PS	20%	PS	40%
5% RDP	50%	5% RDP	82.5%
10% RDP	70%	10% RDP	80%
20% RDP	30%	20% RDP	140%
TCP	100%	TCP	100%

Figure 4. Plating efficiency of FB29/FB71 in various conditions

¹ Schulze, C., Wetzel, F., Kueper, T., Malsen, A., Muhr, G., Jaspers, S., Blatt, T., Wittern, K.-P., Wenck, H., & Käs, J. A. (2010). Stiffening of human skin fibroblasts with age. *Biophysical Journal*, 99(8), 2434-2442. <https://doi.org/10.1016/j.bpj.2010.08.026>

² Plikus, M. V., Wang, X., Sinha, S., Forte, E., Thompson, S. M., Herzog, E. L., Driskell, R. R., Rosenthal, N., Biernaskie, J., & Horsley, V. (2021). Fibroblasts: Origins, definitions, and functions in health and disease. *Cell*, 184(15), 3852-3872. <https://doi.org/10.1016/j.cell.2021.06.024>

³ Svitkina, T. (2018). The actin cytoskeleton and actin-based motility. *Cold Spring Harbor Perspectives in Biology*, 10(1), a018267. <https://doi.org/10.1101/cshperspect.a018267>

Session 5:

TiO₂ Nanotoxicology

Chairs: Huiting Luo, Shi Fu, and Gurtej Singh

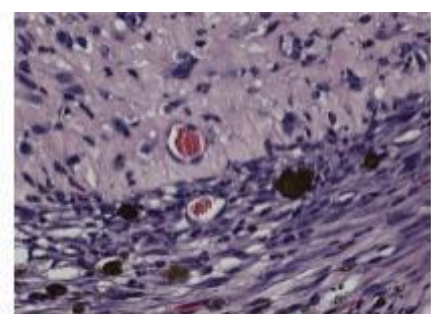


Figure 1. Histology images from left wound of Mouse 1 which received Construct B with TiO₂ NPs.

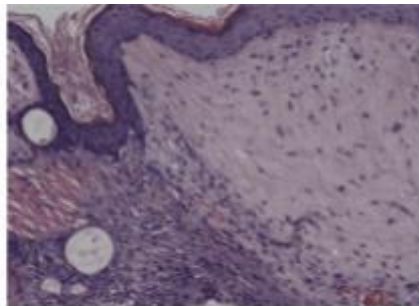


Figure 2. Histology images from left wound of Mouse 2 which received Construct A with TiO₂ NPs.

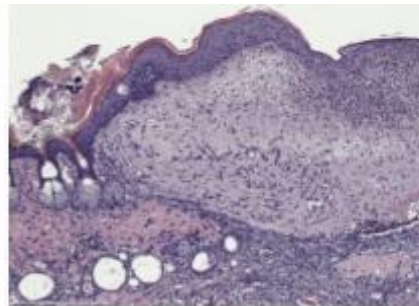


Figure 3. Histology images from left wound of Mouse 3 which received Construct C.

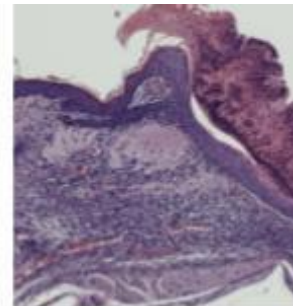


Figure 4. Histology image of wound of Mouse 4 which received RECELL™ skin construct.

Impact of TiO₂ Nanoparticles and RECELL™ on Tissue-Engineered Human Skin Constructs Engrafted in Mice Models

Caitlyn Limbert*¹, Sahana Dhama*², Menachem Lotwin*³, Jacqueline Han*⁴, Grace Wang⁵, Chunuo Chu⁶, Annika Joshi⁷, Rachel Na⁸, Shi Fu⁹, Miriam Rafailovich⁹

*Authors are equal contributors

¹British School Jakarta, Banten 15427, IDN, ²The Wheatley School, Old Westbury, NY 11568, ³Rambam Mesivta, Lawrence, NY, 11552, ⁴Great Neck South High School, Great Neck, NY 11020, ⁵Detroit Country Day School, Beverly Hills, MI, ⁶Shenzhen Middle School, Shenzhen, China, 518000, ⁷Johns Creek High School, Johns Creek, GA, 30097, ⁸Washington University in St. Louis, St. Louis, MO, 63130, ⁹Stony Brook University, Stony Brook, NY, 11794

Skin grafting—the transfer of cutaneous tissue from one part of the body to another—has become the gold standard for treating large wounds as it protects them from the external environment and microorganisms [1]. This study investigates the impact of titanium dioxide (TiO₂) nanoparticles (NPs), a compound commonly found in cosmetic products, on the wound-healing capabilities of skin constructs [2]. Past research has already highlighted TiO₂'s capacity to enhance healing through its antimicrobial and cell growth stimulation properties [3].

To start experimentation, four SHO® hairless mice were placed under anesthesia. After sterilizing the dorsal thorax, saline solution was injected on the left and right sides of the mice's backs to separate the epidermis and dermis from the panniculus muscle. Surgical scissors and tweezers created an 8mm diameter circular wound on both sides of the mice's back. Mouse 1 received skin construct A (vascularized with GFP HUVEC, mural cells, collagen, and fibrin) along with TiO₂ NPs on the left wound and received skin construct B (vascularized without GFP HUVEC, mural cells, collagen, and fibrin) on the right wound. Mouse 2 received skin construct A with TiO₂ NPs on the left wound and skin construct B on the right wound. Mouse 3 received skin construct C (contains only mural cells, collagen, and fibrin) on the left, and received skin construct D (contains only collagen and fibrin) on the right. Mouse 4 received 6.25 µl of RECELL™, then a collagen/fibrin scaffold, and then 6.25 µl of RECELL™ again on the left wound and received a collagen/fibrin scaffold and 6.25 µl of RECELL™ on top of the right wound. Circular silicon covers were placed on all the skin constructs, followed by a wound dressing.

After seven days of recovery, tissue explants were taken from the mice's wound sites and stained with H&E media for histology analysis. Standard H&E staining protocols were applied with xylene, ethanol, and a hematoxylin nuclear stain. Samples were prepared in cover glasses and then individually placed through the Invitrogen EVOS M7000 Imaging System for image generation. Red blood cells, keratinocytes, fat cells, and fibroblasts were

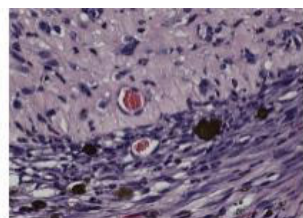


Figure 1. Histology images from left wound of Mouse 1 which received Construct B with TiO₂ NPs.

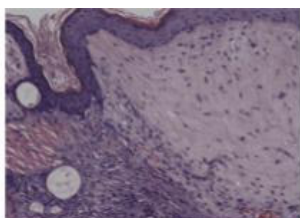


Figure 2. Histology images from left wound of Mouse 2 which received Construct A with TiO₂ NPs.

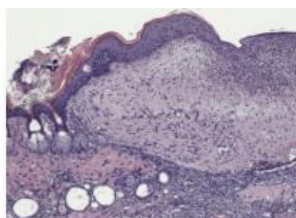


Figure 3. Histology images from left wound of Mouse 3 which received Construct C.

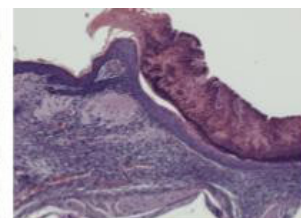


Figure 4. Histology images from left wound of Mouse 4 which received RECELL™ skin construct.

examined. Results generally indicated that the mice's skin could fully heal with the presence of TiO₂ NPs, as seen in Figures 1 and 2. Red blood cells (the red areas) were noted, assisting in the healing process. The high frequency of these red blood cells denotes the substantial amount of healing the mice underwent due to the application of TiO₂ NPs. Furthermore, fibroblasts were noted, which were also generally indicative of healing across the mice. In Figure 3, healing with red blood cells, fat cells, and more were similarly observed, but to a lesser extent. However, for the RECELL™ mice in Figure 4, an unusually high concentration of cells was noted in the histology, making identifying the cells difficult. Hence, the evaluation of healing was unclear for the RECELL™. In both images, it is important to note that mural cells were present. Future studies should observe how collagen, fibrin, RECELL™, and TiO₂ nanoparticles affect wound healing in a larger sample of mice.

[1] Braza, M. E., & Fahrenkopf, M. P. (2022). Split-Thickness Skin Grafts. In *StatPearls*. StatPearls Publishing.

[2] Sanches, P. L., Geaquito, L. R. de O., Cruz, R., Schuck, D. C., Lorencini, M., Granjeiro, J. M., & Ribeiro, A. R. L. (2020). Toxicity Evaluation of TiO₂ Nanoparticles on the 3D Skin Model: A Systematic Review. *Frontiers in Bioengineering and Biotechnology*, 8. <https://doi.org/10.3389/fbioe.2020.00575>

[3] Amer, A. M., Maksoud, A. I. A. E., Abdeen, M. A., Hamdy, A., Mabrok, H. A., Amer, M. M., & El-Sanousi, A. A. (2018). Potency Of Titanium Dioxide Nanoparticles On Skin Wound Healing In Rats. *Research Journal of Pharmaceutical, Biological and Chemical Sciences*.

Analyzing the Effects of Titanium Dioxide Nanoparticles on Angiogenesis

Grace Wang¹, Caitlyn Limbert², Sahana Dhama³, Chunuo Chu⁴, Menachem Lotwin⁵, Annika Joshi⁶, Jacqueline Han⁷, Rachel Na⁸, Shi Fu⁹, Miriam Rafailovich⁹

¹Detroit Country Day School, Beverly Hills, MI, 48025, ²British School Jakarta, Banten 15427, IDN, ³The Wheatley School, Old Westbury, NY 11568, ⁴Shenzhen Middle School, Shenzhen, China, 518000, ⁵Rambam Mesivta, Lawrence, NY, 11552, ⁶Johns Creek High School, Johns Creek, GA, 30097, ⁷Great Neck South High School, Great Neck, NY 11020, ⁸Washington University in St. Louis, St. Louis, MO, 63130, ^{*}Stony Brook University, ⁹Stony Brook University, NY, 11794

Titanium dioxide (TiO₂) nanoparticles (NPs) have high biocompatibility, antimicrobial properties, and light-scattering abilities, making them a valuable tool across a variety of industries [1]. As such, TiO₂ NPs have become strong points of interest in the modern biomedical field. Previous research has demonstrated that TiO₂ NPs induce the activation of human umbilical vein endothelial cells (HUVEC) due to increased expression of adhesion and other molecules associated with inflammatory response [2]. Such NPs may be linked to promoting angiogenesis, a process by which new capillaries are formed from existing vascular structures in the human body [3]. Hence, this research aims to examine the effects of TiO₂ NPs on physiological angiogenesis by isolating TiO₂-treated HUVEC through flow cytometry and cell sorting, imaging time lapses of vascular development using EVOS microscopy, network quantification with Celleste Image Analysis software, and scanning electron microscopy (SEM).

In each process, a control sample, cells cultured in media, and an experimental sample, cells cultured in media with suspended TiO₂ NPs, were tested. To specifically test the uptake of the NPs by the cells, flow cytometry, a process in which lasers are rapidly directed at a line of cells, was conducted, and graphs of the produced wavelengths were created. Due to increasing internal complexity, cells that contained NPs had more light scattering. Cell sorting was then conducted to separate treated cells containing TiO₂ NPs from those that did not contain NPs by passing droplets of cells suspended in saline through an electric field. Results showed that 91% of cells treated with NPs were sorted as containing NPs.

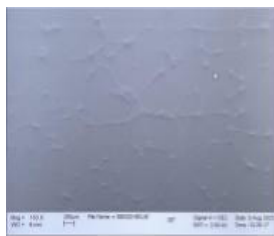


Figure 1. HUVEC networks of the low TiO₂ concentration sample magnified 150X.

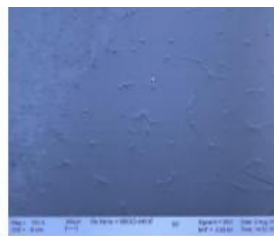


Figure 2. HUVEC networks of the high TiO₂ concentration sample magnified 150X.

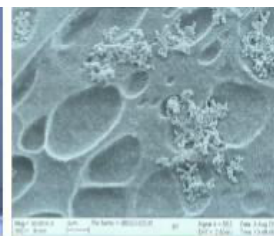


Figure 3. HUVEC surface magnified 30,000X showing TiO₂ NP aggregates and bubbles.

Images of each cell culture were captured every 20 minutes for 18 hours using EVOS microscopy.

Angiogenesis was then quantified using Celleste Image Analysis software. When these results were analyzed, it was confirmed that the experimental group had greater tube/network density than the control group, meaning TiO₂ promotes

angiogenesis. However, the experimental group had a smaller tube length on average due to TiO₂ making the tubes brittle and, therefore, weaker.

SEM imaging was used to visualize the distribution of TiO₂ NPs in the treated cells. In the low-TiO₂ concentration sample, it was observed that matrigel was covering the cells and forming bubbles. The cells formed visible networks (Figures 1 and 2), with some cells stretched to form connections and others remaining short and round to form nodes. TiO₂ NPs aggregated on the surface of cells that formed the nodes in the network (Figure 3), while fewer TiO₂ NPs were observed on long, stretched cells. In the high-TiO₂ concentration sample, the distribution of TiO₂ NPs on the networks was similar to that in the gel-low sample. Cracks were also observed on the surface of the gel.

These results are promising for future studies on promoting angiogenesis with TiO₂ NPs for wound healing applications.

[1] Sanches, P. L., Geaquinto, L. R. O., Cruz, R., Schuck, D. C., Lorencini, M., Granjeiro, J. M., & Ribeiro, A. R. L. (2020). Toxicity Evaluation of TiO₂ Nanoparticles on the 3D Skin Model: A Systematic Review. *Frontiers in Bioengineering and Biotechnology*, 8, 575. <https://doi.org/10.3389/fbioe.2020.00575>

[2] Montiel-Dávalos, A., Ventura-Gallegos, J. L., Alfaro-Moreno, E., Soria-Castro, E., García-Latorre, E., Cabañas-Moreno, J. G., del Pilar Ramos-Godínez, M., & López-Marure, R. (2012). TiO₂ nanoparticles induce dysfunction and activation of human endothelial cells. *Chemical research in toxicology*, 25(4), 920-930. <https://doi.org/10.1021/tx200551u>

[3] Li, T., & Zhang, T. (2021). The Application of Nanomaterials in Angiogenesis. *Current stem cell research & therapy*, 16(1), 74-82. <https://doi.org/10.2174/1574888X15666200211102203>

Analyzing the Impacts of Titanium Dioxide Nanoparticles on the Upregulation of EGFP

Jacqueline Han*¹, Menachem Lotwin*², Annika Joshi*³, Caitlyn Limbert⁴, Sahana Dhama⁵, Chunuo Chu⁶, Grace Wang⁷, Rachel Na⁸, Shi Fu⁹, Miriam Rafailovich⁹

*Authors are equal contributors

¹ Great Neck South High School, Great Neck, NY 11020, ²Rambam Mesivta, Lawrence, NY 11552, ³ Johns Creek High School, Johns Creek, GA 30097, ⁴ British School Jakarta, Banten 15427, IDN, ⁵The Wheatley School, Old Westbury, NY 11568, ⁶ Shenzhen Middle School, Shenzhen, China, 518000, ⁷ Detroit Country Day School, Beverly Hills, MI 48025, ⁸Washington University in St. Louis, St. Louis, MO 63130, ⁹Stony Brook University, Stony Brook, NY 11794

Titanium dioxide (TiO₂) nanoparticles (NPs) are used in various commercial products like sunscreen for their UV-reflecting capabilities [1]. EGFP is a protein that is used as a biological marker because it emits green fluorescence in the presence of UV light [2]. Preliminary research yielded that the accumulation of certain types of TiO₂ NPs in cells was related to the fluorescence enhancement of such cells, indicating the fluorescence-enhancing capabilities of TiO₂ NPs in the context of photodynamic analysis [3]. This research will determine titanium dioxide nanoparticles' impact in terms of their fluorescence-enhancing capabilities for EGFP. The hypothesis of this study is that the addition of titanium dioxide will enhance the green fluorescence of EGFP.

TiO₂-DMEM solutions were mixed into concentrations of 0.1mg/mL, 0.2 mg/mL, and 0.4 mg/mL. To create the 0.4 mg/mL solution, 0.378 mL of TiO₂ DMEM (7.4mg/mL concentration) was mixed with 6.622 mL of EGM media. 3 mL of the 0.4mg/mL solution was added to 3 mL of EGM media to create the 0.2 mg/mL solution. Finally, to create the 0.1 mg/mL solution, 2 mL of the 0.2 mg/mL solution was mixed with 2 mL of EGM. Before the solutions were treated, the TiO₂-DMEM solutions were mixed gently with a P1000 mechanical micropipette.

Controls containing the TiO₂ NPs and no cells were also created for comparison. TiO₂ solutions were added to a fibroblast cell culture and a HUVEC cell culture with a cell plating procedure, with each well having ~10,000 cells.

Images were taken of each sample through the Invitrogen EVOS M7000 Imaging System over two 24-hour periods and one 48-hour period (Figure 1). ImageJ software splits each image by color to isolate green fluorescence. Then, the mean intensity of green fluorescence was measured. The mean green intensity was first analyzed within the controls and used as a threshold for analyzing images of the cell cultures. Once recorded, the data was graphed.

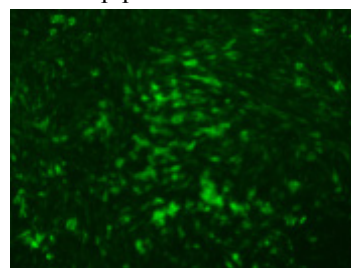


Figure 1. Fibroblast cell culture with 0.4 mg/mL TiO₂ solution on day 3

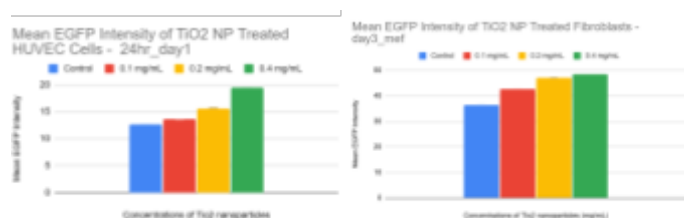


Figure 2. Different concentrations of TiO₂ treated HUVEC on the mean EGFP density on Day 1 (+/- 1SEM).

Figure 3. Different concentrations of TiO₂ treated fibroblasts on Day 3 (+/- 1SEM).

Generally, as concentrations of TiO₂ increased, the mean green intensity also increased (Figures 2 and 3). On day 1 of experimentation, the 0.4 mg/mL of TiO₂ with fibroblasts and HUVECs had the greatest mean intensity. Such patterns continued for days 2 and 3 for the TiO₂-treated HUVECs, and day 3 for the TiO₂-treated fibroblasts. However, for day 1 of the TiO₂-treated HUVECs, the 0.2 mg/mL concentration group had the highest mean EGFP intensity, as opposed to the 0.4 mg/mL group. Overall, however, the results support the hypothesis. Future studies should explore the impact of TiO₂ NPs on the upregulation of the EGFP gene in HUVECs and fibroblasts.

[1] Cinelli, R. A., Ferrari, A., Pellegrini, V., Tyagi, M., Giacca, M., & Beltram, F. (2007). The enhanced green fluorescent protein as a tool for the analysis of protein dynamics and localization: local fluorescence study at the single-molecule level. *Journal of Photochemistry and Photobiology A*, 71(6), 771-776. [https://doi.org/10.1562/0031-8655\(2000\)07110771TEGFPA2.0.CO2](https://doi.org/10.1562/0031-8655(2000)07110771TEGFPA2.0.CO2)

[2] Kanehira, K., Yano, Y., Hasumi, H., Fukuhara, H., Inoue, K., Hanazaki, K., & Yao, M. (2019). Fluorescence Enhancement Effect of TiO₂ Nanoparticles and Application for Photodynamic Diagnosis. *International Journal of Molecular Sciences*, 20(15). <https://doi.org/10.3390/ijms20153698>

[3] Sanches, P. L., Geaquito, L. R. de O., Cruz, R., Schuck, D. C., Lorencini, M., Granjeiro, J. M., & Ribeiro, A. R. L. (2020). Toxicity Evaluation of TiO₂ Nanoparticles on the 3D Skin Model: A Systematic Review. *Frontiers in Bioengineering and Biotechnology*, 8. <https://doi.org/10.3389/fbioe.2020.00575>

Keratinocyte Uptake of Titanium Dioxide Nanoparticles: Effects on Cell Differentiation and Proliferation

Ashley Huang¹, Derek Zhang², Dina McGinley³, Dr. Marcia Simon⁴, Dr. Kuan-Che Feng⁵, Dr. Miriam Rafailovich⁵

¹Syosset High School, Syosset, NY 11791; ²The Wheatley School, Old Westbury, NY 11568; ³Farmingdale State College, Farmingdale, NY 11735; ⁴Department of Oral Biology and Pathology, Stony Brook University, Stony Brook, NY 11794; ⁵Department of Material Science and Engineering, Stony Brook University, Stony Brook, NY 11794

*Authors 1-2 contributed equally to this work

Titanium dioxide nanoparticles (TiO₂ NPs) are widely used in cosmetics, sunscreen, plastics, foods, and drugs for their whitening properties, UV absorption capabilities, and their potential usage as antibacterial reagents¹. Previous studies have shown that these NPs do not penetrate the stratum corneum and hence do not come into direct contact with viable keratinocytes (KCs)². However, TiO₂ NPs used in wound treating creams and wound care dressings raise concern because these NPs can come into direct contact with viable KCs³. In previous studies conducted at Stony Brook University, TiO₂ NPs were found to affect the expression of the protein filaggrin but not the protein corneodesmosin. The current study further explores NP influence on both epithelial stem cells and their differentiation.

In this experiment, three flasks of KC cells co-cultured with irradiated 3T3 mouse cells were fed with growth media (70% confluence). 15 mL of a 0.8 mg/mL solution of rutile TiO₂ NPs (20-50 nm) was added to two of the flasks; the other flask was left as a control. The cells were incubated overnight. Each flask was washed 2-3 times using PBS-EDTA to remove 3T3 cells as well as excess TiO₂ NPs in preparation for cell sorting.

Using Fluorescence-activated cell sorting (FACS), treated and control cells were sorted based on 'high' and 'low' side scatter (Figure 1). Treated cells with high SSC were considered to have taken up TiO₂ NPs; treated cells with low SSC did not take up TiO₂ NPs. Insufficient cells were collected for RT-PCR because of cell-to-cell aggregation because of excess TiO₂ NPs adhered to the surface of the cells.

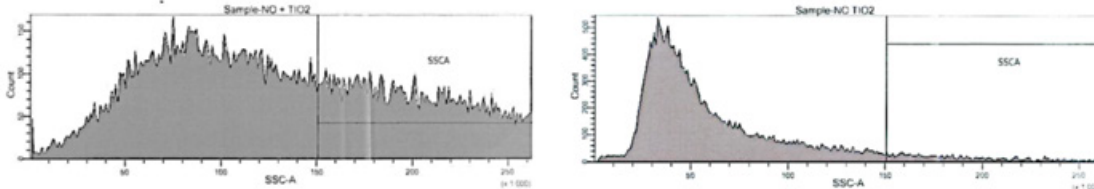


Figure 1. SSC of treated cells (left) and control cells (right)

The cells from the cell sort were then plated for Colony Forming Efficiency (CFE). 12 culture dishes containing 500 cells each were plated: 6 control plates, 3 plates of 'high' SSC, and 3 plates of 'low' SSC. After 14 days, each culture dish was washed with PBS and stained with Rhodamine B. Colonies ≥ 2 mm were counted. Although low SSC cells tended to have slightly greater proliferation compared to high SSC cells, no statistically significant data was collected. The low CFE observed may be due to time in suspension and formation of cell aggregates.

Scanning electron microscopy (SEM) was used to visualize KC uptake of TiO₂ NPs. For this process, cells were plated onto glass coverslips, grown for 48 hours, and then fixed with 2% glutaraldehyde. Samples were then dehydrated using 30-minute incubations with 30, 50, 70, 90, and 100% ethanol. Unexpectedly, the cells that adhered to the glass coverslips contained no TiO₂ NPs (Figure 2). It is possible that KCs that took up TiO₂ NPs did not adhere, or that viable KCs did not uptake TiO₂ NPs. The former is consistent with the expulsion of altered KCs from a healthy epidermis.

Ongoing work includes CFE determination with cells treated at a lower TiO₂ concentration of 0.1 mg/mL, and RT-PCR of differentiation markers in cells that took up NPs with comparisons to those that are NP free.

Acknowledgements: We thank Dr. Jim Quinn of the Department of Materials Science and Chemical Engineering at Stony Brook University for analyzing the SEM images; We thank the Research Flow Cytometry Laboratory at the Stony Brook University Renaissance School of Medicine for conducting the cell sort; we thank Dr. Alice Shih for preparing and culturing KCs in preparation for cell sort

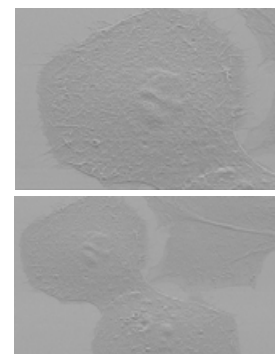


Figure 2. SEM images of high SSC treated KCs

¹Ziental, D., Czarczynska-Goslinska, B., Mlynarczyk, D. T., Glowacka-Sobotta, A., Stanisz, B., Goslinski, T., & Sobotta, L. (2020). Titanium Dioxide Nanoparticles: Prospects and Applications in Medicine. *Nanomaterials* (Basel, Switzerland), 10(2), 387. <https://doi.org/10.3390/nano10020387>

²Hou, J., Wang, L., Wang, C., Zhang, S., Liu, H., Li, S., & Wang, X. (2019). Toxicity and mechanisms of action of titanium dioxide nanoparticles in living organisms. *Journal of environmental sciences (China)*, 75, 40–53. <https://doi.org/10.1016/j.jes.2018.06.010>

³Nikpasand, A., & Parvizi, M. R. (2019). Evaluation of the Effect of Titanium Dioxide Nanoparticles/Gelatin Composite on Infected Skin Wound Healing; An Animal Model Study. *Bulletin of emergency and trauma*, 7(4), 366–372. <https://doi.org/10.29252/beat-070405>

Session 6:

X-Ray Analysis of

Materials

Chairs: Karin Hasegawa

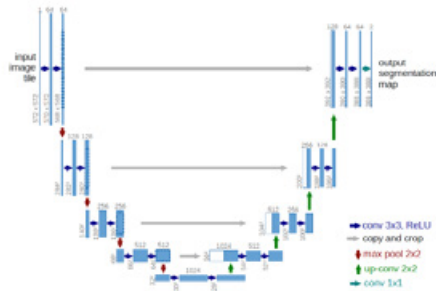


Fig. 1: structure of a Vanilla UNET model

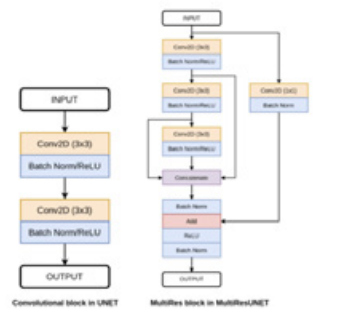
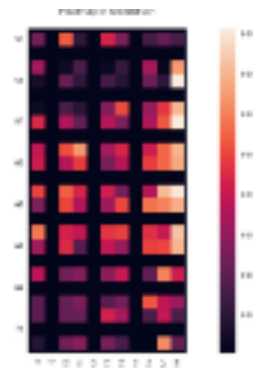


Fig. 2: Comparison of the convolutional block in the UNET and the MultiRes block in the MultiResUNET



Utilizing Machine Learning to Predict Sinusitis Through the Segmentation of Maxillary Sinus Images

Anirudh Srinivasan¹, Karin Hasegawa², Yuefan Deng²

¹duPont Manual High School, Louisville, KY, 40208, ²Department of Applied Mathematics and Statistics, Stony Brook University, Stony Brook, NY, 11794

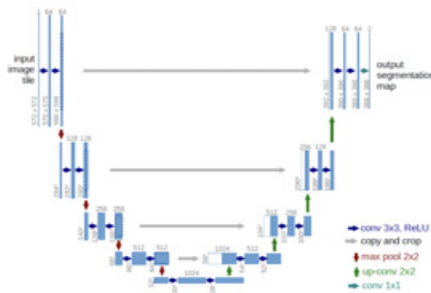
This project aims to develop an innovative AI-driven approach for predicting sinus infections using advanced machine-learning techniques. Sinusitis, a common health concern affecting millions worldwide, necessitates early detection and accurate diagnosis to guide appropriate treatment and improve patient outcomes. In dentistry, researchers have shown significant interest in the maxillary sinuses due to their clinical importance. These large sinuses are susceptible to maxillary sinusitis, leading to symptoms like headaches, pharyngeal discharge, and fever-like manifestations. Carcinoma in the maxillary sinuses can cause dental pain and block the

nasolacrimal duct, while the concept of oro-antral communication intrigues dental researchers^[1]

To achieve effective segmentation of CBCT scan images of the maxillary sinuses and predict sinusitis, a U-Net model, specialized in biomedical image segmentation, was chosen. The U-Net's encoder-decoder structure with skip connections enables the capture of contextual information and fine details.

The encoder path reduces spatial resolution and increases feature channels, while the decoder path utilizes transposed convolutions for upsampling. This architecture has proven successful in medical imaging and tasks requiring precise segmentation^[2]. An alternative to U-Net is the MultiResUNET, sharing similarities but featuring three connected 3x3 convolutional layers with batch normalization and ReLU, whose outputs are concatenated.

Fig. 1: structure of a Vanilla UNET model



Using data from the Medical Segmentation Decathlon dataset in place of the Maxillary Sinus Images (due to pending IRB approval for access to sensitive patient data), the 3D MultiResUNET was implemented.

First, the data had to be converted from a .nii.gz or NIFTI file format to a .png file format to ensure readability and data visualization. Subsequently, the model was developed using TensorFlow and was tested for one lung in the dataset (due to computer RAM issues) and the results are seen in Fig. 2. As shown the model did an accurate job segmenting the images from the ground truths obtaining a Jacard index of approximately 57%, a Dice Coefficient of approximately 73%, and an accuracy of approximately 98% showing that the MultiResUNET was effective at segmenting the lung images, and can effectively be applied to the

Maxillary Sinus Image data to come.

MultiResUNET was implemented.

First, the data had to be converted from a .nii.gz or NIFTI file format to a .png file format to ensure readability and data visualization. Subsequently, the model was developed using TensorFlow and was tested for one lung in the dataset (due to computer RAM issues) and the results are seen in Fig. 2. As shown the model did an accurate job segmenting the images from the ground truths obtaining a Jacard index of approximately 57%, a Dice Coefficient of approximately 73%, and an accuracy of approximately 98% showing that the MultiResUNET was effective at segmenting the lung images, and can effectively be applied to the

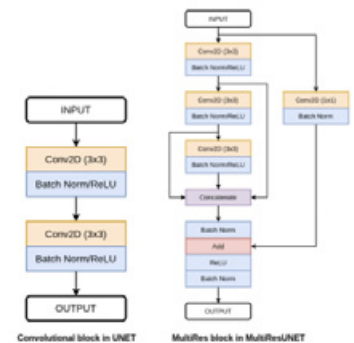


Fig. 2: Comparison of the convolutional block in the UNET and the MultiRes block in the MultiResUNET

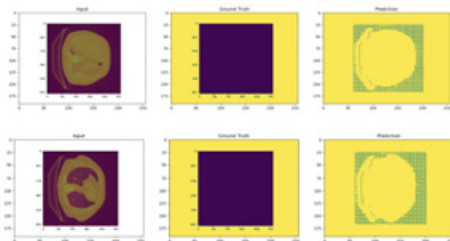


Fig. 3: MultiResUNET image segmentation results for one lung

[1] Maxillary sinus. (2023, July 7). In *Wikipedia*. https://en.wikipedia.org/wiki/Maxillary_sinus

[2] K, Bharath. "U-Net Architecture for Image Segmentation." Paperspace Blog, 6 July 2021, blog.paperspace.com/unet-architecture-image-segmentation/.

Advanced X-Ray Characterization of Fusion Materials

Anthony Zhu¹, Michael Zhang², Ryan Kim³, David Sprouster⁴, Miriam Rafailovich⁴

¹Barrington High School, Barrington, IL 60010, ²Livermore High School, Livermore, CA 94550, ³Thomas Jefferson High School for Science and Technology, Alexandria, VA 22312, ⁴Stony Brook University, Stony Brook, NY 11794

In the present work, we describe our efforts employing advanced non-destructive X-ray-based characterization to support the fabrication and post-irradiation examination of materials for advanced fusion energy systems. Specific material systems include castable nanostructured alloys (CNAs) and neutron irradiated tungsten. We quantify the microstructural and atomic properties of advanced first-wall materials through two-dimensional mapping and high-throughput X-ray diffraction. X-ray-based characterization techniques provide complimentary quantitative insights across multiple length scales needed to fill critical knowledge gaps and predict long-term behavior and performance [1].

CNAs have been under development by the fusion program over the last decade and are meant to provide enhanced elevated temperature performance as compared to reduced activation ferritic martensitic (RAFM) steels through the internal formation of irradiation-stable and dislocation-pinning precipitates [2]. In this way, the CNAs are a potentially more practical high-temperature option for high-heat-flux or other challenging fusion applications. The uniformity of the microstructure and engineered precipitates through various cast steel plates are investigated here by constructing 2D microstructural maps of X-ray diffraction mapping utilizing synchrotron-based X-ray diffraction. Tungsten is presently the leading plasma-facing material candidate due to its high melting point, resistance to sputtering, and chemical compatibility with tritium [3]. However, extended exposure of W to fusion plasmas and intense 14 MeV neutrons, resilience against plasma-induced surface damage (cracking, erosion/exfoliation, and fuzz formation), and degradation of bulk mechanical properties due to neutron irradiation raise significant concerns about its stability.

We performed XRD experiments of unirradiated and neutron-irradiated polycrystalline W alloys after low-dose irradiation at 800°C (0.1 dpa) and after high irradiation temperature (>800°C). 2D XRD mapping of six CNA alloy plates was performed at the PDF beamline at the National Synchrotron Light Source-II. The wavelength of the incident X-rays was 0.1665 Å at an energy of 74 keV. Analysis of the XRD patterns and 2D-XRD mapping data sets allows the determination of the lattice strain, change in microstructure parameters, and formation of secondary phases.

We developed a high-throughput quantitative XRD analysis to generate spatially dependent 2D mappings of the microstructural data of our samples as shown in Figure 1. Using a Perl script, we generated an instructions file to run batch analysis of our data through the Materials Analysis Using Diffraction (MAUD) software and placed the results into a spreadsheet. A Python script, utilizing the Seaborn library, then uses the spreadsheet to generate heatmaps that plot our collected data in 2D mappings.

The quantitative XRD analysis of the exposed CNA samples show a complex hydrogen uptake in the metal carbide crystallites. The lattice expansion and crystallite size reduction will have non-negligible implications on the mechanical properties and retention of transmutation products within this important structural component. The heatmaps visualize microstructural features (carbides) that provide strength to the steel and are trapping sites for radiation-induced gaseous products. The steels are strangely affected by the exposure and expand (lattice expansion).

Our initial success in demonstrating the effective characterization of fabricated and as-irradiated materials supports our goal of fabricating functionally graded or composited first wall tile structures (i.e., W-CNA), which may be essential to mitigate the very high heat flux loading anticipated as we move beyond ITER towards DEMO-like fusion systems.

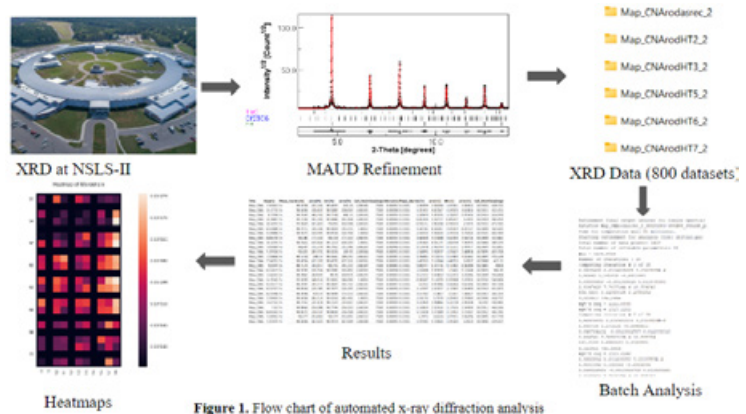


Figure 1. Flow chart of automated x-ray diffraction analysis

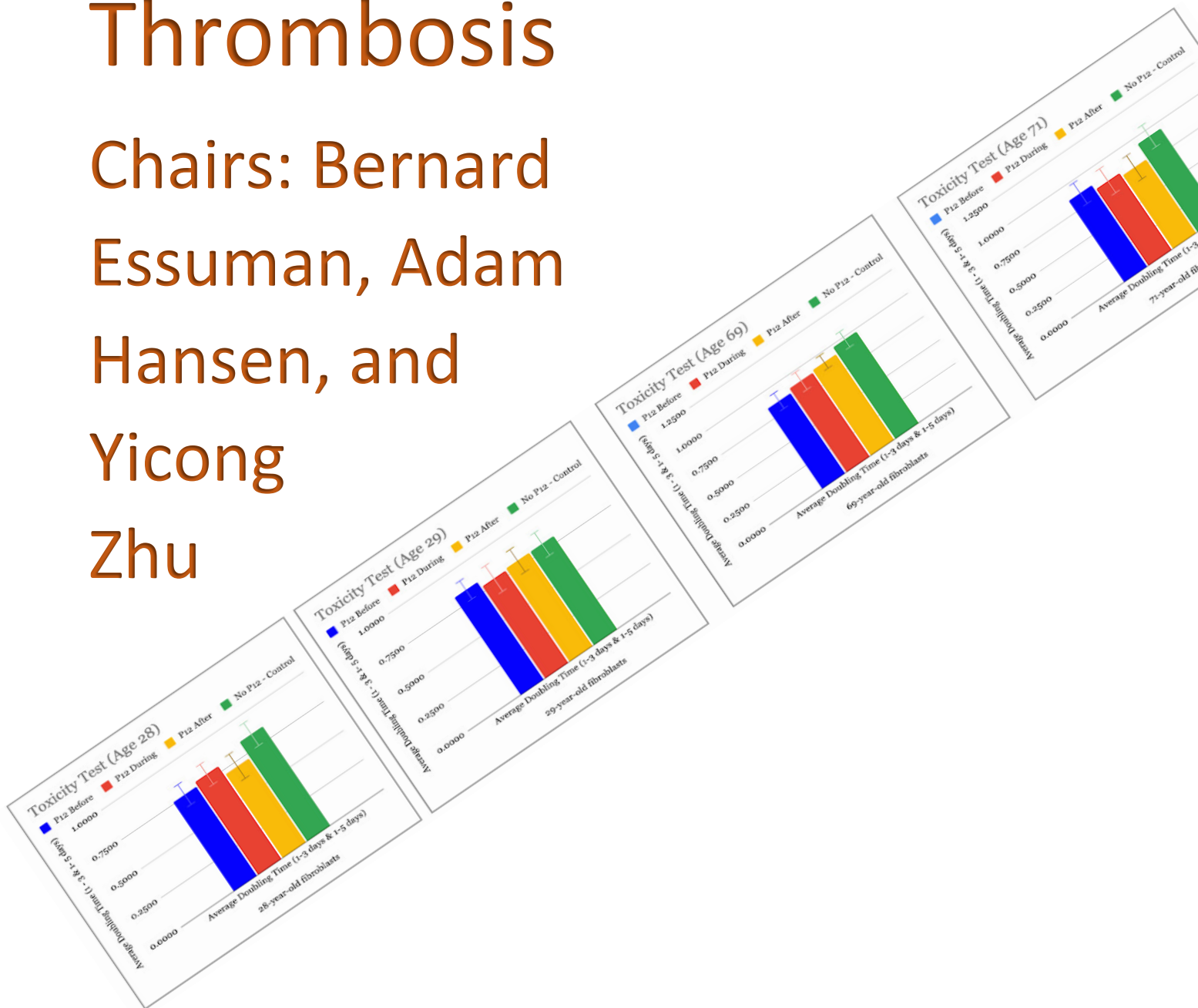
¹ Sprouster, D., Trelwicz, J., Snead, L., Hu, X., Morrall, D., Koyanagi, T., Parish, C., Tan, L., Kato, Y., & Wirth, B. (2020, October 8). *Advanced Synchrotron Characterization Techniques for Fusion Materials Science*. Journal of Nuclear Materials. <https://www.osti.gov/servlets/purl/1820770>

² Tan, L., Katoh, Y., & Snead, L. L. (2018, May 9). *Development of castable nanostructured alloys as a new generation RAFM steels*. Journal of Nuclear Materials. <https://www.osti.gov/pages/servlets/purl/1479784>

³ V. Philipps, Tungsten as material for plasma-facing components in fusion devices, J. Nucl. Mater. 415 (2011) S2, <https://doi.org/10.1016/j.jnucmat.2011.01.110>.

Session 7: Fibrinogen and Thrombosis

Chairs: Bernard
Essuman, Adam
Hansen, and
Yicong
Zhu



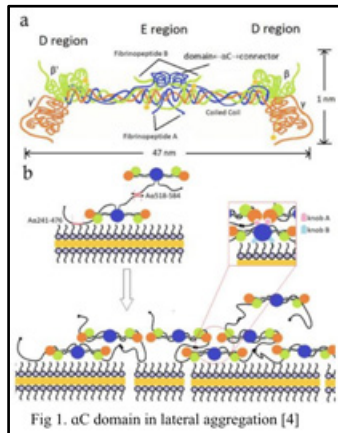
In-Silico Studies on Fibrinogen Domain Adsorption on Polylactic Acid

Matthew Sun^{1*}, Erin Wong^{2*}, Richard Zhang^{3*}, Bernard Essuman⁴, Miriam Rafailovich⁴, Yuefan Deng⁴

¹North Carolina School of Science and Mathematics, Durham, NC 27705 ²Great Neck South High School, Great Neck, NY 11020, ³Conestoga High School, Berwyn, PA 19312 ⁴Stony Brook University, Stony Brook, NY 11794

*Authors contributed equally to this work

Fibrinogen, a vital blood clotting protein, transforms into active fibrin via thrombin activation, creating a scaffold for clots. It is key in interactions with medical device materials, especially those prone to adverse clotting. Investigating material-blood protein interactions, like those with polylactic acid (PLA), which is used for its biocompatibility, can aid in preventing device-induced clots and enhancing safety [1][2].



Prior research demonstrates the impact of surface chemistry on adsorbed fibrinogen's conformation, orientation, fiber formation, and platelet adhesion [3]. This is attributed to distinct surface properties of fibrinogen domains: D and central E (C_e) domains are hydrophobic, while the α C domain is hydrophilic. On hydrophobic surfaces like PLA, D and C_e domains strongly adhere (with C_e showing weaker adherence) while the α C domain remains detached, promoting lateral aggregation via α C domain linkage (Fig 1.) [3]. Conversely, on hydrophilic surfaces, α C domains bind to the C_e domain, reducing lateral aggregation [3]. Additionally, P12, a proven stent coating, reduces fibrinogen fiber count on hydrophobic surfaces and supports endothelial cell growth without adverse effects [4]. P12 obstructs the D domain's hole, impeding fiber formation; it potentially affects α C domains by surface binding as well.

To study this critical interaction between P12 and fibrinogen, we conducted molecular dynamics simulations. In order to lessen the computational cost, the problem was divided into parts for the three fibrinogen domains. For the D and C_e domains, the simulations were identical: run each domain alone in water, each domain face down on PLA, and each domain face up on PLA. By accounting for the different orientations of the domains on PLA, the actual binding configuration for each domain could be deduced as it is currently unknown. For the central complex (α C and C_e domain), umbrella sampling and steered molecular dynamics (SMD) were done to gain insight into the free energy landscape of the complex when the α C domains are separated and to determine the force necessary to pull the α C domain segments apart.



After 2.34 ns of D domain simulation, the total energy of the system was $-2.99888e+06$. After 6.01 ns of C_e domain simulation, the total energy of the system was $-1.38023e+06$. Both domains of the fibrinogen protein were shown to have stably folded, with reasonably invariant radii of gyration. Our next steps include running simulations with the D and C_e domains face down and face up on PLA, to examine the lowest energy conformations and chemical behaviors of these surface interactions. Moreover, we will use data from the SMD and umbrella sampling to train a machine learning model to predict whether the α C domain segments will be pulled apart, given various factors such as thermodynamics values and relative orientation.

1. Jaffer, I. H., Fredenburgh, J. C., Hirsh, J., & Weitz, J. I. (2015). Medical device-induced thrombosis: What causes it and how can we prevent it? *Journal of Thrombosis and Haemostasis*, 13(S1), S72–S81. <https://doi.org/10.1111/jth.12961>
2. da Silva, D., Kaduri, M., Poley, M., Adir, O., Krinsky, N., Shainsky-Roitman, J., & Schroeder, A. (2018). Biocompatibility, biodegradation and excretion of polylactic acid (PLA) in medical implants and theranostic systems. *Chemical Engineering Journal (Lausanne, Switzerland: 1996)*, 340, 9–14. <https://doi.org/10.1016/j.cej.2018.01.010>
3. Zhang, L., Casey, B., Galanakis, D. K., Marmorat, C., Skoog, S., Vorvolakos, K., Simon, M., & Rafailovich, M. H. (2017). The influence of surface chemistry on adsorbed fibrinogen conformation, orientation, fiber formation and platelet adhesion. *Acta Biomaterialia*, 54, 164–174. <https://doi.org/10.1016/j.actbio.2017.03.002>
4. Doilidov, A., El-Saieh, S., Faria, S., & Lo, P. (n.d.). The Effect of P12 Peptide on Fibrinogen Fiber Formation and Endothelial Cell Attachment on Polystyrene.

Thrombosis: An analysis of pseudo-thrombi to understand collagen-fibrin interaction

Sripradha Manikantan¹, Huiting Luo², Shi Fu², Robert Wong², Shiffoni Sukhlal²

¹James Logan High School, Union City, CA 94587, ²Stony Brook University, Stony Brook, NY 11794

When vascular injury occurs, the exposed tissue factor initiates thrombosis through a cascade of events including the aggregation of platelets and their coagulation, which in turn triggers the formation of fibrin and collagen to wrap around the coagulated platelets. Clinical treatment of thrombosis in patients with deep vein thrombosis or pulmonary embolism uses fibrinolytics in order to break down the fibrin and cause thrombolysis [1]. However, for arterial thrombi, fibrinolytics do not often respond well. Research shows that collagen plays a dual role in thrombosis [2] by stimulating glycoprotein VI to promote platelet accumulation and by activating factor XII to promote blood coagulation. In this research, we intend to understand the disparity between venous and arterial thrombosis by studying the interaction between collagen and fibrin in thrombi. Within this overarching goal, two sub-hypotheses were tested. Our first hypothesis used hydroxyapatite to test the collagen-fibrin interaction with calcium to see the presence of biomineralization within the thrombi. Our second hypothesis was that the interaction of collagen and fibrin formed a new biomaterial. In due course of this project, we hope to uncover new targets for effectively treating arterial thrombosis.

After staining the thrombi from the vessels of in-vivo models, we used SEM imaging to track fibrin growth. Hydrogel samples of collagen, fibrin, and an equal mix of both were made for the experimental purpose. XRF imaging was used to determine the actual elements present in the samples. Raman spectroscopy was used to identify the intensity of collagen and fibrin based on the presence of hydroxyapatite.

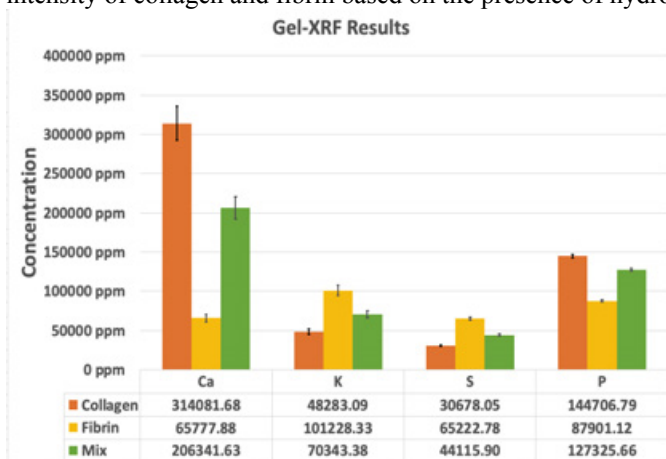


Figure 1. XRF imaging showing the concentration of various element in the in-vitro hydrogel samples

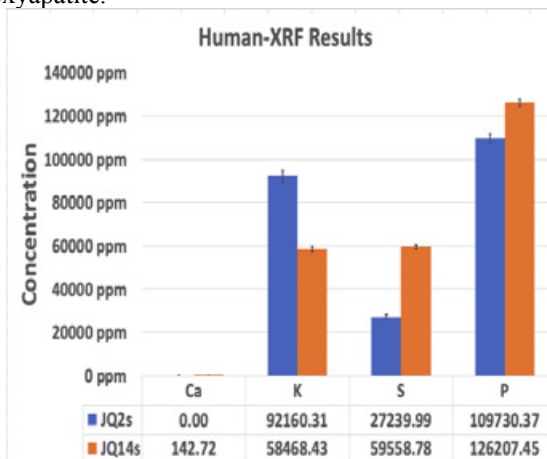


Figure 2. XRF imaging showing the concentration of various elements in the in-vivo human samples

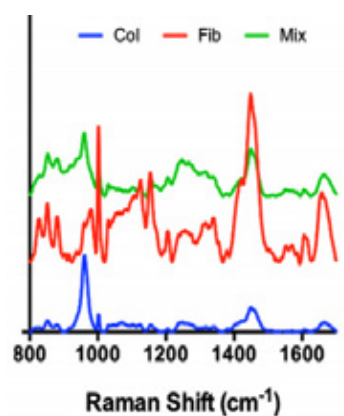


Figure 3. Peaks from Raman spectroscopy showing the intensity of biomineralization (at 980 nm) in collagen, fibrin, and the mix

SEM imaging revealed that fibrin density grows toward the center of the thrombi. Analysis of the XRF data was found to be different between in-vitro and in-vivo models. The in-vitro XRF revealed that biomineralization is significant in collagen when compared to fibrin (**Figure 1**). The calcium to phosphate ratio for the mixture of collagen and fibrin samples is 1.67, validating that hydroxyapatite, a mineral, is present in the sample. The in-vivo XRF data depicting the elemental samples of venous thrombi of human sample (**Figure 2**) shows that the concentration of calcium is insignificantly low due to a high fibrin to collagen ratio. This answers why fibrinolytics works better to break down fibrin in venous clots. Also, Raman spectroscopy showed a greater peak for collagen when compared to fibrin or the collagen/fibrin mix (**Figure 3**). This means that fibrin has very little biomineralization. Also, the unique peaks in the mix graph suggest a new possible biomaterial due to the collagen-fibrin interaction. Further research will use XRF to measure the hydroxyapatite concentration in arterial thrombi, confirming our overall hypothesis about the compositional differences of collagen and fibrin in arterial and venous thrombi. Also, the role of enriched fibroblasts in thrombolysis shall be analyzed.

[1] Baig, Muhammad U, and Jeffrey Bodle. "Thrombolytic Therapy." *National Library of Medicine*, StatPearls Publishing, 2020, www.ncbi.nlm.nih.gov/books/NBK557411/.

[2] van der Meijden, Paola E. J., et al. "Dual Role of Collagen in Factor XII-Dependent Thrombus Formation." *Blood*, vol. 114, no. 4, 23 July 2009, pp. 881-890, https://doi.org/10.1182/blood-2008-07-171066.

Viability of a Novel Peptide P12 as an Antithrombotic Agent

Samuel Coopersmith^{1*}, Sharis Hsu^{2*}, Pranav Kota^{3*}, Pia Sodhi^{4*}, Avi Talsania^{5*}, Richard Wong^{6*}, Adam Hansen⁷, Miriam Rafailovich⁷

*Authors 1-6 contributed equally

¹Casa Grande High School, Petaluma, CA, ²Valley Christian High School, San Jose, CA, ³Cedar Falls High School, Cedar Falls, IA, ⁴The Brearley School, New York, NY, ⁵Sachem High School North, Lake Ronkonkoma, NY, ⁶Plainview-Old Bethpage John F. Kennedy High School, Plainview, NY, ⁷Department of Materials Science and Chemical Engineering, Stony Brook University, Stony Brook, NY

Fibrinogen is a plasma-soluble protein necessary for blood clot formation. During coagulation, the protease thrombin cleaves into insoluble fibrin, which accumulates and promotes platelet aggregation. Excessive coagulation causes thrombosis, resulting in risks of stroke, heart attack, and serious breathing problems. Relatedly, P12 is a 14 amino acid peptide isolated from fibronectin, an ECM protein involved in tissue repair, that holds much promise in its use with biomaterials and clinical applications for thrombosis prevention: prior research indicates that P12 may help prevent blood clot formation *in vitro*² by preventing the α C domain connections between protofibrils. For instance, it could improve the efficacy of current stent technology, which currently holds severe risks of stent thrombosis³. Thus, the use of an improved stent coating, which won't limit cell growth, is necessary. Consequently, the present study seeks to evaluate the effect of P12 on fiber formation on hydrophobic polystyrene (PS) surfaces and its toxicity on fibroblasts.

To analyze P12's ability to prevent fiber formation under staggered thrombin and P12 application, 4mg/ml of fibrinogen was placed in solution in tubes. One tube was treated with 2 units/L of thrombin and 30 seconds later, 50mM of P12. The other was treated with P12, and 5 minutes later, thrombin. Solutions were then deposited on films and imaged with Atomic Force Microscopy (AFM).

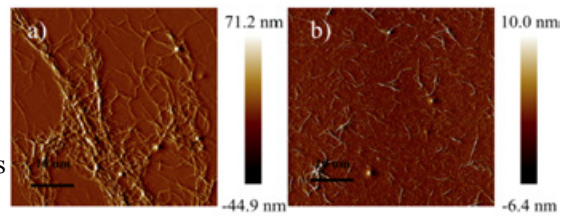
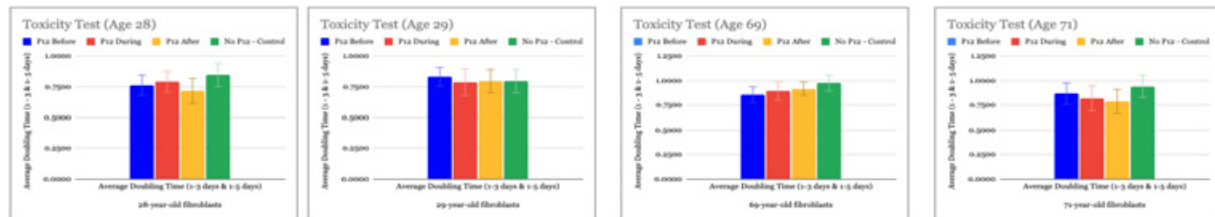


Figure 1. Atomic Force Microscopy. (a) Thrombin applied first (b) P12 applied first

As shown in Figure 1B, AFM demonstrated P12's effectiveness in inhibiting fibrin fiber formation. When P12 was applied before thrombin, large fibers were not able to form from branched, smaller fibers, resulting in the deposition of scattered, disconnected fibrils on the thin-film surface, likely due to P12 adsorption preventing alpha-domain connections between protofibrils. In figure 1A, P12 was ineffective when added post-thrombin incubation when the fibrinogen cleavage and fibrin polymerization already occurred in solution.

Fibroblasts were also cultured in DMEM in 12-well plates to analyze P12's toxicity. P12 was applied either before (100 μ M P12 in 1 mL PBS was used to coat wells), during (50 μ M P12 was added during plating), or after the first media change of the wells (10 μ M P12 was added during the first media change). 10 μ M P12 was added to each experimental well during each subsequent media change. Ultimately, doubling time, plating efficiency, and cytotoxicity were analyzed through immunofluorescence.



By applying a two-tailed t-test, we found that no significant difference ($p > 0.05$) in doubling time between fibroblast groups with or without P12 (control) exists; thus, P12 does not inhibit cell growth and has no toxic effect on cells. This is further supported by plating efficiency data: compared to cells grown on PS thin-films, cells grown with P12 generally had higher plating efficiencies.

Future research should investigate deposition of fibers when using blood containing fibrinogen and thrombin at normal levels. Murine models may also be useful to determine if P12-coated stents have better endothelialization and survival than current alternatives.

¹ Kattula, S., Byrnes, J. R., & Wolberg, A. S. (2017). Fibrinogen and fibrin in hemostasis and thrombosis. *Arteriosclerosis, Thrombosis, and Vascular Biology*, 37(3). <https://doi.org/10.1161/atvbaha.117.308564>

² Doilidova, A., El-Saieha, S., Fariaa, S., & Loa, P. The Effect of P12 Peptide on Fibrinogen Fiber Formation and Endothelial Cell Attachment on Polystyrene.

³ Coombes K, Molina G, Contreras R, Jacobson A, Jarrett R. An Uncommon Case of Acute Coronary Stent Thrombosis. *Cureus*. 2023 Jan 16;15(1):e33834. doi: 10.7759/cureus.33834. PMID: 36651555; PMCID: PMC9842189.

Convolutional Autoencoder and Extended Dynamic Mode Decomposition for Koopman Operator-based Markov Chaining for Time Series Forecasting of a Large-Scale Dissipative Particle Dynamics System for Thrombosis Modelling

Akhil Samavedam¹, Yicong Zhu², Yuefan Deng²

¹Westlake High School, Austin, TX, 78746

²Department of Applied Mathematics and Statistics, Stony Brook University, Stony Brook, NY 11794

Cardiovascular Disease (CVD), is the single largest cause of death in the world, with an annual death toll in excess of 17.9 million¹. The majority of CVD deaths are caused by thrombosis, the formation of a thrombus—a blood clot—in a vein or artery that impedes the

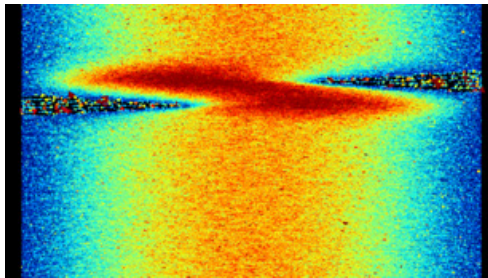


Fig 1. Velocity Field of Thrombosis System

circulatory system. It is therefore necessary to develop computational models for thrombosis in order to understand the mechanics and simulate the process of blood clotting. However, current simulations of thrombosis are extremely computationally intensive and time consuming. The hybridization of continuum methods such as Computational Fluid Dynamics (CFD) and discrete methods such as Coarse-Grained Molecular Dynamics (CGMD) have decreased the time to simulate a millisecond of thrombosis from 3.7 years to 3 days²; however, this speedup is insufficient to model clotting at timescales of days or weeks.

We perform time series forecasting using an approximated Koopman Operator (aKO)³ calculated by Extended Dynamic Mode Decomposition

(EDMD), to form a Markov Chain. aKO converts the nonlinear state space into a linear vector space where multiplying the current state representation by aKO predicts the future state representation. EDMD finds aKO through

the product of a matrix of observable functions and the Moore-Penrose pseudoinverse of time shifted functions. The state tensor that represents the system in discrete time is a high

dimensional construct with over 3 million elements and therefore unusable as an observable function vector. Hence, a Convolutional Autoencoder (CAE) is implemented to learn encodings and decodings to represent the large state tensor as a 256-element latent vector.

These latent vectors encode critical spatiotemporal information about the state of the dynamic system and are therefore usable as observable functions. To forecast the time series, an initial state tensor is encoded as a latent vector, then multiplied by aKO to obtain the latent vector in the future. This latent vector can again be multiplied by aKO to predict

the following time step and can also be decoded by CAE to obtain the next state tensor, creating a Markov Chain as the process is repeated. CAE-EDMD predicts jumps of 5000 time steps of normal simulation in just 300 milliseconds with over 96% accurate Markov analysis for state tensor prediction (with decoding) and 99% for latent vector prediction, allowing for the rapid time series forecasting of thrombosis.

¹Yicong Zhu, Changnian Han, Peng Zhang, Guojing Cong, James R. Kozloski, Chih-Chieh Yang, Leili Zhang, Yuefan Deng, AI-aided multiscale modeling of physiologically-significant blood clots, *Computer Physics Communications*, Volume 287, 2023, 108718, ISSN 0010-4655, <https://doi.org/10.1016/j.cpc.2023.108718>

²Han, C., Zhang, P., Zhu, Y. et al. Scalable multiscale modeling of platelets with 100 million particles. *J Supercomput* 78, 19707–19724 (2022). <https://doi.org/10.1007/s11227-022-04648-4>

³B.O. Koopman, Hamiltonian systems and transformation in Hilbert space, *Proceedings of the National Academy of Sciences of the United States of America*. 17 (1931) 315. <https://doi.org/10.1073/pnas.17.5.315>

⁴Geneva, N. (2020). The common neural networks encoder/decoder structure for learning Koopman observables. *Intro to Deep Learning Koopman Operators*. Retrieved July 28, 2023, from <https://nicholasgeneva.com/deep-learning/koopman/dynamics/2020/05/30/intro-to-koopman.html>.

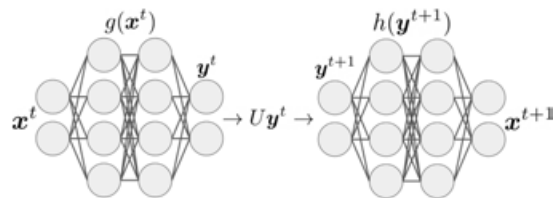


Fig 2. Illustration of the neural network architecture used for learning Koopman observables, adapted from Geneva (2020)⁴.

State tensor at time t x^t is encoded into latent vector y^t then multiplied by Koopman Operator U to produce vector at $t+1$ y^{t+1} and decoded to x^{t+1}

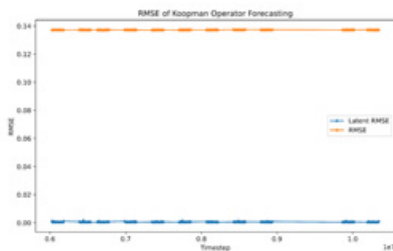
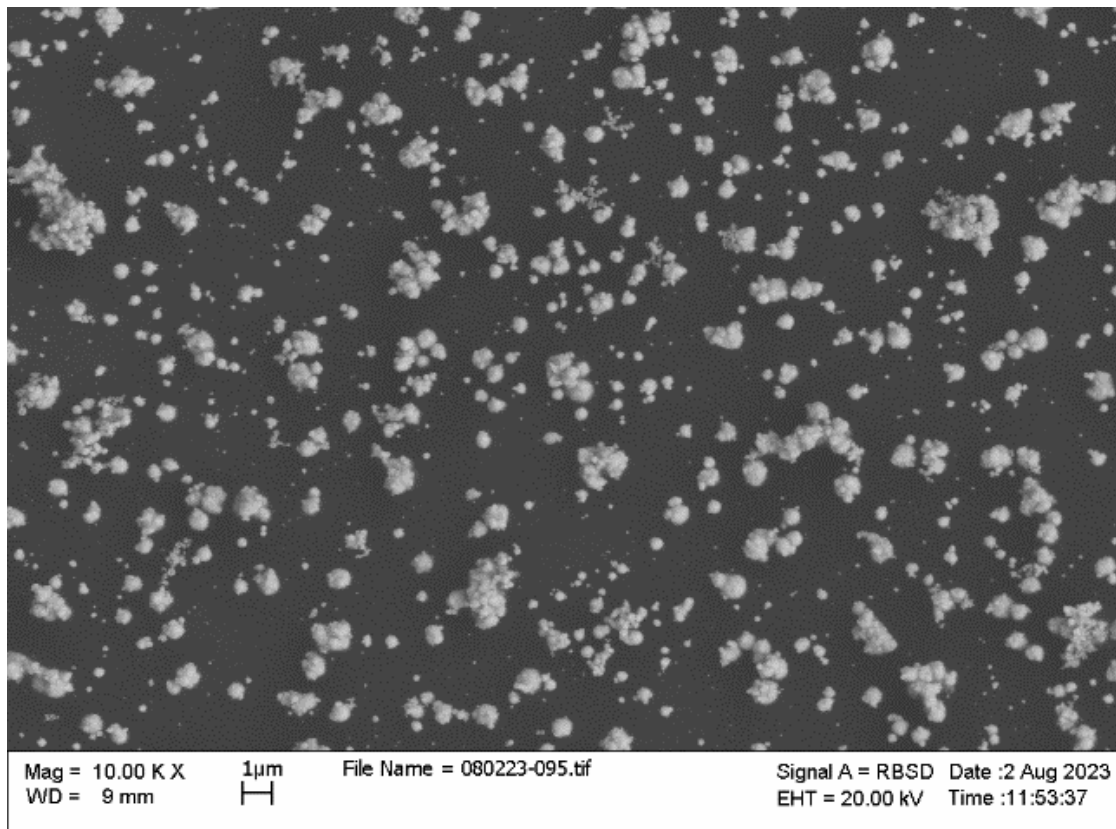


Fig. 3 Error of Latent Vector and State Tensor Prediction

Session 8: Deweaved Cellulose Scaffolds

Chairs: Michael Cuiffo



Synthesizing Gold Nanoparticles on Chitosan-Coated Stainless Steel

Daniel Lu¹, Claire Kang², Harjaisal Brar³, Jacob Zerykier⁴, Gary Halada⁵, Michael Cuiffo⁵

¹Westview High School, San Diego, CA 92129; ²Canyon Crest Academy, San Diego, CA 92130; ³Stockdale High School, Bakersfield, CA 93311; ⁴Massachusetts Institute of Technology, Cambridge, MA 02139; ⁵Department of Materials Science and Chemical Engineering, Stony Brook University, Stony Brook, NY, 11790

Previously, palladium and other noble metal nanoparticles have been synthesized on chitosan-coated stainless steel^{[1][2]}. These metal nanoparticles have been shown to have both antibacterial and catalytic properties. For this reason, discovering ways to synthesize more classes of metal nanoparticles is important.

1 μ m mirror finish 304 stainless steel purchased from McMaster-Carr was cut into one square inch samples (2.54 cm²). The steel samples were ultrasonicated in isopropyl alcohol for 10 minutes, briefly rinsed, and ultrasonicated for another 10 minutes in deionized (DI) water to remove greases and other contaminants. The steel samples were then allowed to air dry and prepared for electrochemical deposition.

A chitosan solution with a concentration of 1.00 to 3.00 grams of chitosan per 120 mL DI water was prepared, and the pH was lowered to less than 5 by adding HCl dropwise to the solution. The solution was stirred overnight so that the chitosan could fully dissolve. A potassium gold (III) chloride solution with a concentration of 0.01 M was prepared in a volumetric flask using high purity (>18m Ω /cm) DI water.

The steel samples were electrochemically coated with a layer of chitosan using controlled potential coulometry. A constant potential of -3.0 V was applied for 60-120 seconds. Each sample was air dried overnight. The chitosan-coated steel samples were used for electrochemical reduction of the gold (III) ions to synthesize nanoparticles on the chitosan layer at voltages ranging from -1.5 to +1.5 for 60-120 seconds in order to determine the optimized parameters for gold nanoparticle synthesis. Once the process was complete, the samples were air dried overnight or placed in a vacuum chamber for several hours.

Various methods of analysis were employed to image and quantify the nanoparticles including Optical Microscopy, Scanning Electron Microscopy (SEM), and X-Ray Fluorescence (XRF). Figure 1 shows an SEM image of the gold nanoparticles.

Future work will include X-Ray Photoelectron Spectroscopy (XPS) to determine the oxidation states of the nanoparticles and more experimentation with concentrations and voltages to optimize the parameters for electrochemistry.

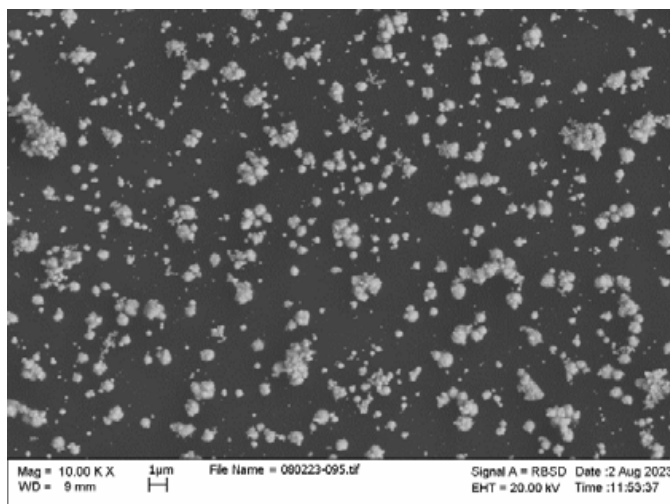


Figure 1: A SEM image of the Gold NPs on the chitosan matrix.

[1] M. Cuiffo, P. K. Jha, G. P. Halada, "Novel Synthesis Route for Palladium Nanoparticles," Patent #9,932,685, April 3, 2018.

[2] Halada, Gary P., et al. "An Environmentally-Benign Electrochemical Method for Formation of a Chitosan-Based Coating on Stainless Steel as a Substrate for Deposition of Noble Metal Nanoparticles." *Ceramic Transactions Series*, John Wiley & Sons, Inc., 1 July 2013, pp. 229–238. Crossref, doi:10.1002/9781118744109.ch25.

Characterizing Adhesive Complex Formed With Deweaved Cotton Fibers and Chitosan Solution

Claire Kang¹, Harjaisal Brar², Daniel Lu³, Jacob Zerykier⁴, Gary Halada⁵, Michael Cuiffo⁵

¹Canyon Crest Academy, San Diego, CA 92130; ²Stockdale High School, Bakersfield, CA 93311; ³Westview High School, San Diego, CA 92129; ⁴Massachusetts Institute of Technology, Cambridge, MA 02139; ⁵Department of Materials Science and Chemical Engineering, Stony Brook University, Stony Brook, NY, 11790

Adhesives serve numerous roles, including producing plywood, packaging, and sealing insulation^[1]. For this reason, it is essential that lower cost and more environmentally friendly options are produced to replace the many toxic materials that are currently used.

In this study, an adhesive matrix was formed with cotton fibers and chitosan solution. Samples of tailored Muslin fabric were deweaved in 0.5 M citric acid solution for 15 minutes, then were added to and dispersed in a chitosan solution. The mixtures were left to dry and/or cured under UV light for up to an hour. It was discovered that the mixture produces a substance that hardens into a thin film when pressure is applied.

This material was analyzed using Differential Scanning Calorimetry (DSC), Thermogravimetric Analysis (TGA), and Fourier-Transform Infrared Spectroscopy (FTIR). Figure 1 shows the DSC results for a sample, showing a glass transition temperature of 145°C, a crystallization temperature of 184°C, and a boiling point of the matrix of 234 °C. Figure 2 shows the TGA plot of another sample. The TGA plot shows the boiling point is around 215°C. This discrepancy may be due to the fact that the samples were not homogenous, since the cotton fibers were inconsistently distributed throughout the material.

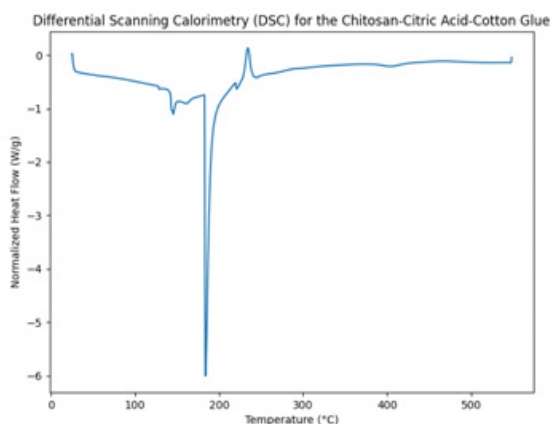


Figure 1: DSC analysis graph for the chitosan-citric acid-cotton glue, produced using Matplotlib.

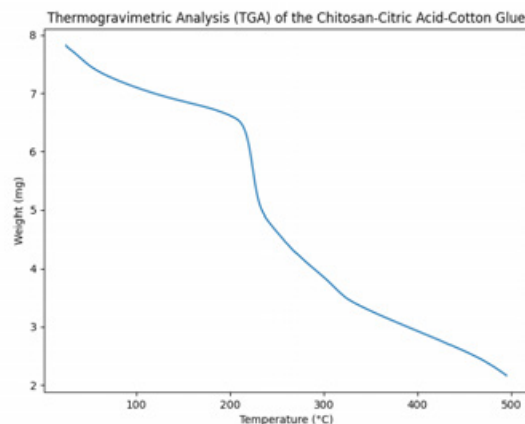


Figure 2: TGA analysis for the chitosan-citric acid-cotton glue, produced using Matplotlib.

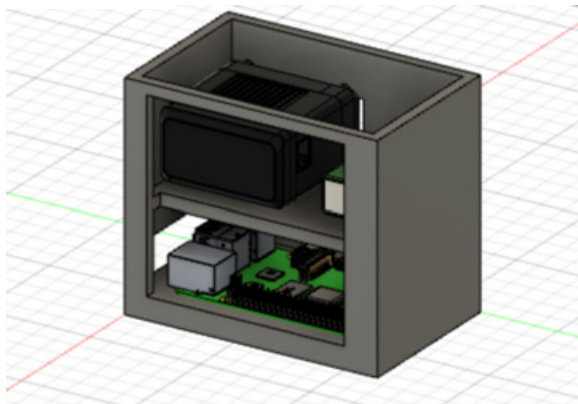
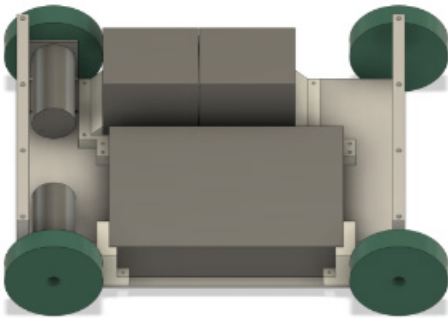
The FTIR results possessed a characteristic peak at 1700 cm⁻¹, indicating chitosan crosslinking as a result of reacting with citric acid^[2]. This suggests that the citric acid likely plays a key role in the adhesive properties of this material by crosslinking chitosan. Future experimentation will be done to assess more material properties, such as tensile strength testing and flame resistance.

[1] Dinte, Elena and Bianca Sylvester. "Adhesives: Applications and Recent Advances." *Applied Adhesive Bonding in Science and Technology*, InTech, 21 Feb. 2018. Crossref, doi:10.5772/intechopen.71854.

[2] Ponnusamy, Prabakaran Graceraj, et al. "Preparation and Characterization of Citric Acid Crosslinked Chitosan-Cellulose Nanofibrils Composite Films for Packaging Applications." *Journal of Applied Polymer Science*, 2022. Crossref, doi:10.1002/app.52017.

Session 9: 3-D Printing and Materials Design

Chairs: Yu-Chung Lin,
Aaron Sloutski,
Robert Wong, Aditya
Patankar



Designing a Mobile Base for a Mobile Manipulator

Dr. Nilanjan Chakraborty¹, Dasharadhan Mahalingam², Peter Elmer³, Eleanor Yang⁴

¹Assistant Professor at Stony Brook University, Stony Brook, NY 11794; ²Graduate Student at Stony Brook University, Stony Brook, NY 11794; ³High School for Math, Science and Engineering, New York, NY 10031; ⁴Evergreen Valley High School, San Jose, CA 95148

Additive manufacturing (AM), more commonly known as 3D printing, allows for increased freedom in designing parts that are used in different applications in the many fields of engineering, especially in robotics¹. Computer-aided design (CAD) is the first and most important step of the 3D printing process. This is the step in which models are designed and visualized, and later revised and refined, using CAD softwares. These models can be converted into .stl files, sliced (made into layers), and converted to a .gcode file to be printed by a 3D printer².



Fig. 1. Franka Emika Panda Robotic Arm

Using CAD, this research aims to 3D-model a mobile base for the Franka Emika Panda robot arm (Fig. 1). A mobile base would allow for an easier way to relocate the Franka Emika Panda robot arm and move it around homes and hospitals to complete tasks more efficiently without the hassle of removing and attaching the arm to a stationary surface. This mobile base was mainly designed using the CAD softwares SOLIDWORKS and Fusion360.

This research considered the given requirements of materials and the constraints of the size of the base. There were several specifications that needed to be followed in order to build this base. It needed to be able to hold two 12V SLA (sealed lead-acid) batteries, have two motors directly driven to two wheels, and most importantly, it needed

to be able to stay upright despite any large movements from the robotic arm. Aluminum supports were used as a frame for the chassis to support the weight of everything we needed. Using SOLIDWORKS and Fusion360, several models for the base were designed with different arrangements of the parts to visualize what we were working with. Given the dimensions and weight of different segments of the Franka Emika Panda robot arm and using tip-over stability, we were able to calculate the necessary dimensions needed for the base so that it would not tip over when the arm is fully extended, but would still be small enough to move through doorways and other tight spaces³. Motors, batteries, and wheels were then selected based on the desired power, speed, and battery life. A final design of the mobile base was then created using Fusion360 (Fig. 2).

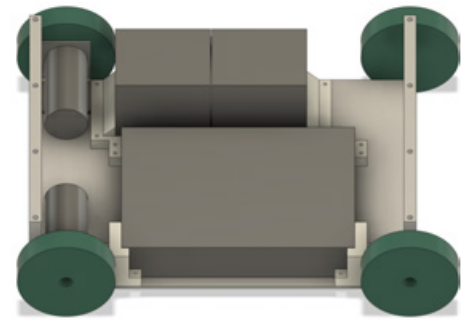


Fig. 2. Final CAD design of mobile base (side view, without top panel)

Since this project can always be improved, we are looking at potential modifications such as creating a circular base for easier navigation around homes and hospitals, using omni-directional wheels to allow the base to move sideways without needing to turn, and adding sensors to minimize collisions that could cause the base to tip over.

¹ Delda, Ray Noel Medina, et al. “3D Printing Polymeric Materials for Robots with Embedded Systems.” *Technologies*, vol. 9, no. 4, Nov. 2021, p. 82. *Crossref*, <https://doi.org/10.3390/technologies9040082>.

² Mikolajczyk, Tadeusz, et al. “CAD CAM System for Manufacturing Innovative Hybrid Design Using 3D Printing.” *Procedia Manufacturing*, vol. 32, 2019, pp. 22–28, <https://doi.org/10.1016/j.promfg.2019.02.178>.

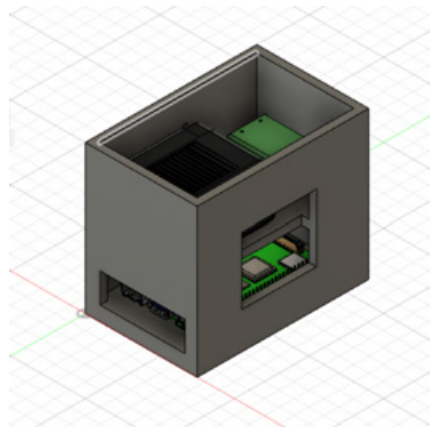
³ “Franka Erika Robot’s Instruction Handbook.” *generationrobots.com*, Oct. 2021, <https://generationrobots.com/media/franka-emika-robot-handbook.pdf>. Accessed 19 July 2023.

A Cross-Platform Transfer

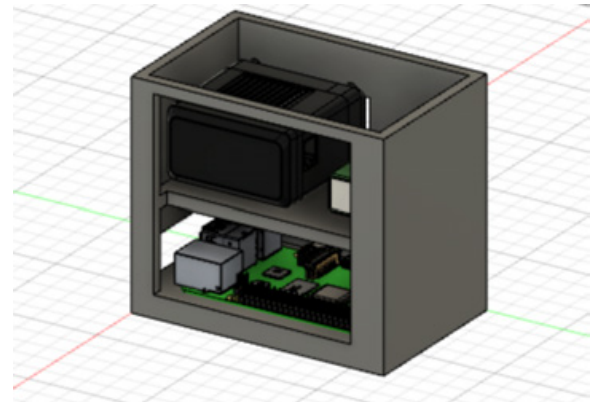
Alex Samadi¹, Junior Gonzalez², Arianna Rolland³

¹Virginia Polytechnic Institute and State University, Blacksburg, Virginia ; ²Suffolk County Community College, Selden, New York; ³Patchogue Medford High School, Medford, New York

Many people who are paralyzed rely on using an electric wheelchair to get from place to place. Quadriplegia occurs after a neck or spinal injury and is a form of paralysis where all four limbs are paralyzed. As people with quadriplegia are unable to move their limbs, they are dependent on their wheelchair and have a restricted range of vision. With this being a major issue, we set out to create a solution, and decided to use a telecommunication device and rotating cameras. We created a program that would be able to control these movements based on words spoken into a microphone, which would then be visible on a display. As the user states words such as “right”, “left” or “center”, the camera would move accordingly. This system consists of a raspberry pi, a camera, a servo, a nine volt battery, a monitor, a fan, and a 3D printed mount. The raspberry pi would be the intelligence of the system, the camera would be mounted onto the servo, the servo would turn dependent on the input from the raspberry pi, the nine volt battery would power the fan which prevents the system from overheating, the monitor would display what the camera sees, and finally the 3D printed mount would be used to grasp everything and connect it to the wheelchair. In most cases, this camera system could be mounted on the upper back part of an electric wheelchair. This allows the user to see both behind and on the sides of the wheelchair simply by saying “right”, “left”, or “center”.



As shown in the figures, a raspberry pi is the backbone of the configuration. It houses a user interface - a voice recognition with an interpreting system to understand voice inputs. Once the raspberry pi interprets voice inputs, it would transmit a signal to the servo which would be



mounted above the raspberry pi and turn the motor 90 degrees in the respective direction. In sum, as this system would be applied to an electric wheelchair, there would be a monitor mounted on one of the armrests that would display what the camera sees and three buttons which could be used with a speech recognition program to move the camera from side to side. The camera would then be clamped on the back of the wheelchair to make places visible that were not before. As this project can always be improved, we are working on adding another camera mounted on a second servo strictly for the range of up and down, which would complete the range of vision for the user. We are also looking to expand our project to further improve the quality of lives for quadriplegics by re-engineering other devices such as a tongue touch keypad.

[1] Suman K. Saksamudre, P.P. Shrishrimal, R.R. Deshmukh. “A Review on Different Approaches for Speech Recognition System”

[2] Hangue Park and Maysam Ghovanloo. “An Arch-Shaped Intraoral Tongue Drive System with Built-in Tongue-Computer Interfacing SoC” 2014

[3] Hui Tang and D.J. Beebe. “An oral tactile interface for blind navigation” 2006

Robotic Vision: 3D Object Orientation Detection Algorithms

Brandon Cai¹, Aditya Patankar², Nilanjan Chakraborty²

¹Parkland High School, Allentown, PA 18104; ²Stony Brook University, Stony Brook, NY 11790

The goal of this project is to create a robust object orientation detection algorithm from the point cloud obtained by an Intel RealSense 3D camera. The determined orientation can help a robot to grasp that object and rotate it. In robotic vision, each object detected is marked with a bounding box, a rectangular prism that surrounds an object to provide dimension. The most basic bounding box is the axis aligned bounding box, which simply calculates the minimum and maximum x -, y -, and z -coordinates of all the points to create a bounding box with edges parallel to the axes even if the object is not aligned with the coordinate axes. Principal Component Analysis (PCA) uses the covariance matrix of the point cloud by calculating the variance and covariance in the x and y directions to determine the orientation of an Oriented Bounding Box (OBB). Because the objects are on a table, we can simply project the point cloud down to the xy plane and calculate the 2D PCA bounding box before adding the height for the final OBB. However, this method is can be fooled as every point in the cloud carries the same weight in orientating, resulting in misalignment.

To determine the best fitting bounding box, the Rotating Calipers algorithm is used. This algorithm is guaranteed to return the minimum area bounding box. First, the convex hull of the point cloud is calculated. The convex hull is a polygon containing some points of the cloud as vertices such that all of the other points are inside it. We can thus ignore all of the points inside the convex hull when calculating the optimal bounding box as they do not affect the bounding box of the convex hull. Now, for every edge of the convex hull, we rotate the hull such that that edge is parallel to one of the axes and calculate the axis aligned bounding box. After doing this for all of the edges, we pick the one with the minimum area and extend the 2D bounding box vertically to get a 3D Oriented Bounding Box parallel to the table.

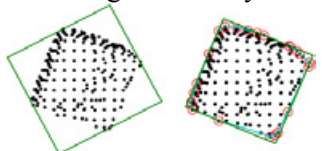


Figure 2: Left – PCA Bounding Box, Right – Optimal Bounding Box from Rotating Calipers

Compared to PCA this algorithm decreased average bounding box area by 12% and increased overhead computation time by 46% for the 26 point clouds.

Another achievement made in this project is to preprocess the point cloud entry to filter out erroneous points that are not part of the object. In many clouds, the table level points are not all filtered out, leaving a tail of points that are just outside of the object's "shadow" from the camera's perspective. These significantly increase the bounding box area and cause wrong orientation. Density Based Clustering detects clusters of points within a specified distance of its neighbors. The goal is to create two clusters: the object and the shadow. Picking the cluster with more points, the object is isolated from the shadow. Tuning the parameters gives an effective noise removal algorithm, filtering out the noise in all point clouds that have it with an average 37% decrease in bounding box area. Overall, a more robust and accurate object orientation algorithm was developed for effective robotic manipulation.

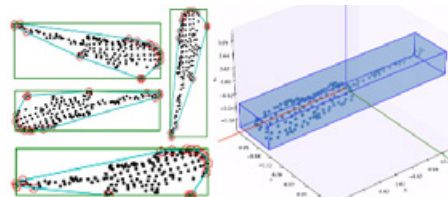


Figure 1: Left – Screwdriver rotated to find optimal bounding, Right – Oriented Bounding

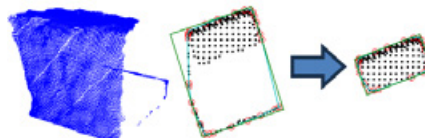


Figure 3: Left to Right – 3D Point Cloud with Noise, Raw Point Cloud Bounding Box, Bounding Box with Noise Removal.

[1] D. S. Arnon and J. P. Gieselman, "A Linear Time Algorithm for the Minimum Area Rectangle Enclosing a Convex Polygon," Purdue University, Department of Computer Science, Tech. Rep., 1983.

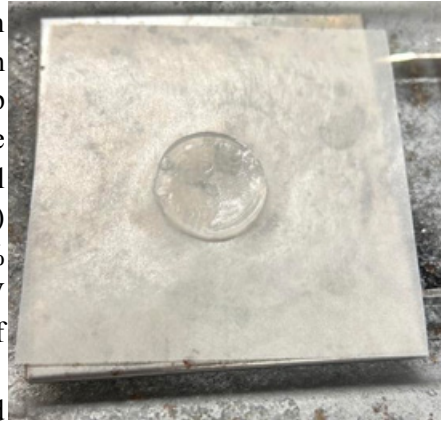
[2] Chang, C.-I., Gorissen, B., and Melchior, S. 2011. Fast Oriented Bounding Box Optimization on the Rotation Group $SO(3, \mathbb{R})$. ACM Trans. Graph. 30, 5, Article 122 (October 2011).

Bioprinting Hydrogels for Dentin Regeneration and Disinfection

Saranya Anantapantula¹, Abdel Mahmoud², Aaron Sloutski³, Kuan-Che Feng³, Miriam Rafailovich³

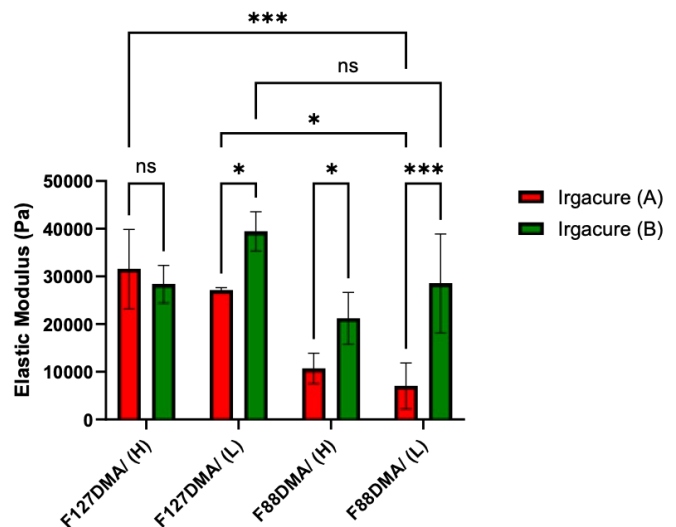
¹Spring-Ford Area High School, PA 19468, ²Stony Brook School of Dental Medicine, NY 11790, ³Department of Materials Science and Engineering, Stony Brook University, NY 11790 USA

Oral and maxillofacial complications pose challenges due to issues like lack of material biocompatibility and invasive treatments¹. One common example is the endodontic treatment, where the infected pulp is removed. This process can leave the tooth brittle in the long-term². Moreover, additive manufacturing or 3D bioprinting can result in the development of hydrogels that can regenerate lost dentin pulp, restoring tooth strength and longevity. This research aimed to identify a hydrogel that can deliver antibiotics or induce stem cell differentiation for dentin pulp regeneration while maintaining durability. We modified three variables to determine the most effective hydrogel: structural material (F127 DMA or F88 DMA), the crosslinking agent (Irgacure 651 (A) or Irgacure 2959 (B)), and the photoinitiator concentration (2.4% (high) or 0.24% (low)). The crosslinking agent is activated by UV light with one minute on each side, resulting in the formation of polymer networks.



In the experiment, solutions of F127 and F88 were prepared with a 20% concentration in a phosphate buffer solution. Subsequently, two photoinitiators (A and B) were added at concentrations of 2.4% and 0.24%. As a result, we had 8 samples with combinations of these materials. Hydrogels were then formed using a 22mm-diameter silicon mold and exposed to UV light for crosslinking, after which they were stored in DI water. Rheology was conducted on the samples to understand how stiff the samples were.

Measurements taken aimed to assess the swelling ratio (water retention capability), elastic modulus (material stiffness), and cross-linking efficiency. The data collected showed that F88 had a higher swelling ratio than F127. Elastic modulus measurements confirmed that F127 was inherently stronger, and its cross-linking efficiency was superior due to its lower swelling ratio. In conclusion, while F127's stiffness and effective crosslinking make it a promising candidate, further research is required to assess the biocompatibility of photoinitiators and their concentrations in terms of cell viability. Thus, further studies will be conducted on the hydrogel's bioprintability, cell viability, cytotoxicity, and osteogenic differentiation or the ability of stem cells to differentiate into bone cells. The final gel has multiple potential endodontic applications: it could be placed on the top of the pulp cavity to induce dentin regeneration or disinfect the canal area. Thus, these bioprintable hydrogels will ultimately pave the way for healthier teeth.



¹ Huang, Mingshu, et al. "Hydrogels for Treatment of Oral and Maxillofacial Diseases: Current Research, Challenge, and Future Directions." *Biomaterials Science* (2022).

² Yan, Weishi, et al. "Contribution of Root Canal Treatment to the Fracture Resistance of Dentin." *Journal of Endodontics*, vol. 45, no. 2, Feb. 2019, pp. 189–93. DOI.org (Crossref), <https://doi.org/10.1016/j.joen.2018.10.004>.

Mechanical Property and Cell-Adhesion Characterization of Poly(vinyl alcohol) and Resorcinol Diphenyl Phosphate Clay Blend Hydrogels

Hannah Oh¹, Leora Stochel², Haoyu Xu³, Megha Gopal⁴, Robert Wong⁵, Aaron Sloutski⁵, Adam Hansen⁵, Reza Dashti⁶, Chander Sadasivan⁶, Miriam Rafailovich⁵

¹Chadwick International School, Yeonsu-gu, Incheon, South Korea 22002, ²Hebrew Academy of Nassau County, Uniondale, NY 11553, ³Hangzhou Foreign Languages School, Hangzhou, Zhejiang, China 310023, ⁴Department of Biomedical Engineering, Stony Brook University, Stony Brook, NY 11794, ⁵Department of Materials Science and Chemical Engineering, Stony Brook University, Stony Brook, NY 11794, ⁶Department of Neurological Surgery, Stony Brook University Medical Center, Stony Brook, NY 11794

The development of synthetic small-scale vascular grafts is critical as their anastomosis into animal models allows for experimental evaluations of medical devices. Current vascular models, however, are fallible to hyperplasia, thrombosis, and occlusion.¹ One promising material is Poly(vinyl alcohol) (PVA), a water-soluble polymer capable of cross-linking into a hydrogel. It has been shown to be hemocompatible, biocompatible, elastic, and resistant to stress, showing adequate vascular performance under arterial pressure when tested in vivo in rats.² However, the bioinert nature of PVA imparts a low propensity for cellular adhesion. This research investigates the effect of Resorcinol Diphenyl Phosphate (RDP) clay, a phosphate ester flame retardant which has been proven to increase cell adhesion when added to PVA thin films, on the mechanical and cell-adhesive properties of PVA-based hydrogels.³

To make the hydrogels, solutions of 10% PVA (w/w) were prepared with RDP-clay concentrations of 0%, 1%, 5%, and 10%. After cross-linking with 15% Sodium Trimetaphosphate (STMP) solution and 30% NaOH solution, hydrogel solution was added to individual wells of a 6-well plate and allowed to dry overnight. Following complete desiccation of the discs, they were sterilized under UV light for 30 minutes on each side. After rehydration in media, the discs were cut into squares and placed in 12-well plates coated with 2% agarose. Human Umbilical Vein Endothelial Cells Expressing Green Fluorescent Protein (HUVEC-EGFP) were plated on the squares at a density of 2,000 cells/cm². After five days in the incubator, cells were fixed with formaldehyde and viewed under the EVOS-M7000 microscope with DAPI staining. Discs not used for cell plating were rehydrated and cut into square films, and their wall thicknesses were confirmed to fall within manufactured tubular geometry thicknesses with Keyence microscope.

To create tubular geometries, cylindrical wax rods with 2mm diameter were dipped in the prepared PVA/RDP solutions 10 times and allowed to spin-dry on a monoaxial spinner for a fixed interval. To investigate the effect of spin-drying time on the thickness of the vessels, three vessels of 10% PVA were spin-dried at 15, 18, 20 minute intervals. The wall thickness of each vessel was determined by cutting the vessel perpendicular to its length to expose the cross-section of the tube and measuring the thickness using the Keyence microscope.

No HUVEC-EGFP cell growth was observed on any RDP concentration, with minimal growth found on the 0% RDP group, which signifies an issue with the processing of the PVA discs. It is likely that the pH of the disc surface was too basic for cell culture due to inadequate washing of the NaOH crosslinker. When viewed under the EVOS-M7000, RDP-clay in the PVA hydrogel displayed both blue and green fluorescence, shown in Fig. 1, which can also make it difficult to view cells.

Furthermore, it was found that generally, increasing spin-drying time corresponded to increased manufactured vessel wall thickness. As seen in Fig. 2.A, the average thickness of the 15-minute interval vessels corresponds to that of human vasculature (200-300 μm)⁴ and are thinner than its 20 minute drying counterpart (Fig 2.B). The 18-minute interval vessels, however, unexpectedly display decreased thickness relative to the vessels of the other time intervals. This inconsistency can be attributed to the usage of faulty wax rods and also suggests the importance of controlling the casting process, as vessel thickness seems to be influenced by variables such as drying conditions, dipping time and the viscosity of the solution.

This study posits dip-casting as an effective and successful means of manufacturing PVA vessels and continues to show promise for cell adhesion with alternative hydrogel processing. Further directions include refining the vessel manufacturing process by reducing and unifying dip-coating duration and developing a thorough washing protocol to remove excess NaOH from the hydrogel matrix.

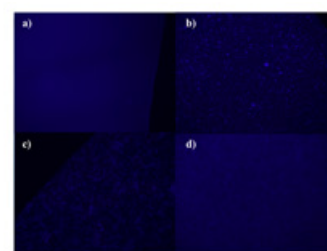


Fig 1: The fluorescence of RDP clay under EVOS microscope (concentration of RDP clay: a=0%, b=1%, c=5%, d=10%)

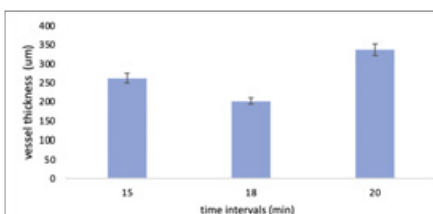


Figure 2.A: effect of spin-drying time on average vessel

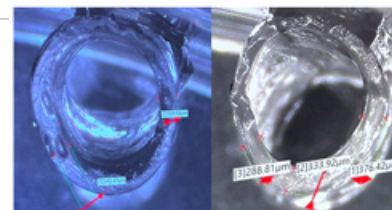


Figure 2.B: Vessels under Keyence Microscope (Left: 15 min drying interval, right: 20 min drying interval)

¹Táborská, J., et al. (2021, February 3). "Endothelialization of an eptfe vessel prosthesis modified with an antithrombogenic fibrin/heparin coating enriched with bound growth factors." RSC Advances.

²Chaouat, Marc, et al. "A novel cross-linked poly (vinyl alcohol)(PVA) for vascular grafts." Advanced Functional Materials 18.19 (2008): 2855-2861.

³Feng K-C, et al. Investigating the Effects of Different Spun-Cast and Molded Polylactic Acid (PLA) and Polystyrene (PS) Composites on the Proliferation, Differentiation and Biomaterialization of Dental Pulp Stem Cells. Materials Research Society Fall Meeting; 2018 Nov 25-30; Boston, USA.

⁴Mandell, D M, et al. "Intracranial Vessel Wall MRI: Principles and Expert Consensus Recommendations of the American Society of Neuroradiology." AJNR. American Journal of Neuroradiology, Feb. 2017.

Xuyi Zhou¹, Yu-Chung Lin², Miriam Rafailovich²¹ Shanghai Pinghe School, Shanghai, 201206 ² Department of Material Science and Engineering, Stony Brook University, NY, 11794

The electronic industry has considerable demand for materials with good electrical and thermal conductivity, and for the convenience of manufacturing, it would be beneficial for the materials to have better mechanical properties in comparison to the currently actively researched material graphene. In response to such need, we intend to engineer nanocomposites with a blend of PLA, PBAT, and GNPs H-5 through 3D printing in this research. From the properties of individual materials, PLA is the currently commercialized 3D printing filament material; PBAT, as a ductile polymer, compensates for the brittleness of graphene; GNPs H-5 has greater surface contact between particles compared to GC750, contributes to good electrical and thermal conductivity. From previous studies, it had been concluded that the optimal ratio of PLA to PBAT is 1:3, considering electrical conductivity, thermal conductivity, and mechanical properties[1]. Contact angle tests and work of adhesion calculation indicated that GNPs preferred the phase of PBAT as opposed to PLA. The addition of PLA, at low concentration, would take up space and confine GNPs in PBAT, therefore improving electrical and thermal conductivity. Nevertheless, more PLA has the risk of making PBAT phase discontinuous. Inspired by this, in our research, we altered the concentration of GNPs (including 8%, 12%, 16%, and 20%) to find the composites with optimal thermal conductivity, electrical conductivity, and mechanical properties. The ratio of PLA to PBAT is fixed as 1:3. The 3D printing nozzle shear force is expected to further orientate the H-5 platelets.

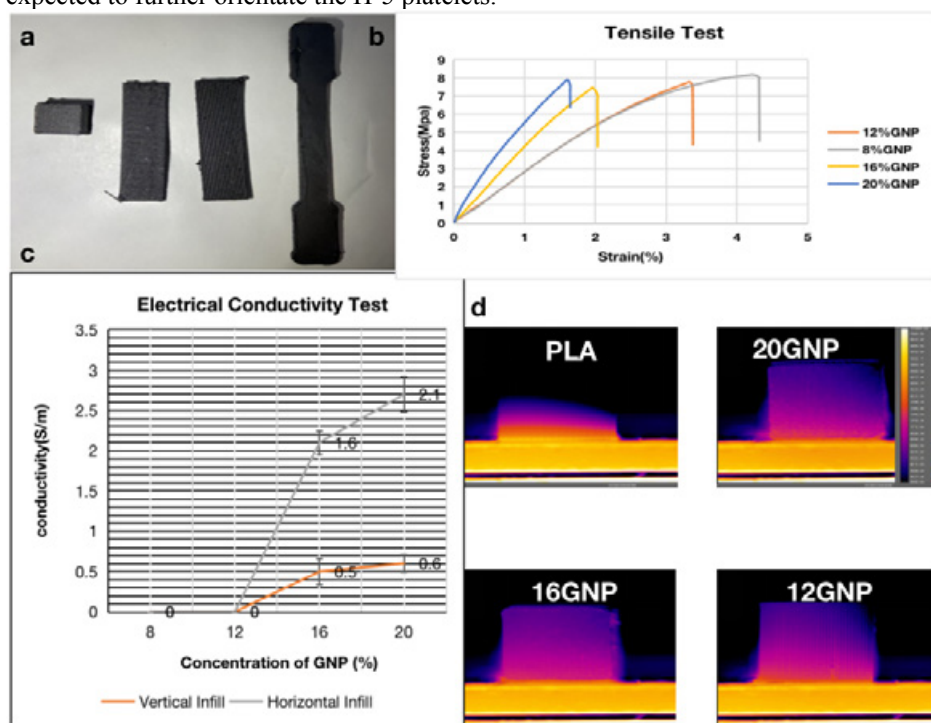


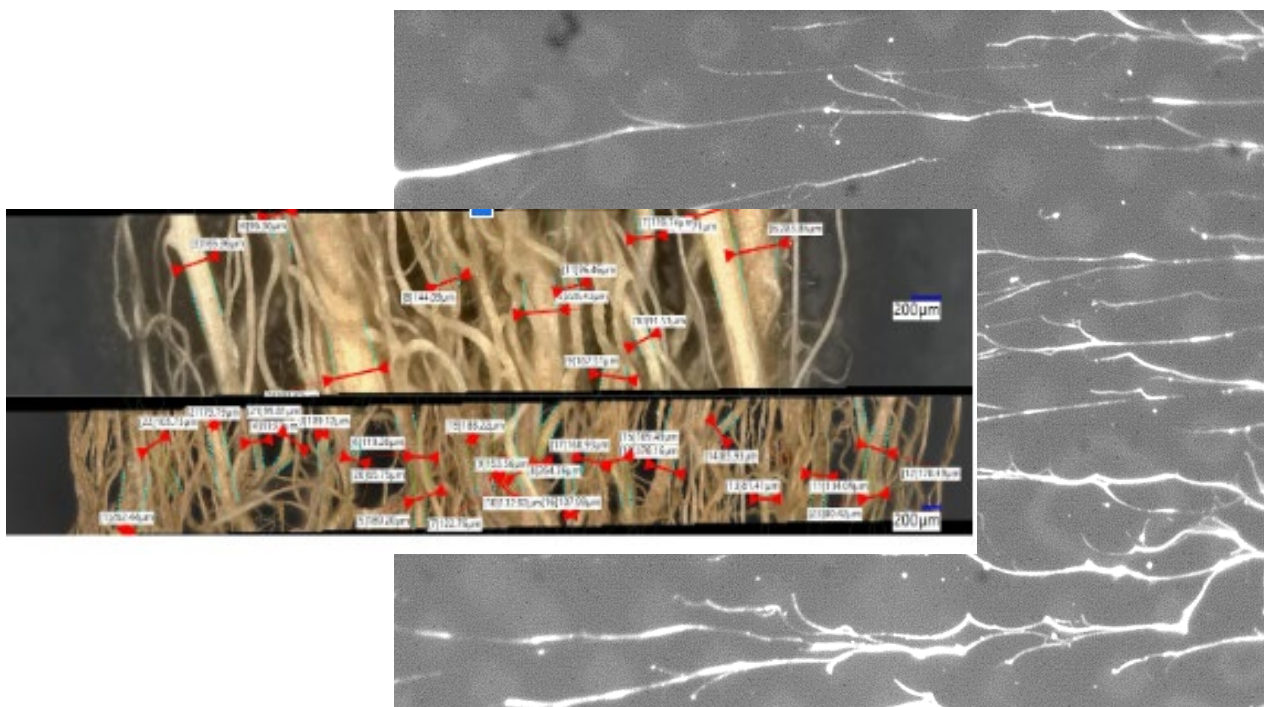
Figure 1: (a) 3D printed samples for thermal conductivity, electrical conductivity, and tensile tests. (b) Strain-Stress plot from tensile tests. (c) Electrical Conductivity to GNPs concentration plots, including vertical and horizontal infill data. (d) Pictures from thermal sensing cameras for standard PLA samples, 22PLA 66 PBAT 12 GNPs samples, 21 PLA 63 PBAT 16 GNPs samples, and 20 PLA 60 PBAT 20 GNPs samples.

Four-point electrical conductivity tests were performed on the 3D printed electrical test samples shown in Figure 1. As expected, electrical conductivity increases as GNPs concentration increases. 23 PLA 69 PBAT 8 GNPs and 22PLA 66 PBAT 12 GNPs samples were generally not electrically conductive. The electrical conductivity increases to 1.6 when 16% of GNPs is added. From 21 PLA 63 PBAT 16 GNPs to 20 PLA 60 PBAT 20 GNPs, the electrical conductivity increases from 1.6 to 2.1 S/m. In addition, the orientation of infill during the 3D printing process has an effect on electrical conductivity. According to our data, printed samples with infill direction perpendicular to electron transfer direction are less electrically conductive than samples with infill direction parallel to electron transfer direction. The thermal conductivity of samples were measured by a thermal sensing camera while the samples were heated for a fixed interval of time. The data suggested that the transmission of heat occurred much faster in 20 PLA 60 PBAT 20 GNPs and 21 PLA 63 PBAT 16 GNPs samples than those with lower GNPs concentration. In comparison to pure PLA, 20 PLA 60 PBAT 20 GNPs samples are 270% thermal conductive. This is coincident with our hypothesis that an increase in the concentration of graphene incurs an uplift in thermal conductivity. In the tensile test, the strain to stress diagram revealed the brittleness of 20 PLA 60 PBAT 20 GNPs samples. 23 PLA 69 PBAT 8 GNPs and 22PLA 66 PBAT 12 GNPs samples have significantly lower Young's Modulus values and greater toughness values as well as breaking elongation. As the concentration of GNPs increases from 8% to 20%, the maximum strain before breaking decreases from 4.3% to 1.5%. Such result corresponds to the hypothesis that at the microscopic level, graphene platelets block the interaction between polymers in the composites, giving rise to the decrease in material strength. Based on our evaluation of electrical conductivity, thermal conductivity, and mechanical strength, we expect the ideal blend of PLA, PBAT, and GNPs H-5 to have the proportion between 22PLA 66 PBAT 12 GNPs and 21 PLA 63 PBAT 16 GNPs. If the concentration of GNPs is above 16%, the material will be too brittle according to the mechanical tests data. Otherwise, if the concentration of GNPs equals or is below 12%, the electrical and thermal conductivity of the material will be comparatively low for practical use.

Session 10:

Biopolymers and Surfaces

Chairs: Robert Wong, Aaron Sloutski, and Yiwei Fang



Engineering a Reverse Thermo-Responsive, Cross-Linkable, Biodegradable Liquid Embolic Agent for Brain Aneurysm Treatment

Lamia Ayaz¹, Hannah Feng², Ruoxi Jin³, Ann Lee⁴, Sheldon Liu⁵, Evan Pang⁶, Jiarui Peng⁷, Grace Qiao⁸, Ruth Pereira⁹, Robert Wong⁹, Aaron Sloutski⁹, Chandramouli Sadasivan^{9, 10}, Daniel Cohn¹¹, Miriam Rafailovich⁹

¹Howard High School, Ellicott City, MD, 21043; ²Torrey Pines High School, San Diego, CA, 92130; ³Beijing National Day School, Beijing, 100039; ⁴Seoul International School, Seoul, South Korea, 13113; ⁵Stuyvesant High School, New York, NY, 10282; ⁶Mission San Jose High School, Fremont, CA, 94539; ⁷East Lyme High School, East Lyme, CT, 06333; ⁸The Experimental High School Attached to Beijing Normal University, Beijing, 100032; ⁹Department of Materials Science and Chemical Engineering, Stony Brook University, Stony Brook, NY, 11790; ¹⁰Department of Neurological Surgery, Stony Brook University, Stony Brook, NY, 11790; ¹¹Hebrew University of Jerusalem, Jerusalem, Israel, 91904013

*Authors 1-8 contributed equally to this work

Cerebral aneurysms are dilations of cerebral vasculature walls that can rupture, leading to hemorrhagic stroke. Although the majority of current aneurysm treatments involve implantation of catheter-based endovascular coils and meshes, they show unfavorable primary outcomes in 20% to 30% of cases [1]. Existing liquid embolic agents (LEAs) serve as alternative treatment options but demonstrate strong thrombogenic properties, dependence on organic solvent carriers, and mass effects. The development of a reverse thermo-responsive, cross-linkable, and biodegradable liquid embolic agent using pluronic F88-DMA is expected to mitigate many of these issues, and this study aims to characterize the properties of this hydrogel.

F88-DMA polymer was utilized to form the hydrogel due to its physical gelation at physiological temperatures and cross-linking mechanical strength. The polymer was mixed with ammonium persulfate (APS) and tetramethylethylenediamine (TEMED) for cross-linking, while iohexol was added as a contrast and diluting agent.

Upon gelation and crosslinking, hydrogels swell *in situ* due to thermodynamic forces, posing significant risk for compression or rupture. F88-DMA hydrogel swelling was demonstrated to be dependent on polymer concentration: the 24% F88-DMA gel swelled the least with a 29% mass increase at the observed peak and a 28% mass increase after 3 days ($p = 0.019695$) (Figure 1a). Furthermore, the addition of iohexol significantly decreased swelling over the course of 3 days (Figure 1b). These findings are valuable in determining the optimal F88-DMA and iohexol concentration for use as a liquid embolic agent.

Rheology was used to determine that a higher concentration of F88-DMA lowers gelation temperature. This correlation was further confirmed with differential scanning calorimetry. The gelation and micellization peaks were determined by plotting heat flow against temperature. The temperatures at which the gelation peak occurred aligned with the transition temperatures from rheology for all three concentrations of F88-DMA (27%, 30%, & 33%), corroborating that the gelation temperature decreases with increasing polymer concentration.

Furthermore, benzoyl peroxide (BPO) was explored as an alternative crosslinker. BPO is heat sensitive, enhancing the injectability and controllability of the gel. Specifically, F88DMA treated with 3.5% APS and varying concentrations of BPO demonstrated successful crosslinking when incubated at 37°C. The rheological results of F88DMA treated with 3.5% (v/v) APS and 2% (v/v) BPO revealed a noticeable delay in the crosslinking time.

These trials indicate that future LEA developments should be centered around lower-concentration gels, further exploring iohexol and various crosslinking agents as additives. Future studies will involve injecting this gel into rabbit models to examine its effects *in vivo*, examining rates of endothelialization post-injection, analyzing microcatheter injections of the gel in model aneurysms, measuring the effect of APS and TEMED concentration on crosslinking time, and continuing development of a peptide gel that degrades with naturally-occurring, patient-specific enzyme activity.

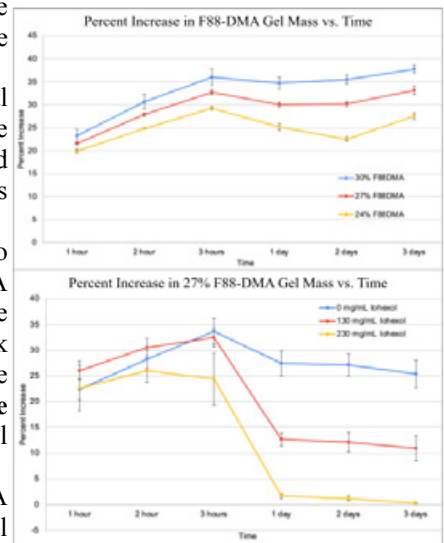


Figure 1: Percent increase in F88-DMA gel mass for a) different concentrations of F88-DMA and b) different concentrations of iohexol

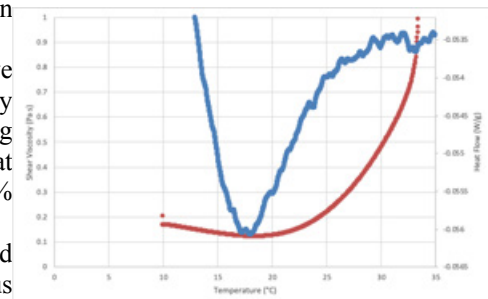
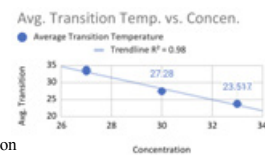


Figure 2. Rheology and Differential Scanning Calorimetry Overlay for 27% F88DMA

Figure 3. Average Transition Temperature vs Concentration for 27%, 30%, 33% F88DMA samples



[1] Taschner CA, Chapot R, Costalat V, Machi P, Courtheoux P, Barreau X, et al. Second-Generation Hydrogel Coils for the Endovascular Treatment of Intracranial Aneurysms: A Randomized Controlled Trial. *Stroke*. 2018;49(3):667-74.

***Rhizobium Tropici*-Produced EPS Biopolymer: Chemical Analysis and Impact on Bermuda Grass Root Growth**

Haaris Alam¹, Isana Alicea², Brinley Dai³, Jerry Gao⁴, Ashritha Kalakuntla⁵, Tei Kim⁶, Elise Ngo¹, Tony Guo Feng Tung⁷, Yiwei Fang⁸, Aaron Sloutski⁸, Marcia Simon⁹, Jay Gao¹⁰, Miriam Rafailovich⁸

¹Portola High School, Irvine, CA 92618, ²Patchogue Medford High School, Medford, NY, 11763, ³Experimental High School Attached to Beijing Normal University, Beijing, China, 100035, ⁴Beijing No. 80 High School, Beijing, China, 100102, ⁵Ed W. Clark High School, Las Vegas, NV, 89102, ⁶Stanford Online High School, Redwood City, CA, 94063, ⁷Shanghai High School International Division, ⁸Department of Materials Science and Chemical Engineering, Stony Brook University, Stony Brook, NY 11794, ⁹Department of Oral Biology & Pathology, Stony Brook University, Stony Brook, NY 11794, ¹⁰Stony Brook University School of Dental Medicine, Stony Brook, NY 11794

Authors 1–8 contributed equally to this work

Erosion control is imperative to soils vulnerable to flooding, such as watersheds in the Mississippi River Basin.¹ A potential solution is extracellular polymeric substances (EPS): hydrated microbial biopolymers whose high water-holding capacity, entrapment of nutrients, and resistance to environmental stressors help maintain the structural integrity of soil.² A related benefit of EPS is their ability to enhance subterranean root growth; a corresponding increase in root mass or length can stabilize topsoil and aid in erosion control.¹ However, the specific composites and properties of EPS that pertain to root growth remain unclear. This project aims to investigate the influence of EPS derived from *Rhizobium tropici* bacteria, RT-EPS, produced with and without dialysis on root growth in Bermuda grass.

First, the chemical composition of RT-EPS was analyzed with high-performance liquid chromatography (HPLC) and the interaction between RT-EPS and clay was explored through rheology. The former exhibited a significant presence of polysaccharides in RT-EPS and the latter displayed the mixture's superior mechanical properties, which simulate RT-EPS's on-site reinforcement of soil via shear strength enhancement. Moreover, protein assays demonstrated the presence of protein in the bulk of the RT-EPS produced. Their impact will be further examined.

To investigate the impact of RT-EPS on plant growth, Bermuda grass seeds were germinated in soil and sand treated with tap water (control), non-dialyzed RT-EPS, and dialyzed RT-EPS. The seeds were grown in one of three conditions: a controlled chamber, inside a greenhouse, or outdoors. The mass and length of the roots and shoots were measured after a 60-day growth period, revealing that RT-EPS treatment increased the mass proportion of roots. Additionally, the structure, density, and elemental composition of the roots of Bermuda grass grown in sand were analyzed via the Keyence 3D Microscope. Imaged RT-EPS-treated samples exhibited higher density, greater branching, and elevated tertiary branching coverage (Figure 1). X-ray fluorescence (XRF) spectroscopy was performed to determine root concentrations of calcium, sulfur, potassium, and phosphorus, with results demonstrating a greater concentration of these important ions in samples with RT-EPS. X-ray diffraction (XRD) was then performed to determine the presence of crystalline structures on top of the roots; XRD-generated graphs are to be analyzed.

Future directions include in-depth research on the protein fraction RT-EPS contains, with a focus on their influence on root stem cell differentiation. Furthermore, further experiments will be conducted to compare the impacts of different types of RT-EPS dialysis (14K vs. 2K pores) on Bermuda grass root growth. The knowledge obtained from these studies will be utilized for open-field experiments to examine the effect of RT-EPS on large-scale growth, including soil analysis.

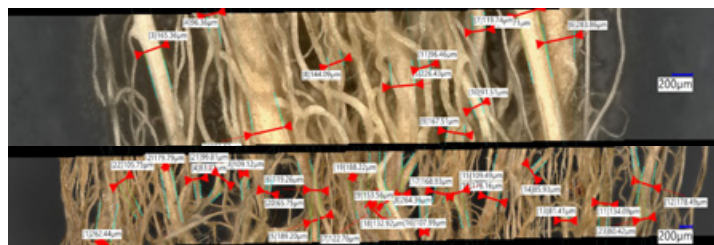


Figure 1. Root cross sections of Bermuda grass in sand grown inside the chamber. The top sample was treated with tap water and the bottom sample treated with 12.5 mg/ml non-dialyzed RT-EPS.

¹Yasarer, L. M. W., et al. (2019). Assessment of the soil vulnerability index and comparison with AnnAGNPS in two Lower Mississippi River Basin watersheds. *Journal of Soil and Water Conservation*, 75(1), 53–61. <https://doi.org/10.2489/jswc.75.1.53>

²Costa, O. Y., Raaijmakers, J. M., Kuramae, E. E. (2018). Microbial extracellular polymeric substances: Ecological function and impact on soil aggregation. *Frontiers in Microbiology*, 9. <https://doi.org/10.3389/fmicb.2018.01636>

Molecular Dynamics Simulations of Soil-Strengthening Hydrogels

Emily Sun¹, Shoumik Saha², Jose Nicasio², Dilip Gersappe², Miriam Rafailovich²

¹Westford Academy, Westford, MA 01886, ²Department of Materials Science and Chemical Engineering, Stony Brook University, Stony Brook, NY 11794

Hydrogels are crosslinked polymer networks that can absorb and retain large quantities of water within their structures. Typically made of hydrophilic polymers, their swelling ability gives these materials properties of both solids and liquids alike. [1] Recent studies have also shown that when these polymers are combined with charged clay-based nanofillers, the result is a fixed hydrogel with enhanced properties. [2] However, little is known about the mechanism of their network formation from a theoretical standpoint. Here, we explore a system of free-floating polymer chains to determine the specific network formation and rheology of a hydrogel, with an aim of determining the optimal conditions for producing the strongest hydrogel, which can then be used for soil-strengthening.

To do so, we perform coarse-grained molecular dynamics with the LAMMPS software. We simulate the system parameters with reduced units, which have been shown to optimize computational efficiency. Our polymer chains are modeled after the Kremer-Grest model, which defines bond interaction via the finitely extensible nonlinear elastic (FENE) potential. We model these for polymer concentrations of $N=300$, 600 , and 900 , with different distributions for their hydrophilic regions, or “stickers,” which are placed uniformly every 5th, 9th, and 14th monomers (5, 3, and 2 stickers). The system is set to NVT ensemble, to control for polymer concentration, volume, and temperature. We turn on attractive interaction between stickers, which allows polymer chains to connect and undergo network formation. The polymers’ dynamics will be calculated through the radius of gyration (R_g) values; overall diffusion coefficients will be measured from mean-squared-displacement (MSD) tests.

After confirming the dynamics of our free gels, we plan to test for their viscosity under different conditions. First we test a shear rate of 0, which is when our system is kept at equilibrium state. These results will be graphed with our stress-autocorrelation (SAC) calculations which summarize a substances’ viscosity behavior. Then we will apply external shearing rates of 0.12, 0.24, 0.36, and 0.48 then calculate viscosity behavior. We expect larger viscosity for 2 sticker systems, as similar results were seen with our small-concentration tests (**Fig. 1**). The shear tests will give an idea on their shear thinning properties, which help us determine the optimal freegel strength. Our specific results are expected to come out within seven days, after which we will summarize and compare them with that of previous work.

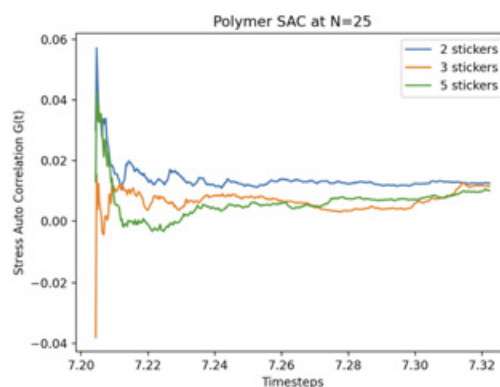


Figure 1. Stress autocorrelation functions of polymers with different sticker distributions plotted at a concentration of $N=25$.

[1] Ahmed, Enas M. "Hydrogel: Preparation, Characterization, and Applications: A Review." *Journal of Advanced Research*, vol. 6, no. 2, Mar. 2015, p. 106. *ScienceDirect*, <https://doi.org/10.1016/j.jare.2013.07.006>.

[2] Xu, Di, et al. "Rheology of Poly(N-isopropylacrylamide)–Clay Nanocomposite Hydrogels." *Macromolecules*, vol. 48, no. 3, 16 Jan. 2015, p. 840. *ACS Publications*, <https://doi.org/10.1021/ma502111p>.

A novel DNA ligase-based soft lithographic approach to ordered DNA fragmentation

Selina Zhang^{1,2 †}, Jude Ouerfelli^{1,3 †}, Aditi Kiran^{1,4 †}, Alex Zheng^{1,5 †}, Boheng Cao^{1,6 †}, Ellen Hu^{1,7 †},
Jonathan Sokolov¹, Miriam Rafailovich¹

[†] authors contributed equally to this work

¹ Stony Brook University, NY, 11794, ² North Hunterdon High School, NJ, 08801, ³ Fort Lee High School, NJ, 07024, ⁴ BASIS Independent Fremont, CA, 94539, ⁵ Stuyvesant High School, NY, 10282, ⁶ North Hollywood High School, CA, 91607, ⁷ C. Leon King High School, FL, 33610

As genetic sequencing grows more widespread in diagnostics and research, increasing its accessibility becomes more pressing. Current next generation sequencing (NGS) technologies entail the large-scale assembly of complete sequences from short, free-floating DNA fragments, resulting in high computational costs. Research has attempted to address this issue through long-read and third-generation sequencing, extending the length of the contiguous DNA fragments to tens of kilobase pairs.¹ However, repetitive regions of the DNA still limit the ability of software to reassemble unique sequences. Previous studies have examined DNA-depositing parameters for ordered fragmentation.²

In this work, we explore a novel approach to DNA fragmentation that entails depositing DNA molecules on the surface of a poly(methyl methacrylate) (PMMA)-coated silicon wafer and using soft ultraviolet (UV) lithography and UV photoresist patterning to suspend DNA, allowing steric clearance for transposase strandcutting over exposed regions. Such ordered fragmentation would tremendously reduce information loss and eliminate the need for original sequence order recovery.

To prepare the substrate, silicon wafers were cut into 0.5" by 0.5" squares and cleaned in a PSD UV ozone system (NovaScan) for 1 hour. A solution of 47.8 mg/g of 996K PMMA in toluene was spin-casted onto the cleaned silicon squares at 2500 RPM for 30 seconds. After overnight annealing in a vacuum oven at 130 °C, the samples were patterned with soft UV lithography. A 2000 mesh copper grid (Ted Pella) was placed on the sample underneath a piece of quartz glass to limit motion. The samples were exposed to 257 nm UV radiation of intensity $0.1 \pm 0.02 \text{ mW}/(\text{mm})^2$, followed by development in a 7:3 isopropyl alcohol (IPA) and water solution. UV exposure was found to increase the hydrophilicity of the PMMA surface, which was uncondusive to DNA stretching, so we aimed to minimize UV exposure and increase development accordingly to create sufficiently deep wells. We analyzed ellipsometry, atomic force microscopy (AFM), light microscopy with an Olympus microscope, and contact angle goniometry data, determining that 7 hours of UV exposure and 2 minutes of IPA:water development were optimal for DNA combing on PMMA wafers.

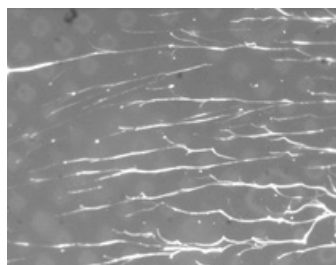


Figure 1. Ligated DNA deposited on a developed surface, with a pattern created by photolithography

λ bacteriophage DNA was ligated to obtain long concatemers for surface deposition. Solution for ligation was composed of 2 μL of λ DNA (NEB), 1 μL of stock DNA ligase, and 2 μL of stock ligase buffer, all diluted to 20 μL with nuclease-free water. The ligation solution was incubated at 16°C for 12 hours. Exposure to 65°C for 10 minutes deactivated ligase, and 10 μL 10x diluted SyBr Gold dye was added. The ligated DNA solution was finally diluted to 700 μL . Using a stepper motor connected to a linear stage, we dipped a PMMA wafer in this diluted solution for 60 seconds followed by withdrawal at a rate of 2 mm/s and then imaged with a Leica confocal microscope (Figure 1).

Our findings successfully demonstrate a deposition of ligated DNA onto the patterned PMMA surface. This suggests that further exploration involving Tn5 transposases may lead to promising results for ordered DNA fragmentation.

¹ Schadt, E. E., Turner, S., & Kasarskis, A. (2010). A window into third-generation sequencing. *Human Molecular Genetics*, 19(R2), R227–R240. <https://doi.org/10.1093/hmg/ddq416>

² Cho, N., Goodwin, S., Budassi, J., Zhu, K., McCombie, W. R., & Sokolov, J. (2017). Fragmentation of surface adsorbed and aligned DNA molecules using soft lithography for next-generation sequencing. *Journal of Biosensors & Bioelectronics*, 08(04). <https://doi.org/10.4172/2155-6210.1000247>

In silico study of the temperature effect on binding dynamics between SARS-CoV-2 spike glycoprotein and polylactic acid surface

Matthew Chang¹, Karin Hasegawa², Yuefan Deng²

¹Woodbridge High School, Irvine, CA, 92604, ²Department of Applied Mathematics and Statistics, Stony Brook University, Stony Brook, NY, 11794

Since the beginning of the global spread of COVID-19 caused by the SARS-CoV-2, healthcare workers worldwide involved in the treatment and care of COVID-19 patients have been at high risk of infection. Measures have been taken to prevent direct infection by use of personal protective equipment (PPE), and these measures seem to be effective to a certain extent. While the adequate use of such equipment is certainly a key of reducing such risk of infection, the risk of indirect transmission, namely fomite transmission due to the contamination of virus on PPE and other inanimate materials in hospitals, is still controversial and remains as a possible route of infection that requires careful investigation. Current studies have provided good understanding of survival rate of infectious SARS-CoV-2 on inanimate material surfaces and its temperature dependency from both direction of laboratory experiment and molecular dynamics simulation; however, to the best of our knowledge, molecular level understanding of the viral interaction with such material surfaces and their dynamics are still lacking in the current study. Understanding and explaining the result of such at atomic level is significant and inevitable to fully understand and interpret the macro level results that was found by others. The initial structure of S-protein was obtained from Protein Data Bank (PDB: 6VXX) [25, 26]. The original 6VXX structure had several missing residues, and the only modification made was filling the missing loops. Once the crystal waters were stripped out from the structure, the initial topology was generated based on CHARMM36 force field using GROMACS 2020.2. The PLA substrate model was prepared and 2 μ s simulations were run. The molecular simulations at the three temperatures, 3 deg, 24 deg, and 50 deg, are shown in Fig. 1. The result showed that the S-protein – PLA binding affinity was the highest at 24 deg which is the typical room temperature. As the temperature approaches either extreme, such as at 3 deg or at 50 deg, the binding affinity gets weaker. This indicates that the binding ability of the S-protein to the PLA surface is enhanced at normal temperature condition, which can pose a greater risk of contact transmission for front line health care workers who use PLA-based PPE equipment against SARS-CoV-2.

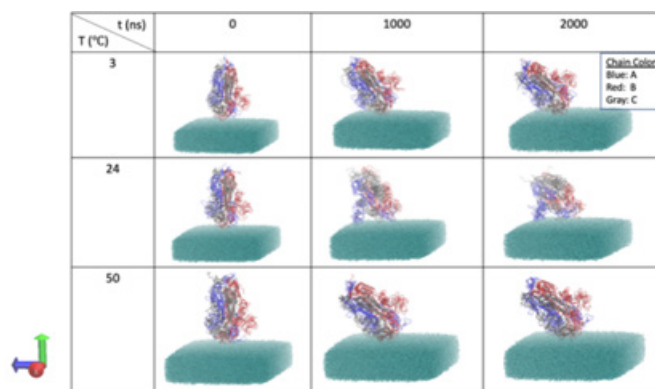


Fig. 1 The snapshots of each complex system ($T = 3, 24$ and $50\text{ }^{\circ}\text{C}$) at three different time points ($t = 0, 1$ and $2\mu\text{s}$).

[1] Rudberg A-S, Havervall S, Månberg A, et al (2020) SARS-CoV-2 exposure, symptoms and seroprevalence in healthcare workers in Sweden. Nat Commun 11:5064. <https://doi.org/10.1038/s41467-020-18848-0>

[2] Ye G, Lin H, Chen L, et al (2020) Environmental contamination of the SARS-CoV-2 in healthcare premises: An urgent call for protection for healthcare workers. Medrxiv 2020.03.11.20034546. <https://doi.org/10.1101/2020.03.11.20034546>



Hannah Oh



Richard Chen



Pia Sodhi



Jerry Gao



Isana Alicea



Selina Zhang

We gratefully acknowledge the support of ICL Group and the Louis Morin Charitable Trust

***Thanks for a
great summer!***

